eman ta zabal zazu

Universidad del País Vasco
Euskal Herriko Unibertsitatea

Modelling Thermo-Electric Transport and Excited States in Low Dimensional Systems

by

Robert Biele

Supervisors:
Prof. Dr. Angel Rubio
Dr. Roberto D'Agosta

A thesis submitted in partial fulfillment for the
degree of Doctor of Philosophy

in the
Faculty of Physics, Chemistry and Materials Science
Department of Materials Physics

May 2016

Abstract

The interaction of radiation with matter at the nanoscale has an inexhaustible range of applications in electronics, biotechnology and medicine. At the nanoscale, the length scale where the classical and quantum worlds meet, quantum effects dominate the light–matter interaction and unique phenomena arise. This work addresses fundamental questions on the overlap of quantum theory, non-equilibrium thermodynamics and material science.

As the exact description of these quantum phenomena is not feasible, we discuss how the open quantum system approach can be used to study thermal relaxation and thermo-electric transport at the nanoscale. The basic concepts of thermal relaxation are studied from first principles. As the conditions for relaxation are connected with the non-Markovian nature of the equation of motion, we discuss a time-local stochastic Schrödinger equation. Remarkably, this equation can describe thermal relaxation and transport dynamics correctly. Furthermore, this thesis introduces a thermal transport theory where the temperature field is established by radiation of classical blackbodies. The combination of this theory with the techniques of time-dependent current density functional theory provides an *ab initio* tool to study thermal transport in many-body systems. This approach is general and can be adapted to describe both electron and phonon dynamics. In this way, combined with the time-dependent current DFT, it provides a unified way to investigate *ab initio* electrical and thermal transport beyond linear response. The observation of thermo-electric transport in macroscopic bodies does not disturb the system or change the flow of energy. However, when moving towards the nanoscale, measurements may influence the system and has to be considered. We demonstrate that the choice of location of these local measurements provides control of the direction of the energy flow and of the particle currents separately. These results seem to violate the second law of thermodynamics. By treating decoherence as a thermodynamic bath we resolve this contradiction. In order to further advance the applications of light–matter interactions for realisable materials, the electronic and optical properties of 2D layered semiconductors are studied. 2D materials have established their place as candidates for the next generation of opto-electronic devices. Specifically, the electronic and optical properties of TiS_3 and In_2Se_3 are theoretically investigated within DFT and many-body perturbation theory. This work constitutes a first step towards exploiting the trichalcogenide family in 2D opto-electronical applications, such as chemical sensors, passive optical polarisers, fast photodetectors, and battery technologies.

List of Publications

- **published during the PhD:**
  - **“A stochastic approach to open quantum systems”**
    R. Biele and R. D’Agosta, Topical Review in Journal of Physics Condensed Matter **24**, 273201 (2012).
  - **“Application of a time-convolutionless stochastic Schrödinger equation to energy transport and thermal relaxation”**
    R. Biele, C. Timm, and R. D’Agosta, Journal of Physics Condensed Matter **26**, 395303 (2014).
  - **“Time-Dependent Thermal Transport Theory”**
    R. Biele, R. D’Agosta, and A. Rubio, Physical Review Letters **115**, 056801 (2015).
  - **“TiS_3 transistors with tailored morphology and electrical properties”**
    J. O. Island, M. Barawi, R. Biele, A. Almazán , J. M. Clamagirand, J. R. Ares, C. Sánchez, G. A. Steele, H. S. J. van der Zant, J.V. Alvarez, R. D’Agosta, I. J. Ferrer, and A. Castellanos-Gomez, Advanced Materials **27**, 2595–2601 (2015).
  - **“Electronic bandgap and exciton binding energy of layered semiconductor TiS_3”**
    A. J. Molina-Mendoza, M. Barawi, R. Biele, E. Flores, J.R. Ares, C. Sánchez, G. Rubio-Bollinger, N. Agraït, R. D’Agosta, I. J. Ferrer, and A. Castellanos-Gomez, Advanced Electronic Materials **1**, 9 (2015).
  - **“Titanium trisulfide (TiS_3): a 2D semiconductor with quasi-1D optical and electronic properties”**
    J. O. Island, R. Biele, M. Barawi, J. M. Clamagirand, J. R. Ares, C. Sánchez, H. S. J. van der Zant, I. J. Ferrer, R. D’Agosta, A. Castellanos-Gomez, Scientific Reports **6**, 22214 (2016).
- **submitted:**
  - **“Strain-induced bang-gap engineering in layered TiS_3”**
    R. Biele, E. Flores, J. R. Ares, C. Sánchez, I. J. Ferrer, G. Rubio-Bollinger, A. Castellanos-Gomez, and R. D’Agosta, submitted (2015).
  - **“Layered TiS_3 for fast and broadband photodetectors”**
    J. O. Island, A. J. Molina-Mendoza, M. Barawi, R. Biele, J. M. Clamagirand, J. R. Ares, C. Sánchez, H. S.J. van der Zant, R. D’Agosta, I. J. Ferrer, A. Castellano-Gomez, chapter submitted to Springer books (Jan, 2016).
  - **“Strong quantum confinement effect in the optical properties of ultrathin In_2Se_3”**
    J. Quereda, R. Biele, G. Rubio-Bollinger, N. Agraït, R. D’Agosta, and A. Castellanos-Gomez, submitted (March, 2016).
- **to be submitted soon:**
  - **“Decoherence-driven thermo-electric transport”**
    with C. Rodríguez-Rosario and A. Rubio.

Abbreviations

DFT	**D**ensity **F**unctional **T**heory
KS	**K**ohn–**S**ham
OQS	**O**pen **Q**uantum **S**ystem
SSE	**S**tochastic **S**chrödinger **E**quation
NMSSE	**N**on-**M**arkovian **S**tochastic **S**chrödinger **E**quation
TCLSSE	**T**ime-**C**onvolution**L**ess **S**tochastic **S**chrödinger **E**quation
NMME	**N**on-**M**arkovian **M**aster **E**quation
BSE	**B**ethe–**S**alpeter **E**quation
MBPT	**M**any-**B**ody **P**erturbation **T**heory
TMDCs	**T**ransition **M**etal **D**i**C**halcogenides
SEM	**S**canning **E**lectron **M**icroscopy
FET	**F**ield-**E**ffect **T**ransistors
RPA	**R**andom **P**hase **A**pproximation
STM	**S**canning **T**unnelling **M**icroscope
STS	**S**canning **T**unnelling **S**pectroscopy
AFM	**A**tomic **F**orce **M**icroscope

Contents

Chapter 1

Introduction

Nanoscience is a relatively young field which covers the overlap between physics, chemistry, biology and engineering at the nanoscale, the length scale where the classical and quantum worlds meet. Within the last decades a significant effort of a growing community of engineers and scientists has been devoted to nanotechnology. It has as well attracted the interest and imagination of the general public. It is primarily defined by a length scale, the nanometer, which we are now able to explore thanks to recent experimental developments. While lithographic techniques have allowed the fabrication of increasingly smaller structures, advances on the characterisation side by scanning tunnelling and atomic force microscopy provide the atomic scale resolution. Recently developed experimental techniques have triggered the creation of entirely new classes of materials such as quantum dots, fullerenes, nanotubes and nano-composites. These materials may be used as building blocks for completely new structures and devices with an almost unlimited range of applications.

This rapid progress in experimental physics has forced theorists to develop new approaches and viewpoints as novel properties have emerged at the nanometer scale. While some physical assumptions and approximations worked well for mesoscopic systems, they may fail when entering this “nanoworld”. When moving from macroscopic systems towards the nanoscale, one reaches the quantum coherence length of many materials, and quantum entanglement effects become more important. For instance, while Kirchoff’s law applies at the macroscopic level, it fails at the nanoscale, where phase coherence can provide interference effects on electrical transport [1]. Also, nanoscale systems are much more sensitive to the interaction with other systems. For instance, a local measurement could suppress quantum coherence locally and might lead to a variety of novel effects, such as the enhancement of energy transport [2, 3] or the creation of electrical currents. In addition, when thinking of a system consisting of only a single electron, thermodynamics may no longer apply. When entering this nanoscale world questions arise, such as, how one should define statistical properties for instance the temperature or pressure? Even worse, when dealing with thermal or energy transport, the system is shifted out of its equilibrium state and the important concept of a local temperature appears difficult to justify in this non-equilibrium problem. This shows that deep and fundamental questions in the overlap between thermodynamics and quantum theory still exist [4, 5] and have to be carefully addressed.

All these advances in the experimental and theoretical control of matter at the scale of small molecules to single atoms have opened a wide range of applications in the field of molecular electronics, photocatalysis, medicine, optoelectronics and biotechnologies, to just name a few. The ultimate target of nanotechnology is to advance materials and devices that will outperform current technologies, and even create new ones with completely new behaviours. As an example, novel electronic transport properties show up in mechanically controllable break junctions [6], a junction that is created by mechanically breaking a metal wire resulting in a single atomic contact between two large chunks of the same material. There, a typical electrical current of around $1\,\mu$A across the whole system will create a current density of around 10^9 A/cm^2 [7] across the atomic junction. These current densities are orders of magnitude larger than those found in macroscopic systems, and will amplify electron–electron and electron–ion interactions locally in the nanostructure. This can result in a heating up of the junction and affect its structural stability under current flow. The understanding of how such heat is carried and distributed in nano-structured system might answer questions such as whether Fourier's law also applies at the nanoscale and can have a practical impact on society. For instance, the flow of energy could be harnessed via thermoelectric effects [8, 9] to generate an electrical current. Improving the efficiency of such heat–voltage converters at the nanoscale might influence the global use of alternative energy resources. Other important applications of thermal transport at the nanoscale include thermal transistors [10, 11], thermal rectifiers [12, 13] and even thermal memory and logic gates [14, 15].

This thesis deals with the fundamental interaction of radiation with matter and its applications in nanotechnology. While the understanding of radiation has a long history, early speculations on the nature of light date back to the first millennium B.C.. These yielded the idea that light appeared very soon after the beginning as "God divided the light from the darkness" (Genesis

1.4). The competing notions of wave and particle have dominated our thinking about light ever since. Early in the fifth century B.C. Empedocles of Agrigentum was writing about a corpuscular theory of light which moves at a finite velocity. In 300 B.C. Euclid proposed the law of reflection and Seneca produced colours with a prism [16]. In the early seventeenth century Grimaldi discovered diffraction and Hooke suggested that light is a transverse wave [16]. At the same time, Newton believed in a corpuscular theory of light, although he investigated interference effects, as he believed that strict rectilinear propagation is not compatible with the wave theory [17]. Later, in the nineteenth century James Clerk Maxwell proposed his unified theory connecting the electric and magnetic [18] field with the charge density and current density. From his equations he deduced the electro–magnetic wave equation that predicted that light propagates as an electro–magnetic disturbance in a medium called the aether with the finite speed of light. While this classical theory of light has developed so rapidly and achieved such success, some disagreement with experiments on the interaction of matter with radiation began to appear. Experiments showed that electrons are able to escape from a metal surface when exposed to radiation. The classical wave theory predicts that the kinetic energy of those electrons should depend on the intensity of the incident radiation. However, it was found that the kinetic energy of the emitted electrons only increases with increasing frequency of the incident light [19]. This observation and the ultraviolet catastrophe for blackbody radiation presented significant difficulties for the classical theory. These led to the early quantum theory of matter and light. Einstein's paper in 1905 [20] not only contains his famous discussion on the photoelectric effect but also a discussion of blackbody radiation. There he suggested that light behaves as a gas of corpuscles with a discrete energy, that is, photons. However, in 1951 Einstein admitted [21]: "All these fifty years of conscious brooding have brought me no nearer to the answer to the question 'What are light quanta?' Nowadays every Tom, Dick and Harry thinks he knows it, but he is mistaken."

As this thesis deals with the coupling of quantum radiation to matter, I will address fundamental questions on the overlap of quantum theory, thermodynamics and electrodynamics here. For instance, a system in radiative contact with the surrounding should relax towards a thermal equilibrium state. This fundamental law of thermodynamics also holds true for nanoscale systems. In order to describe such relaxation dynamics, one needs to allow the system to exchange energy with the radiation field via spontaneous and stimulated emission and absorption of light. As the exact description of these quantum processes is not feasible, I will discuss in chapter 2 the concept of **Open Quantum Systems** (**OQS**) which describes the coupling of the system to quantum radiation in a way that makes calculations feasible. In this thesis, we will mainly focus on two approaches to OQS, namely master equation and stochastic wave-function methods. A quantum master equation is a deterministic equation of motion for the density operator, which can become numerically quite costly when the system under consideration becomes large. Within stochastic wave-function methods, we are confronted with an equation of motion for the wave function, which incorporates any small fluctuation of the environment as a random effect on the system. We will see that in both approaches the influence of the radiation onto the system enters through additional terms into the equation of motion. One of these not only depends on the current state of the system, but also depends on the entire history of the state. This behaviour is called non-Markovian and makes OQS costly to apply. I also discuss in detail conditions for thermal relaxation, which are connected to this non-Markovian term. Hence, by performing approximations on this term, one might incorrectly describe thermal-relaxation behaviour. Therefore, we study in chapter 3 whether with a time-local version of a non-Markovian stochastic Schrödinger equation, thermal relaxation and thermal transport dynamics can be described correctly.

In chapter 4 we will address how to define a local temperature and incorporate thermal gradients into nanoscale systems by introducing a thermal transport theory where the temperature field is established by two or more blackbodies of known thermal properties. Besides thermal transport at the nanoscale, this theory can be used to understand energy transport in cold atoms, biological, or optical systems. We will show that our approach recovers known physical results, as the linear relation between the thermal current and the temperature difference between two blackbodies. Furthermore, this theory is not limited to the linear regime and goes beyond it by accounting for non-linear effects and transient phenomena. Since this approach is general and can be adapted to describe both electron and phonon dynamics, it is a first step towards a unified formalism for investigating thermal and electronic transport at the nanoscale.

As another application of the interaction of radiation with matter at the nanoscale, the influence of a local measurement on thermo-electric transport, will be investigated in chapter 5. This local measurement can be thought of as an observer breaking quantum coherence by a dynamical process known as decoherence [22]. Decoherence has been shown to affect the efficiency of transport in molecular devices and biological systems [23]. The observer is modelled by a decoherence bath within OQS that can be treated as a new kind of quantum thermodynamic bath. We study how this type of quantum measurement can change the direction and magnitude of heat flow. Depending on where and how strong these observations are, we find that the heat flow can go against the heat gradient. We also show how, under these observations, particle currents can be created and controlled. Furthermore, we study how the choice of location of these quantum measurements can provide full control of the direction of the energy flow and of the particle currents separately. Even though this seems baffling from a thermodynamic point of view, by treating quantum measurements as a thermodynamic bath we resolve this paradox.

Not only has our understanding of what light is evolved, but concomitantly, our understanding of what matter is. At increasingly smaller scales, particles no longer behave as predicted by classical physics and the principles of quantum mechanics have to be applied. Nowadays, condensed matter research is not mainly aimed at finding new fundamental laws, it deals mostly with solving the Schrödinger equation of a well-known Hamiltonian, and extracting useful information from this solution. However, for many-body problems in condensed matter physics or chemistry solving the Schrödinger equation numerically becomes intractable. Moreover, the exact solution contains information we are not interested in [24]. **Density functional theory** (**DFT**) provides an alternative approach for the description of quantum many-body systems. This is accomplished by circumventing the computationally costly task of finding the electronic many-body wave function via the solution of the Schrödinger equation. DFT provides, in principle, an exact description only for the ground state energy and density of the many-body system. However, by employing the Kohn-Sham wave functions obtained from DFT, one may often obtain a reasonable description for all ground-state properties. Nowadays, DFT is the most widely used method for electronic structure calculations in the condensed matter community. Section 6.1 gives a brief introduction to DFT. While DFT in its static formulation is an effective one-particle scheme and in principle capable to predict ground-state energies correctly, it often has problems predicting the electronic structure of systems involving d-electrons, excited systems, and the absorption of light. Therefore, section 6.1 additionally discusses how to treat the interaction of a quantum system with classical light within many-body perturbation theory by discussing the GW approximation and the Bethe–Salpeter equation. These techniques will be applied in the rest of chapter 6 to 2D layered semiconductors to study their electronic and optical properties. Atomically thin semiconductors are very attractive materials for the design of novel optoelectronic nanoscale devices due to their large surface–to–volume ratio, high transparency and flexibility. 2D materials have established their place as candidates for the next generation of optoelectronic devices. They present outstanding mechanical and electrical properties and can be easily integrated with conventional silicon technologies. Comparing them to their higher (3D) and lower (1D) dimensional counterparts, 2D materials offer higher electric field tunability. Additionally, layered materials often bring new functionalities and applications beyond those of industry standard transistors and photodetectors. These improved properties include stronger light–matter interaction [25, 26], and greater flexibility and transparency [27, 28].

This thesis is devoted to the many different aspects of the interaction of radiation with matter. Therefore, chapter 2 discusses the theory of OQS that describes the coupling of a quantum system to photons, while section 6.1 introduces briefly DFT and how to describe the coupling of quantum systems to classical light. The concepts introduced in chapter 2 are necessary for the study of chapters 3 to 5, thus the reader only interested in chapter 6 can skip the introduction on OQS. Equations throughout this thesis are written in atomic units ($\hbar = m_e = 1/(4\pi\epsilon_0) = e = 1$). Although in the applied chapter 6 we use in the text units like Kelvin or nanometer to compare with realistic quantities. I hope the reader will enjoy this journey of the many fascinating aspects of the interaction of radiation and matter. Hopefully Einstein would not have included our names amongst his Toms, Dicks, and Harrys.

Chapter 2

Open Quantum Systems

In this chapter I will describe the basic theoretical concepts underlying chapters 3 to 5. As mentioned in the introduction, the focus of this work is on the very fundamental interaction of matter with radiation. The first step towards modelling matter is usually to consider it as isolated. However, for any size of system, there is always some leakage or coupling, which does not allow for a complete decoupling of the dynamics of the system from the external environment. Although this coupling may be weak, it might influence the system in a non-trivial way as it acts over long times. This radiative interaction can lead to the dissipation of energy, the loss of coherence and thermalisation of the quantum system. A full description of phenomena arising from the interaction between matter and photons is provided by quantum electrodynamics. However, for most of the systems of relevance in physics, chemistry, biology and nanoscience, such a description cannot be obtained and approximations must be made. Therefore, we will concentrate in this chapter on how the influence of quantum-radiation fields on matter can be incorporated into a dynamical description via OQS.

The accurate description for the time-evolution of the system in contact with the environment would be the Schrödinger equation for the total system. This combined system consists of the quantum system under consideration, the macroscopic environment and its coupling to the quantum system. As the total system is a macroscopic object itself, its exact dynamical description via Schrödinger's equation is not feasible. Furthermore, as one is only interested in the small system, solving the Schrödinger equation for the total system would give us information that is not necessary. Therefore, the demand for a simpler description of the system under the influence of its surrounding emerges. This has been accomplished in a very elegant and natural manner by the theory of OQS. This theory plays an important role in many branches of physics, ranging from quantum information over quantum optics to condensed matter physics and quantum computing. It has been an active research topic since the middle of the last century. During this period many distinct approaches to the description of OQS have been developed.

In OQS the dynamics of the total system is expressed in the Hilbert space of the small system. This immense reduction in dimensionality makes the quantum mechanical investigation of a system coupled to the surrounding possible. In this work we will focus mainly on two approaches to OQS, namely the master equation and stochastic wave-function methods. These approaches are in principle equivalent, although both have their advantages and disadvantages. While quantum master equations are deterministic equations of motion for the density operator, they can get numerically quite costly when the system under consideration becomes bigger. Within stochastic wave-function methods, on the other hand, we are confronted with an equation of motion for the wave function, which incorporates any small fluctuation of the environment as a random effect on the system. Here, we will focus on the so-called **stochastic Schrödinger equation** (**SSE**) for the time evolution of the 'state' of the system. It simulates the average behaviour of a variety of condensed matter systems interacting with their environments. In doing so, we will build an ensemble of states and to obtain any physical quantity we will average over this ensemble. This SSE will serve us in this work as a starting point to investigate the dynamics of open quantum systems capable of exchanging energy and momentum with an external environment.

In the following, we will bother the reader neither with historical details of those techniques nor with too many technicalities of the derivation of master equations or SSEs. The interested reader can find those in a series of brilliantly written textbooks and reviews on the wide topic of OQS [29–32]. What we will do instead, is to introduce both concepts on equal footing by pointing out the important approximations. In order to assimilate the following chapters, it is not needed to understand every technical detail of the derivation of such equations. This will give the reader a feeling for the situations to which those equations can be successfully applied. In addition, the detailed derivation of the SSE can be found in appendix A.

While in this chapter, matter is described by model Hamiltonians and the focus is more on the interaction of matter with photons. In chapter 6 the full quantum-mechanical description of many-body electronic systems interacting with classical light will be discussed.

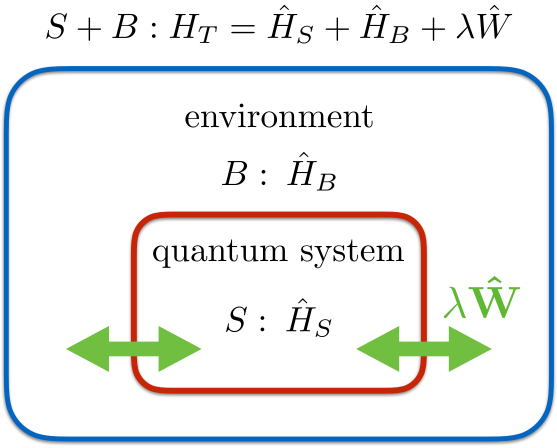

FIGURE 2.1: Typical situation when a description in terms of OQS is needed: We are interested in the dynamics of the small quantum system *S* which is interacting via $\lambda\hat{W}$ with a macroscopic environment, *B*. The solution of the whole problem is not feasible.

2.1 Master Equations and Stochastic Schrödinger Equations

A dynamical description of OQS is usually required when one faces the situation described in Fig. 2.1. We are interested in the dynamics of the system *S* (described by the Hamiltonian $\hat{H}_S$), which is embedded or in contact with one or more macroscopic systems, the environment (also called bath) *B*. Solving the Schrödinger equation for the combined system, *S*+*B*, is far beyond feasible. A very elegant and natural way to describe the effects of the environments in the Hilbert space of the system *S* is given by OQS.

The common starting point for the derivation of master equations or stochastic Schrödinger equations is the equation of motion for the system and its surrounding, described by the total Hamiltonian

$$\hat{H}_T = \hat{H}_S + \hat{H}_B + \lambda\hat{W}, \tag{2.1}$$

where $\hat{H}_B$ represents the environment which couples weakly via $\lambda\hat{W}$ to the system *S*. Here, the parameter λ is introduced to allow a perturbative expansion afterwards. The interaction potential $\hat{W}$ is assumed to be linear,

$$\hat{W} = \sum_a \hat{S}_a \otimes \hat{B}_a, \tag{2.2}$$

where $\hat{S}_a$ and $\hat{B}_a$ are hermitian coupling operators of the system and the environment, respectively. In general the interaction can be written in such a linear form. If not, the separability of the system and the environment is questionable.

While for the derivation of a master equation one starts from the von Neumann equation of motion for the density matrix, here our starting point will be the Schrödinger equation for the system and the environment:*

$$i\partial_t|\Psi_T(t)\rangle = (\hat{H}_S + \hat{H}_B + \lambda\hat{W})|\Psi_T(t)\rangle. \tag{2.3}$$

From this we derive in Appendix A the non-Markovian SSE based on a perturbative expansion up to second order in the coupling parameter λ. Therefore, after changing to the interaction picture we integrate out the irrelevant degrees of freedom of the environment and furthermore, we neglect initial correlation of the system with its surrounding,

$$\hat{\rho}_T(0) = |\phi(0)\rangle\langle\phi(0)| \otimes \hat{\rho}_B^{\mathrm{eq}} = |\phi(0)\rangle\langle\phi(0)| \otimes \frac{e^{-\beta\hat{H}_B}}{Z_B}, \tag{2.4}$$

where β is the inverse of the temperature and $Z_B = \mathrm{Tr}_B\, e^{-\beta\hat{H}_B}$. Here, we have defined that the system *S* is initially in a pure state while the bath is in thermal equilibrium. As we are interested in the corresponding initial wave function to the total density operator of Eq. (2.4), one needs to introduce

$$|\Psi_T(0)\rangle = |\phi(0)\rangle \otimes \sum_n \sqrt{\frac{e^{-\beta\epsilon_n}}{Z_B}} e^{i\theta_n}|n\rangle, \tag{2.5}$$

where $|n\rangle$ are eigenfunctions of the environment with eigenenergies ϵ_n, and θ_n are independent random phases uniformly distributed over the interval $[0, 2\pi]$. Exactly here is where the stochasticity enters the equation of motion and what makes the difference to deterministic master equations. While in a density operator formalism the phases are naturally washed out, in a wave-function approach those unknown phases are kept via stochastic noises. After performing a thermal average and rearranging the terms we arrive at a SSE for the state of the system $|\phi\rangle$ [30, 33, 34],

$$\begin{aligned} i\partial_t|\phi(t)\rangle &= \Big[\hat{H}_S + \lambda\sum_a \gamma_a(t)\hat{S}_a\Big]|\phi(t)\rangle \\ &\quad -i\lambda^2\sum_{a,b}\hat{S}_a\int_0^t \mathrm{d}\tau e^{-i\hat{H}_S\tau}\hat{S}_b C_{ab}(\tau)|\phi(t-\tau)\rangle. \end{aligned} \tag{2.6}$$

Here, many details have been left out while we have focused on the main assumptions, however, the full derivation with all technicalities can be found in Appendix A. The stochastic term enters

---

*Here, I would like to remind the reader of the usage of atomic units.

via the coloured noise $\gamma(t)$ characterised by its variance and mean value,

$$\overline{\gamma_a(t)} = 0, \qquad \overline{\gamma_a(t)\gamma_b(t')} = 0, \qquad \overline{\gamma_a^*(t)\gamma_b(t')} = C_{ab}(t-t'). \tag{2.7}$$

I would like to emphasise that in Eq. (2.6) the change of the system at time *t* depends not only on the state $|\phi(t)\rangle$ but also on the whole history in the interval from the initial time to time *t*. This behaviour is called non-Markovian and thus Eq. (2.6) is a **non-Markovian stochastic Schrödinger equation** (**NMSSE**). In this equation the integrant over the whole history of the wave function is also called memory kernel.

In the NMSSE the coupling of the bath to the subsystem is described in an approximate manner and enters the dynamics through the bath-correlation function $C_{ab}(t)$,

$$C_{ab}(t-t') = \mathrm{Tr}_B\left[\hat{\rho}_B^{\mathrm{eq}}\hat{B}_a(t)\hat{B}_b(t')\right]. \tag{2.8}$$

This implies that all the information about the time evolution of the bath and its coupling to the system is contained in the bath-correlation function. In comparison to the original closed Schrödinger equation for the combined system, an enormous reduction of dimensionality has been achieved, at the cost of now having to solve a stochastic equation of motion which is in addition non-Markovian.

In most quantum optical cases, the dependence on the past of the wave function can be approximately neglected, due to the fact that the bath-correlation function decays rapidly to zero on a time-scale on which the system's wave-function does not vary significantly. For convenience, one neglects the non-Markovian behaviour by approximating the time dependence of the bath-correlation function by a δ-function, $C_{ab}(t-t') \approx \frac{1}{2}D_{ab}\delta(t-t')$. As a result, the NMSSE simplifies to the *Markovian stochastic Schrödinger equation*,

$$i\partial_t|\phi(t)\rangle = \left[\hat{H}_S + \lambda\sum_a \gamma_a(t)\hat{S}_a - \frac{i\lambda^2}{2}\sum_{a,b}\hat{S}_a\hat{S}_b D_{ab}\right]|\phi(t)\rangle. \tag{2.9}$$

where $\gamma_a(t)$ are white-noise processes with $\overline{\gamma_a(t)} = 0$ and $\overline{\gamma_a^*(t)\gamma_b(t')} = D_{ab}\delta(t-t')$. With the help of a unitary transformation $U_{\gamma\delta}$ that diagonalises D_{ab} with eigenvalues d_a, Eq. (2.9) can be written in an Itô differential form

$$\mathrm{d}|\phi(t)\rangle = \left[\Big(-i\hat{H}_S - \frac{1}{2}\sum_a \hat{V}_a^\dagger\hat{V}_a\Big)\,\mathrm{d}t + \sum_a \hat{V}_a\,\mathrm{d}W_a\right]|\phi(t)\rangle, \tag{2.10}$$

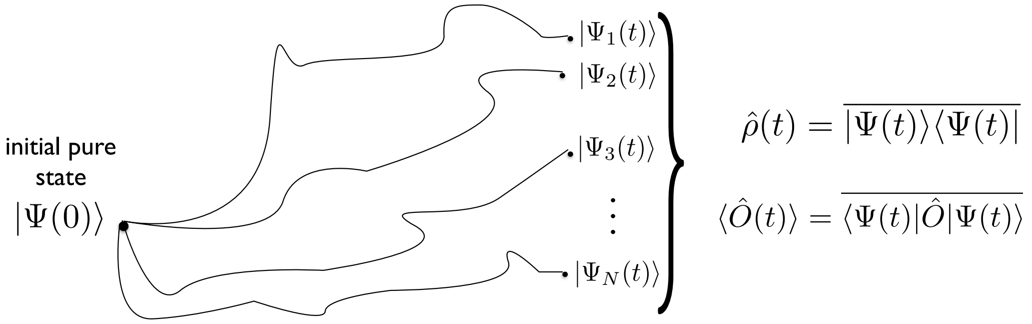

FIGURE 2.2: Schematic representation of how to calculate physical quantities with the SSE.

where the new set of bath operators is given by $\hat{V}_a = \lambda\sqrt{d_a}\sum_b U_{ab}\hat{S}_b$. It should be emphasised that the stochastic processes are included in $\mathrm{d}W_a = (-i/\sqrt{d_a})\sum_j U^{\dagger}_{ja}\gamma_j \mathrm{d}t$ and one can show that those satisfy

$$\overline{\mathrm{d}W_a} = 0, \qquad \overline{\mathrm{d}W_a \mathrm{d}W_b^*} = \delta_{ab}\mathrm{d}t. \tag{2.11}$$

Equation (2.10) does not follow standard rules of calculus. The state $|\phi(t)\rangle$ is a stochastic function and its time derivative is not defined at any instant of time. Additionally, the differential noise $\mathrm{d}W$ scales on average as $\mathrm{d}t^{1/2}$ and thus can be interpreted as the differential increment of an underlying Wiener process. As a result, this differential equation is not tractable with standard calculus and the rules have to be modified according to the *Itô calculus*. Since an in-depth introduction to this calculus will bring us too far; here we will only state the important results of the Itô calculus needed in the following chapters. For a more complete treatment of the Itô formalism one can consult the vast literature on the subject, here we just list some few standard references [30, 35–39]. An important result from this calculus is the Itô chain rule,

$$\mathrm{d}\big(|\phi\rangle\langle\psi|\big) = \big(\mathrm{d}|\phi\rangle\big)\langle\psi| + |\phi\rangle\big(\mathrm{d}\langle\psi|\big) + \big(\mathrm{d}|\phi\rangle\big)\big(\mathrm{d}\langle\psi|\big), \tag{2.12}$$

where ϕ and ψ are two states evolving according to the Markovian SSE (2.10).

After having introduced the NMSSE and the Markovian SSE, we will show how to use such stochastic equations to calculate ordinary time evolution and physical quantities. Due to the coupling to the bath, the system will be driven into a statistical mixture of states although a pure initial state was assumed. From the derivation in Appendix A, one can see that the SSE describes the time evolution of a typical member of this statistical ensemble. As a result, a single evolution of the SSE will not contain information to reconstruct the physical state.

Starting from an initial state $|\Psi(0)\rangle$ of the system, the SSE will evolve the state in a non-deterministic way due to the influence of dissimilar stochastic processes, leading to different trajectories as shown in Fig. 2.2. Only on average, indicated by the over-line, one can gain physical information from the stochastic time evolution. For example, from an average over many realisations of the time evolution of an initial wave function we can calculate the state at time *t*,

$$\hat{\rho}_S(t) = \overline{|\Psi(t)\rangle\langle\Psi(t)|} \equiv \lim_{N\to\infty} \sum_{i=1}^{N} |\Psi_i(t)\rangle\langle\Psi_i(t)|. \tag{2.13}$$

In a similar way, expectation values of an operator $\hat{O}$ can be calculated via

$$\langle\hat{O}\rangle(t) \equiv \overline{\langle\Psi(t)|\,\hat{O}\,|\Psi(t)\rangle}, \tag{2.14}$$

and it is worth mentioning that via the SSE approach it is also possible to describe non-pure initial states, also called mixed states,

$$\hat{\rho}_S(0) = \sum_r p_r\,|\Psi^r(0)\rangle\langle\Psi^r(0)|, \tag{2.15}$$

where p_r is the fraction of the ensemble in each pure state $|\Psi^r(0)\rangle$. The time evolution of the mixed state can be calculated as

$$\hat{\rho}_S(t) = \sum_r p_r\,\overline{|\Psi^r(t)\rangle\langle\Psi^r(t)|}. \tag{2.16}$$

After discussing how to calculate the state of the system, $\hat{\rho}_S(t)$, we might ask what is the related equation of motion for the density operator corresponding to the NMSSE or Markovian SSE. Those master equations can be derived from first principles in a way similar to the SSEs starting from the von Neumann equation for the density operator of the total system. Under the assumptions of weak system–bath interaction, uncorrelated initial states at time $t = 0$ of the full density operator, and vanishing averages of bath operators to first order, the equation of motion for the reduced density operator $\hat{\rho}$ of the system up to second order in the coupling parameter λ is given by [30–32, 40]:

$$\partial_t\hat{\rho}_S(t) = -i\big[\hat{H}_S, \hat{\rho}_S(t)\big] + \lambda^2 \sum_a \big[\hat{S}_a, \hat{M}_a^\dagger(t) - \hat{M}_a(t)\big]. \tag{2.17}$$

Here we have defined

$$\hat{M}_a(t) \equiv \sum_b \int_0^t \mathrm{d}\tau \, C_{ab}(\tau) \, e^{-i\hat{H}_S\tau} \, \hat{S}_b \, \hat{\rho}_S(t-\tau) \, e^{i\hat{H}_S\tau}. \tag{2.18}$$

As in Eq. (2.6) the change of the system at time *t* depends on the history of the state $\rho_S(\tau)$, and so we will name Eq. (2.17) the **non-Markovian master equation** (**NMME**). Alternatively, one can show the correspondence between the NMME and the NMSSE by performing a perturbative expansion in λ [34] of the time evolution operator up to second order.

On the other hand, a Markovian master equation can be obtained by assuming that the bath-correlation function is δ-correlated in the NMME leading to the so-called **Lindblad master equation** [41]

$$\partial_t \hat{\rho}_S = -i[\hat{H}_S, \hat{\rho}_S] - \frac{1}{2} \sum_{a,b} D_{ab} \Big\{ \hat{S}_b \hat{S}_a \hat{\rho}_S + \hat{\rho}_S \hat{S}_b \hat{S}_a - 2\hat{S}_a \hat{\rho}_S \hat{S}_b \Big\}. \tag{2.19}$$

This is the most general type of a Markovian master equation which is known to preserve not only the norm but also positivity and hermiticity. Alternatively, the Lindblad master equation can also be derived from the Markovian SSE using Itô's calculus.

2.2 Thermal Relaxation Dynamics

From fundamental thermodynamic considerations [42, 43] we know that when bringing two objects in contact with each other, they will both equilibrate at the same temperature. Hence, we expect our open quantum system in contact with the equilibrated heat bath to evolve towards some steady state that coincides with its thermal equilibrium at the same temperature *T* of the heat bath,

$$\lim_{t\to\infty} \hat{\rho}_S(t) = \frac{e^{-\beta \hat{H}'_S}}{\mathrm{Tr}_S e^{-\beta \hat{H}'_S}} = \hat{\rho}_S^{\mathrm{eq}}. \tag{2.20}$$

This dynamic towards thermal equilibrium is a non-equilibrium process, called thermal relaxation or in short, thermalisation. The Hamiltonian $\hat{H}'_S$ entering the equilibrium state is not exactly the system Hamiltonian, since the coupling slightly changes the energy spectrum of the system. This energy shift is known as the Lamb shift and will be neglected in the following.

This and the following subsection are based on my master thesis "Stochastic Approaches to Thermal Relaxation of Open Quantum Systems".

In order to describe realistic open systems and accordingly introduce the temperature in the description of the dynamics, the equation of motion should ensure thermalisation. Considering the approximations applied in the derivation of the 'open equations' in section 2.1, the question arises of whether those equations are still able to describe the thermal relaxation process correctly.

In order to understand those processes, we are interested in the conditions for thermal relaxation and how they enter the open equations of motion. The coupling of the system with the environment enters the equation of motion only through three quantities, namely the bath-correlation function $C_{ab}(\tau)$, the noise, and the system's coupling operators $\hat{S}_a$. However, the noise is on average determined by the bath-correlation function and one naturally expects that the operators $\hat{S}_a$ from the Hilbert space of the system do not contain information about the environment, like for example its temperature. Therefore, the bath-correlation function is the only quantity that describes the coupling from the side of the environment and hence thermalisation has to be highly dependent on its structure and how it enters the equation of motion. Of course, the coupling operators $\hat{S}_a$ can hinder the establishment of thermal equilibrium when chosen in an inaccurate way. However they should not contain environmental information like the temperature of the environment.

As we have seen before, the SSE describes an ensemble of wave functions evolving under the influence of distinct stochastic processes. Consequently, only on average one will be able to judge whether or not thermal equilibrium is reached and thus we will use the NMME for the discussion of thermal relaxation processes, which is equivalent to the NMSSE on average. As we are interested in the long-time dynamics, it is sufficient to investigate thermal relaxation in the limit $t \to \infty$, where the condition

$$\lim_{t\to\infty} \frac{\mathrm{d}\hat{\rho}_S^{\mathrm{eq}}}{\mathrm{d}t} = 0 \tag{2.21}$$

indicates that the thermal state is a steady state of the dynamics. However, this assumption does not guarantee that the equation of motion thermalises all initial states. Condition (2.21) and the fact that the equilibrium density operator commutes with the system Hamiltonian lead to a necessary condition for the NMME (and also NMSSE) to ensure thermal relaxation,

$$0 = \lim_{t\to\infty} \frac{\mathrm{d}\hat{\rho}_S^{\mathrm{eq}}}{\mathrm{d}t} = \sum_{\alpha} \left(\hat{K}_a \hat{\rho}_S^{\mathrm{eq}} \hat{S}_a + \hat{S}_a \hat{\rho}_S^{\mathrm{eq}} \hat{K}_a^{\dagger} - \hat{S}_a \hat{K}_a \hat{\rho}_S^{\mathrm{eq}} - \hat{\rho}_S^{\mathrm{eq}} \hat{K}_a^{\dagger} \hat{S}_a \right) + \mathcal{O}(\lambda^4), \tag{2.22}$$

where

$$\hat{K}_a = \lambda^2 \sum_b \int_0^\infty \mathrm{d}\tau \, C_{ab}(\tau) e^{-i\hat{H}_S\tau} \hat{S}_b e^{i\hat{H}_S\tau}. \tag{2.23}$$

The derivation of the conditions for thermalisation in OQSs and an extensive discussion of the topic can be found in appendix B. Indeed, there we show that a necessary condition for the system to relax towards thermal equilibrium is that $C_{ab}(t,\tau) = C_{ab}(t-\tau)$ and that the power spectrum

$$\widehat{C}_{ab}(\omega) \equiv \int_{-\infty}^{+\infty} \mathrm{d}t \, C_{ab}(t) \, e^{-i\omega t}, \tag{2.24}$$

essentially the Fourier transform of the bath-correlation function, satisfies the detailed-balance condition [32, 44]

$$\widehat{C}_{ab}(-\omega) = e^{\beta\omega} \, \widehat{C}_{ba}(\omega). \tag{2.25}$$

This relation ensures that energy transitions in the system are balanced according to a Boltzmann factor.

In conclusion, in order to correctly describe thermalisation processes the bath-correlation function should satisfy the detailed-balance relation. By the Markovian approximation, $C_{ab}(\tau) \approx \frac{1}{2} D_{ab}\delta(\tau)$, one neglects this property of the bath-correlation function, and therefore, the description of thermal relaxation processes from first principles within Markovian dynamics seems to be questionable, or at least should be done with special care keeping the previous considerations in mind. Note that the detailed-balance relation only guarantees that the equilibrium state is a steady state of the dynamics. However, this does not ensure that all initial states will be driven towards this steady state.

2.3 Microscopic Model for the Coupling

When we want to investigate closed quantum systems we first need to determine the Hamiltonian of the system and then solve the equation of motion. However, for the dynamical investigation of OQS it is also needed to set up the environment and its coupling to the system. Therefore, we will derive in this section the bath-correlation function and the operators $\hat{B}$ (and $\hat{S}$) for the coupling of an electronic system to the electromagnetic field in a three-dimensional cavity of volume V. In the dipole approximation this interaction can be written as

$$\hat{W} = -q \sum_i \hat{\mathbf{r}}_i \otimes \hat{\mathbf{E}}(t), \tag{2.26}$$

where q is the charge of an electron and $\hat{\mathbf{E}}$ is the electric field inside the cavity. In the dipole approximation the wavelength of the electromagnetic field is assumed to be large compared to the system size, hence $\hat{\mathbf{E}}$ is considered to be uniform in space. The electrical field in second-quantised form is [45]

$$\hat{\mathbf{E}}(t) = \sum_k i p_k \big(\hat{b}_k e^{-i\omega_k t} - \hat{b}_k^\dagger e^{i\omega_k t}\big)\mathbf{u}, \tag{2.27}$$

where the k-th field mode inside the cavity with frequency ω_k is created by $\hat{b}_k^\dagger$ and we define $p_k = \sqrt{\omega_k/(2V\epsilon_0)}$. For simplicity, we have assumed that the modes are polarised in the same direction as $\mathbf{u}$. By expanding the operator $\hat{\mathbf{r}}$ in a complete basis of the system, one can write the interaction term Eq. (2.26) as

$$\hat{W} = -q \sum_{l,p} \mathbf{u} \cdot \langle\psi_l|\hat{\mathbf{r}}|\psi_p\rangle \hat{\epsilon}_l^\dagger \hat{\epsilon}_p \otimes \sum_k i p_k \big(\hat{b}_k e^{-i\omega_k t} - \hat{b}_k^\dagger e^{i\omega_k t}\big) = \hat{S} \otimes \hat{B}, \tag{2.28}$$

where $\epsilon_l^\dagger$ creates an electron in the system in the state $|\psi_l\rangle$. These states form an orthonormal basis of the system Hamiltonian. Here, it should be emphasised that Eq. (2.28) is already in the required bilinear form for the coupling, as assumed in the derivation of the SSE. From Eq. (2.28) we can immediately read off the form of the operators $\hat{S}$ and $\hat{B}$.* In order to have access to the bath-correlation function, we need to calculate

$$\begin{aligned} C(t,\tau) &= \mathrm{Tr}_B[\hat{\rho}_B^{\mathrm{eq}}\, \hat{B}(t)\, \hat{B}(\tau)] \\ &= -\mathrm{Tr}_B\Big[\hat{\rho}_B^{\mathrm{eq}} \sum_{k,j} p_k p_j \big(\hat{b}_k e^{-i\omega_k t} - \hat{b}_k^\dagger e^{i\omega_k t}\big)\big(\hat{b}_j e^{-i\omega_j \tau} - \hat{b}_j^\dagger e^{i\omega_j \tau}\big)\Big]. \end{aligned} \tag{2.29}$$

Evaluating this in the bosonic many-particle basis of the bath and replacing the sum over the bath modes ω_k by an integral over frequency yields

$$C(t,\tau) = \frac{1}{2\epsilon_0 \pi^2} \int_0^{\omega_c} \mathrm{d}\omega\, \omega^3 \Big\{ \big[n_B(\beta\omega) + 1\big]\, e^{-i\omega(t-\tau)} + n_B(\beta\omega)\, e^{i\omega(t-\tau)} \Big\}, \tag{2.30}$$

where we have inserted the density of states in the cavity, ω^2/π^2 and $n_B(\beta\omega) \equiv 1/(e^{\beta\omega} - 1)$ is the Bose–Einstein distribution function. Furthermore, we have introduced a cutoff frequency

---

*Here we have dropped the sum over many bath operators. A different choice could be made here.

ω_c to be consistent with the dipole approximation, restricting the wavelengths of the bath modes to be larger than the system size. As the former integral cannot be evaluated analytically, we will calculate the power spectrum of this bath-correlation function,

$$\widehat{C}(\omega) = \frac{|\omega|^3}{\pi \epsilon_0} \big[n_B(\beta|\omega|) + \Theta(-\omega) \big] \quad \text{for} \quad |\omega| < \omega_c, \tag{2.31}$$

where $\Theta(\omega)$ is the Heaviside step function. For $|\omega| > \omega_c$, the power spectrum is set to vanish. I would like to point out that increasing ω_c does not change the relaxation dynamics as long as ω_c is larger than the energy differences in the system and hence does not exclude any energy transitions. One can easily show that the detailed-balance relation (2.25) is satisfied by this power spectrum and hence can be used to describe thermal relaxation processes.

Chapter 3

Thermal Relaxation and Transport within the Time-Convolutionless Stochastic Schrödinger Equation[†]

In this chapter we study thermal relaxation and thermal transport dynamics with a known but rarely used, time-local version of the NMSSE, called **time-convolutionless SSE** (**TCLSSE**). In order to investigate non-Markovian stochastic dynamics it would be advantageous to have a SSE that is local in time but is nevertheless able to reproduce the dynamics induced by a non-Markovian equation. This would allow to study a non-Markovian equation at the cost of a Markovian one. Such an equation has been proposed by Strunz and coworkers [46–48], although it is rarely applied or tested.

A promising application of the TCLSSE is the investigation of the energy transport in nanosystems. For this the system is coupled at its ends locally to two baths kept at different temperatures. The temperature gradient induces a thermal force letting the energy flow from the hot bath to the cold bath. However, before investigating this non-equilibrium situation in section 3.3, we will first test whether the TCLSSE reproduces the relaxation dynamics correctly: In contact with a single bath at a constant temperature, the system should relax to its equilibrium state at the same temperature. We have seen in section 2.2 that there exists a condition which

---

[†] This chapter is based on the article
"Application of a time-convolutionless Schrödinger equation to energy transport and thermal relaxation", Journal of Physics Condensed Matter **26**, 395303 (2014), by R. Biele, C. Timm, and R. D'Agosta.

the memory kernel needs to satisfy for the system to reach thermal equilibrium, the detailed-balance relation. This might no longer be fulfilled when approximations of the memory kernel are made [32, 44], as the history dependence of the equation of motion is essential for thermal relaxation. This raises the question of whether the TCLSSE is capable of correctly describing thermal relaxation dynamics. For this, we study the relaxation behaviour of a simple three-level system within the TCLSSE in section 3.2. This pedagogical work verifies the applicability of the TCLSSE to thermal transport. To set up the theoretical foundation we will show how the dynamics of the TCLSSE and the NMME coincide up to third order in the coupling parameter between the system and the bath.

3.1 Time-Convolutionless Stochastic Schrödinger Equation

The dynamics introduced by the NMME can be obtained not only by a numerical integration of the former but also by the solution of a NMSSE [34]. However, any attempt to solve those two non-Markovian equations requires an enormous numerical effort due to the integral over time, which needs to be evaluated at every time step and for every realisation during the time-propagation. This raises the question of whether there exists a simpler SSE that on average reproduces the dynamics induced by the NMME. Indeed this is the case, as the TCLSSE [46]

$$i\partial_t|\Psi(t)\rangle = \left(\hat{H} + \lambda\sum_a \gamma_a(t)\,\hat{S}_a - i\,\lambda^2\,\hat{\mathfrak{T}}(t)\right)|\Psi(t)\rangle, \tag{3.1}$$

with

$$\hat{\mathfrak{T}}(t) \equiv \sum_{a,b}\hat{S}_a\int_0^t \mathrm{d}\tau\, C_{ab}(\tau)\, e^{-i\hat{H}\tau}\hat{S}_b\, e^{i\hat{H}\tau}, \tag{3.2}$$

reproduces the dynamics induced by the NMME up to third order in the coupling parameter λ. In order to show this, we write the TCLSSE in the interaction picture, $|\Psi_I(t)\rangle = e^{i\hat{H}t}|\Psi(t)\rangle$ and $\hat{S}_a(t) = e^{i\hat{H}t}\hat{S}_a\, e^{-i\hat{H}t}$ and expand the time-evolution operator up to second order in λ,

$$\begin{aligned}|\Psi_I(t)\rangle \;\cong\; \Bigg[&\mathbb{1} - i\lambda\sum_a\int_0^t \mathrm{d}t_1\,\gamma_a(t_1)\,\hat{S}_a(t_1)\\ &-\lambda^2\sum_{a,b}\int_0^t \mathrm{d}t_1\int_0^{t_1}\mathrm{d}t_2\, C_{ab}(t_2)\,\hat{S}_a(t_1)\,\hat{S}_b(t_1-t_2)\\ &-\lambda^2\sum_{a,b}\int_0^t \mathrm{d}t_1\int_0^{t_1}\mathrm{d}t_2\,\gamma_a(t_1)\,\hat{S}_a(t_1)\,\gamma_b(t_2)\,\hat{S}_b(t_2)\Bigg]|\Psi_I(0)\rangle + \mathcal{O}(\lambda^3).\end{aligned}$$

In order to calculate the ME that corresponds to the TCLSSE, we will insert this expansion into the expression for the density operator of the system, $\hat{\rho}_I(t) = \overline{|\Psi_I(t)\rangle\langle\Psi_I(t)|}$. By performing the average, using the properties of the noise and the identity $C_{ab}(\tau,t) = C^*_{ba}(t,\tau)$, and differentiating with respect to *t*, we arrive finally at

$$\begin{aligned}\partial_t\hat{\rho}_I(t) &= \lambda^2\sum_{a,b}\int_0^t \mathrm{d}\tau\,\Big[C_{ab}(t,\tau)\,\hat{S}_b(\tau)\,\hat{\rho}_I(0)\,\hat{S}_a(t) - C_{ab}(t,\tau)\,\hat{S}_a(t)\,\hat{S}_b(\tau)\,\hat{\rho}_I(0)\\ &\qquad + C^*_{ab}(t,\tau)\,\hat{S}_a(t)\,\hat{\rho}_I(0)\,\hat{S}_b(\tau) - C^*_{ab}(t,\tau)\,\hat{\rho}_I(0)\,\hat{S}_b(\tau)\,\hat{S}_a(t)\Big] + \mathcal{O}(\lambda^4).\end{aligned}$$

I would like to point out that the averages of the terms proportional to λ^3 vanish. Furthermore, replacing $\rho_I(0)$ by $\rho_I(\tau) + \mathcal{O}(\lambda^2)$ does not change the equation up to order λ^3. Finally, by returning to the Schrödinger picture we arrive at the NMME up to order λ^3, i.e., higher than the order up to which these equations are valid anyway. Indeed, the NMME and the NMSSE are usually derived as a second-order expansion in the coupling parameter λ. This is remarkable since one might expect a more complex time-non-local SSE to be required for reproducing the dynamics of the NMME. Still, the TCLSSE is local in time, i.e., the operator $\hat{\mathfrak{T}}(t)$ does not depend on the state of the system at previous times and can thus be calculated once before the numerical integration and be used for each realisation of the stochastic process. This reduces the numerical cost of solving each realisation of the TCLSSE to that of a Markovian SSE [34, 40].

We note that at the same level of approximation, λ^3, we can derive a time-convolutionless master equation instead of the non-local NMME. However, since in general the density matrix and the operators $\hat{S}_a$ do not commute, the integral over time still contains the density matrix in a complicated manner. From a numerical point of view, the solution of this equation is therefore not simpler than that of a NMME. The equivalence of the NMME and the time-convolutionless master equation is a generalisation of the result that a time-convolutionless Pauli master equation, i.e., a master equation for the diagonal components of the density matrix only, can be proven to be equivalent to a Nakajima–Zwanzig–Markov Pauli master equation to second order in λ [49].

3.2 Time-Convolutionless Description of Thermal Relaxation

As the condition of thermal relaxation in open quantum system is connected with the memory kernel of the equation of motion, in this section, we will test whether the TCLSSE is capable of correctly describing relaxation dynamics. This will then allow us to study thermal transport within the TCLSSE approach in the next section.

In the following, we consider an electronic system coupled to the electromagnetic field in a cavity. This three-dimensional cavity acts as the environment at a certain temperature, *T*. As we have shown in subsection 2.3, the power spectrum for the cavity is given by

$$\widehat{C}(\omega) = \frac{|\omega|^3}{\pi\epsilon_0}\big[n_B(\beta|\omega|) + \theta(-\omega)\big] \quad \text{for} \quad |\omega| < \omega_c, \tag{3.3}$$

where ω_c is a cutoff frequency determined by the dimensions of the system. For this power spectrum the detailed-balance condition (2.25) is satisfied. In order to solve the TCLSSE one needs to generate the noise which is connected with the bath-correlation function as defined in Eq. (2.7). One can easily prove that the noise $\gamma(t)$ can be generated by

$$\gamma(t) = \int_{-\infty}^{+\infty} \frac{\mathrm{d}\omega}{\sqrt{2\pi}} \sqrt{\widehat{C}(\omega)}\, x(\omega)\, e^{i\omega t}, \tag{3.4}$$

where $x(\omega)$ is a white-noise process in the frequency domain satisfying

$$\overline{x(\omega)} = 0, \quad \overline{x(\omega)x(\omega')} = 0, \quad \overline{x^*(\omega)x(\omega')} = \delta(\omega - \omega'). \tag{3.5}$$

From a numerical point of view, the generation of this coloured noise requires the calculation of the Fourier transform in Eq. (3.4). In order to verify the agreement between the power spectrum (3.3) and the power spectrum of the noise generated by (3.4), we perform a Fourier transform of the time-domain signal and compared it to our target. Figure 3.1 shows that the agreement is excellent.

For the electronic system we consider a three-site spinless tight-binding chain described by the Hamiltonian

$$\hat{H} = -\mathcal{T}\left(\hat{c}_1^\dagger \hat{c}_2 + \hat{c}_2^\dagger \hat{c}_1 + \hat{c}_2^\dagger \hat{c}_3 + \hat{c}_3^\dagger \hat{c}_2\right), \tag{3.6}$$

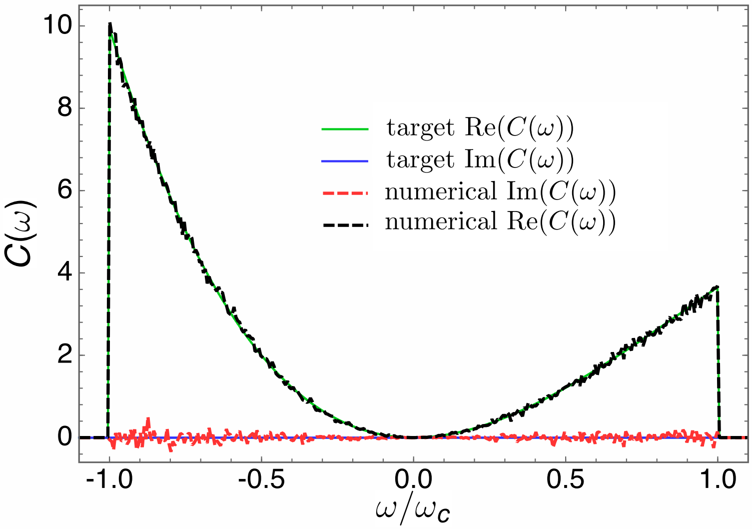

FIGURE 3.1: Comparison between the target, Eq. (3.3), (solid lines) and the Fourier transform of the correlation function obtained from Eq. (3.4) by averaging over 90 000 realisations of the noise (dashed lines). (Plot reused from [50])

where the operator $\hat{c}_i^\dagger$ creates an electron at site i, and we assume a single electron to be present. This system is coupled to the electromagnetic field of the cavity by

$$\hat{S} = -q \sum_{i,j} \mathbf{u} \cdot \langle W_i | \mathbf{r} | W_j \rangle \, \hat{c}_i^\dagger \hat{c}_j, \tag{3.7}$$

where $|W_i\rangle$ is single-particle state localised at site i. For simplicity, we assume that each relevant mode of the cavity has the same polarisation direction $\mathbf{u}$, parallel to the tight-binding chain. Note that the form of this operator should be immaterial for the establishment of thermal equilibrium, which is only determined by the power spectrum.

In Fig. 3.2, the occupation probabilities of the three eigenstates of the Hamiltonian are shown in the one-electron sector as a function of time calculated using the TCLSSE (dashed lines) and the NMME (solid lines), respectively. For the TCLSSE, the results have been obtained by averaging over 90 000 independent realisations of the noise. We have used the parameters $\beta = 1$, $\omega_c = 1$, $\mathcal{T} = 1$, $\epsilon_0 = 1$ and $\lambda = 0.1$ and we have employed the Euler algorithm [51, 52] with time step $\Delta t = 0.005$ to numerically solve the equations. We have chosen an arbitrary pure state as the initial state, $|\Psi(0)\rangle = 0.94\,|1\rangle + 0.2\,|2\rangle + 0.28\,|3\rangle$, where $|i\rangle$ represents the i-th eigenstate of the Hamiltonian, where the eigenenergies satisfy $\epsilon_1 \leq \epsilon_2 \leq \epsilon_3$.

The dynamics induced by the NMME and the TCLSSE are in good agreement: The small discrepancies in the numerical solutions are due to the finite number of realisations we have

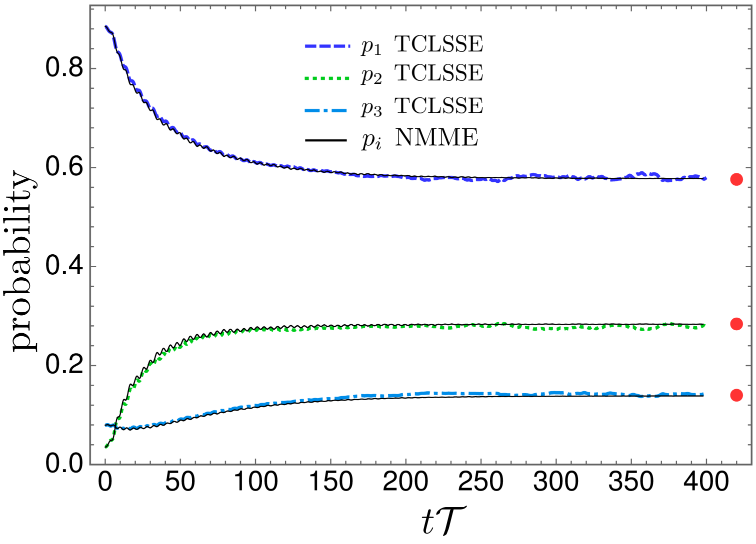

FIGURE 3.2: Dynamics of the occupation probabilities p_1, p_2, p_3 of the eigenstates of the Hamiltonian (3.6) in the one-electron sector calculated from the evolution of the TCLSSE (dashed lines) and the NMME (solid lines) with the power spectrum given by Eq. (3.3). The eigenstates are labeled such that the eigenenergies satisfy $\epsilon_1 \leq \epsilon_2 \leq \epsilon_3$. The red dots represent the thermal-equilibrium probabilities calculated from Eq. (3.8). The time t is measured in terms of the inverse of the energy constant T. (Figure from [50])

used; the solution of the TCLSSE still contains some noise, as expected. For long times, both formalisms converge to the thermal-equilibrium probabilities

$$p_i^{\text{eq}} = \frac{e^{-\beta\epsilon_i}}{e^{-\beta\epsilon_1} + e^{-\beta\epsilon_2} + e^{-\beta\epsilon_3}}, \tag{3.8}$$

which are indicated by red dots in Fig. 3.2. If we were only interested in the long-time limit, we could have averaged over all times after some equilibration time t_{min} to obtain better statistics, using the ergodic theorem to replace the average over many realisations by an average over time of a single realisation.

3.3 Thermal Transport in a Spin Chain

To show that the TCLSSE can be used to investigate energy transport in open quantum systems, we consider a spin chain in contact with two baths at different temperatures, as shown in Fig. 3.3. The baths are locally connected to the terminal spins of the chain [53, 54]. Energy is transferred between the high-temperature bath, via the spin chain, to the low-temperature bath. Here we assume the baths to be represented by an ensemble of harmonic oscillators with a continuous spectrum. In the long-time regime, we expect the appearance of a steady state of constant energy flow.

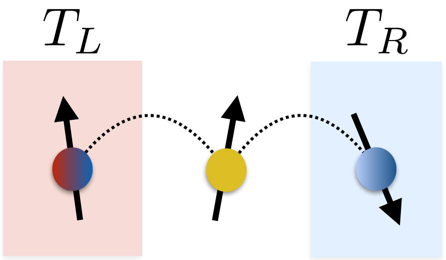

FIGURE 3.3: Interacting spins are connected at the terminal spins to two baths kept at different temperature. This temperature gradient will induce a thermal force in the system which drives an energy current.

The total Hamiltonian of a spin-$1/2$ chain coupled to two baths L and R reads

$$\hat{H}_T = \hat{H}_S + \sum_{i=L,R} \left(\hat{H}_B^{(i)} + \hat{W}^{(i)}\right), \tag{3.9}$$

where the system Hamiltonian is given by

$$\hat{H}_S = \frac{\Omega}{2}\sum_{\mu=1}^{n} \sigma_z^{(\mu)} + \Gamma \sum_{\mu=1}^{n-1} \vec{\sigma}^{(\mu)} \cdot \vec{\sigma}^{(\mu+1)}, \tag{3.10}$$

with $\vec{\sigma} = (\sigma_x, \sigma_y, \sigma_z)$ and the index μ indicating the spin site. The Pauli matrices are given by

$$\sigma_x = \begin{pmatrix} 0 & 1 \\ 1 & 0 \end{pmatrix}, \quad \sigma_y = \begin{pmatrix} 0 & -i \\ i & 0 \end{pmatrix}, \quad \sigma_z = \begin{pmatrix} 1 & 0 \\ 0 & -1 \end{pmatrix}, \tag{3.11}$$

and the spin operators for the n-site chain are

$$\begin{array}{ccccccccc} & & 1 & & 2 & & \mu & & n \\ \sigma_j^{(\mu)} & = & \mathbb{1} & \otimes & \mathbb{1} & \otimes\cdots\otimes & \sigma_j & \otimes\cdots\otimes & \mathbb{1}. \end{array} \tag{3.12}$$

In Eq. (3.10), Ω is the energy associated with a uniform magnetic field aligned along the z direction and Γ is the spin–spin Heisenberg interaction.

The baths are coupled to the spins at the ends of the chain,

$$\hat{W}^{(i)} = \lambda\, \hat{S}^{(i)} \otimes \hat{B}^{(i)} = \lambda\, \sigma_x^{(i)} \otimes \hat{B}^{(i)}, \tag{3.13}$$

where $\sigma_x^{(i=L)} = \sigma_x^{(1)}$, $\sigma_x^{(i=R)} = \sigma_x^{(n)}$, λ is the coupling strength and $\hat{B}$ is the coupling operator from the bath. Here, we consider a bath-correlation function which describes the electromagnetic field of a one-dimensional cavity [32],

$$C^{(i)}(\tau) = \frac{\pi}{2\epsilon_0} \int_0^{\omega_c} \mathrm{d}\omega\, \omega \left[\cos(\omega\tau) \coth\left(\frac{\beta^{(i)}\omega}{2}\right) - i \sin(\omega\tau) \right], \tag{3.14}$$

where $\beta^{(i)}$ is the inverse temperature of bath *i* = *L*, *R*. Accordingly, one can calculate the power spectrum of this bath correlation function as

$$\widehat{C}^{(i)}(\omega) = \frac{\pi^2|\omega|}{\epsilon_0} \left[n_B(\beta^{(i)}|\omega|) + \theta(-\omega) \right] \quad \text{for} \quad |\omega| < \omega_c, \tag{3.15}$$

which is the one-dimensional analogue of Eq. (3.3). One can immediately prove that this correlation function does fulfil the detailed-balance relation and therefore we expect the system to be driven towards thermal equilibrium if the temperatures of the two baths are the same.

To investigate the energy transport, we identify the energy current through a continuity equation for the local energy. Therefore, we define a local Hamiltonian by

$$\hat{h}^{(\mu)} = \frac{\Omega}{2} \sigma_z^{(\mu)} + \frac{\Gamma}{2} \left(\vec{\sigma}^{(\mu)} \cdot \vec{\sigma}^{(\mu+1)} + \vec{\sigma}^{(\mu-1)} \cdot \vec{\sigma}^{(\mu)} \right) \tag{3.16}$$

if μ is different from *n* or 1. We also define

$$\hat{h}^{(1)} = \frac{\Omega}{2} \sigma_z^{(1)} + \frac{\Gamma}{2} \vec{\sigma}^{(1)} \cdot \vec{\sigma}^{(2)} \tag{3.17}$$

and

$$\hat{h}^{(n)} = \frac{\Omega}{2} \sigma_z^{(n)} + \frac{\Gamma}{2} \vec{\sigma}^{(n-1)} \cdot \vec{\sigma}^{(n)} \tag{3.18}$$

so that $\hat{H}_S = \sum_\mu \hat{h}^{(\mu)}$. The time evolution of each local Hamiltonian is given by

$$-\frac{d\hat{h}^{(\mu)}}{dt} = -i \, [\hat{H}_S, \hat{h}^{(\mu)}] = \hat{j}^{(\mu),(\mu+1)} - \hat{j}^{(\mu-1),(\mu)}, \tag{3.19}$$

where energy-current operators have been defined as

$$\hat{j}^{(\mu),(\mu+1)} = \frac{i}{4} \left[\Omega \, (\sigma_z^{(\mu)} - \sigma_z^{(\mu+1)}),\ \Gamma \, \vec{\sigma}^{(\mu)} \cdot \vec{\sigma}^{(\mu+1)} \right]. \tag{3.20}$$

Equation (3.19) has the form of a continuity equation for the energy at site μ and is valid for sites inside the spin chains that are not coupled to a bath.

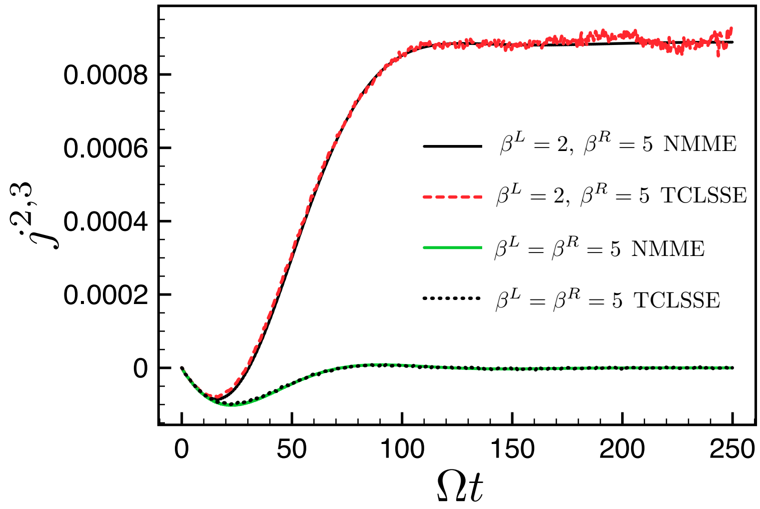

FIGURE 3.4: Dynamics of the energy current of a three-site spin chain coupled locally to two baths for the cases of equal and unequal temperatures, calculated with the NMME (solid lines) and the TCLSSE (dashed and dot–dashed lines). The agreement between the two sets of lines is excellent, in particular at short times. The time *t* is measured in terms of the inverse of the energy constant Ω. (Figure from [50])

In Fig. 3.4 we report the energy current flowing from the second to the third spin of a three-site spin chain. In the equal-temperature case ($\beta^{\mathrm{L}} = \beta^{\mathrm{R}} = 5$, green solid and black dotted lines), a steady state is reached for long times that cooresponds to the thermal equilibrium, and hence no current is flowing through the system. On the other hand, for the case of unequal temperatures ($\beta^{\mathrm{L}} = 2$ and $\beta^{\mathrm{R}} = 5$), the steady state shows a non-zero energy current from the warmer to the colder bath, as expected (black solid and red dashed lines). For the TCLSSE we have averaged over 100 000 independent realisations of the noise and for both calculations we have used the parameter values $\Omega = 1$, $\Gamma = 0.01$, $\lambda = 0.1$, $\epsilon_0 = 1$ and $\omega_c = 6$. Both for the equal-temperature case and for the case with a thermal gradient, we have chosen an initial state populated with the probabilities determined by the equilibrium distribution at the lower temperature. It can been seen that the TCLSSE produces the same dynamics of the energy current as obtained from the NMME in the equilibrium and non-equilibrium regime and hence can be seen as a reliable tool to simulate energy transport with moderate numerical cost.

In conclusion, we have numerically investigated a time-local (time-convolutionless) version of a *non-Markovian* SSE, which correctly describes the approach to thermal equilibrium and energy transport as obtained from the general NMME (2.17). We report two case studies which show that the TCLSSE is a viable alternative for obtaining the exact dynamics of a non-Markovian open quantum system.

Chapter 4

Time-Dependent Thermal Transport Theory[†]

Understanding thermal transport in nanoscale systems presents important challenges to both theory and experiment. As we are increasingly able to probe and manipulate nanoscale systems, an explosion of novel work in the field of nanotechnology has taken place. From macroscopic systems towards the nanoscale, quantum effects such as entanglement and quantum coherence become more important. While at the macroscopic level Kirchhoff's law applies, in the nanoscale world the electrical conductance no longer obeys it, and phase coherence can cause interference effects on electrical transport [1]. The same holds true for thermal transport: While Fourier's law has been empirically postulated in 1822 for bulk materials and derived phenomenologically more than 80 years ago by Peierls, no simple proof of its validity has ever been derived from first principles for the nanoscale [55]. Experimentally and theoretically one has found simple nanoscale systems where Fourier's law has been violated [56–58]. This shows that the theory and simulation of nanoscale thermal transport is at an immature stage and poses deep questions in the overlap between thermodynamics and quantum theory [4, 5]. In particular, the concept of local temperature at the nanoscale appears difficult to justify: Temperature is defined for equilibrated systems. When a thermal gradient is present, this does clearly not apply. Even worse, when dealing with microscopic quantum systems the concept of temperature,

---

[†] This chapter is based on the article
"Time-Dependent Thermal Transport Theory", Physical Review Letters **115**, 056801 (2015), by R. Biele, R. D'Agosta, and A. Rubio.

defined for macroscopic objects, is hard to apply or justify. Therefore, we propose in this chapter a theoretical approach where we replace the temperature gradient with controllable external blackbody radiations. In constructing the formalism we desire certain physical behaviour to be fulfilled by the theory, for example the thermalisation of the system when no temperature gradient is applied. We will show that our approach recovers known physical results, such as the linear relation between the thermal current and the temperature difference of two blackbodies. Furthermore, this theory is not limited to the linear regime and goes beyond it by accounting for non-linear effects and transient phenomena. Since the present approach is general and can be adapted to describe both electron and phonon dynamics, it is a first step towards a unified formalism for investigating thermal and electronic transport at the nanoscale.

It is a common everyday experience that two macroscopic bodies in contact with each other equilibrate in the long-time limit to the same temperature. Microscopically, equilibration means that there is no net energy-flow between the two bodies. But the exchange of energy, in form of small fluctuations, is still present. Since the direction of the energy flow is solely determined by the sign of the difference between the temperatures of the bodies, one can conclude that the absence of an energy flow implies that the two bodies have the same temperature. This law of thermodynamics provides an operative definition of the temperature difference. What makes thermal transport at the nanoscale a difficult theoretical problem is that the very basic fundamentals of standard thermodynamics cannot be applied, and the idea of thermalisation needs to be reconsidered. Attempts have been made to introduce a position dependent temperature, but they do not provide a satisfactory definition of local temperature. Indeed, the concepts of local Hamiltonian, useful to define a local energy density, local thermal current, and local nanoscale thermal gradient are not uniquely or hardly defined as we will see later. Recently, a way out, restricted to small thermal gradients, has been put forward using an effective gravitational field, as originally proposed by Luttinger [59], that mimics the effect of a temperature gradient [60, 61]. Here, we propose an alternative approach where the temperature field is established by two or more blackbodies of known thermal properties. Besides thermal transport at the nanoscale, this theory can be used to understand energy transport in cold atoms, biological, or optical systems. We first consider the equation of motion for an electronic system coupled to classical and quantum fields and see what is the simplest model that allows to introduce a temperature in the system and leads to thermal relaxation. After clarifying this, we lay down the basic formalism for our thermal transport theory and then consider a simple one-electron model system. However, our theory is not limited to this, it can be directly extended to the general framework of time-dependent current-density functional theory [62–64] to consider also many-body systems. More important, our approach is not restricted to linear response or weak coupling regimes, and we can easily investigate the interesting cases of both strong coupling — recovering the Kramers' turnover [65] — and large temperature gradients. Finally, we have access to the full dynamics of the system. Therefore we can investigate transient regimes, usually unaccessible to other formalisms. Last but not least, our theory can be applied to investigating the phonon thermal transport. In this respect, it could be seen as a first step towards a unified *ab initio* formalism for thermal and electric transport.

4.1 Formalism

A blackbody, according to its original definition by Kirchhoff in 1860 [66], is a macroscopic object that absorbs all the radiation impinging on it. In thermal equilibrium the blackbody emits electromagnetic radiation according to Plank's law, whose spectrum is determined solely by the temperature of the blackbody and not by its shape or composition [67, 68]. If we enclose the blackbody by an optical cavity made of reflecting walls, the radiation inside the cavity thermally equilibrates with the blackbody radiation, and any object in this cavity will also thermalise. Hence, by changing the temperature of the blackbody we control both the temperature inside the cavity and that of the object. When thermal equilibrium is reached, at any point in the cavity the electromagnetic radiation follows Planck's law with the temperature of the blackbody. Finally, we can extract or estimate a local temperature from the observation of the energy radiation and this serves us in the following to construct a formalism for thermal transport. Our thermometer, or thermal source, is indeed described as a blackbody which radiates according to its temperature.

A possible thermal-transport configuration can be seen in Fig. 4.1. Two blackbodies radiate according to their temperature onto an electronic system from the left and right side. This will drive the system out of equilibrium and energy will begin to flow in the system. In order to allow for spontaneous and stimulated emission and absorption of energy, the system is interacting with the surroundings.

To begin with, we consider an electronic system, S, coupled to any strength to the blackbody radiation, labeled by BB, and weakly to the free field of the environment, labeled by E. The

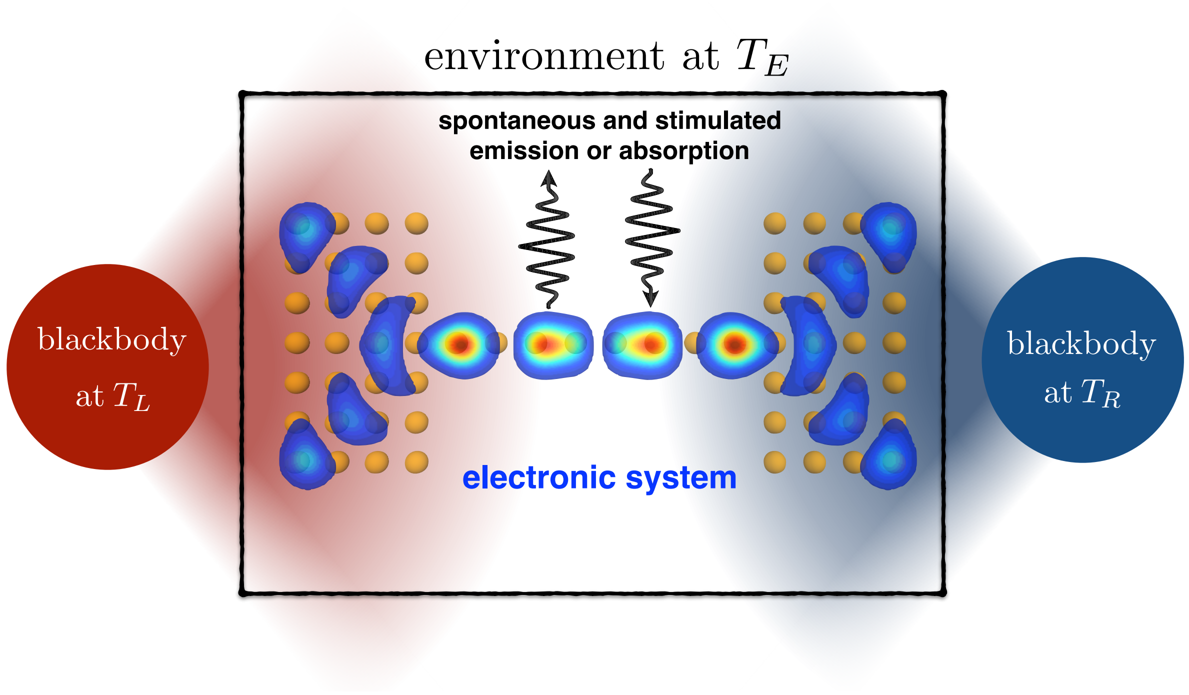

FIGURE 4.1: Two blackbodies, radiating according to their temperature, will introduce a thermal force in the electronic system and heat will flow from the hot to cold regions. At the same time the system is connected with the surrounding to allow for spontaneous and stimulated emission and absorption.

dynamics of the blackbody radiation is determined solely by the blackbody itself. Here, we assume the macroscopic parameters of the blackbody to be constant in time and treated classically. The blackbodies are far away from the system and there is no back-coupling from the system to the blackbodies. At the same time, the system is embedded in a bosonic environment, kept at constant temperature T_E, with which the system can exchange energy via spontaneous and stimulated emission or absorption. The total Hamiltonian where we treat the environment quantum-mechanically, is

$$\hat{H}_T = \sum_{i=1}^{N} \left[\frac{1}{2} \left(\hat{\mathbf{p}}_i - \hat{\mathbf{A}}_E(\mathbf{r}_i) - \mathbf{A}_{\mathrm{BB}}(\mathbf{r}_i, t) \right)^2 + U(\mathbf{r}_i, t) \right] + \hat{H}_E, \tag{4.1}$$

where $\hat{H}_E = \sum_{\mathbf{k},s} \omega_{\mathbf{k}} \hat{b}^{\dagger}_{\mathbf{k},s} \hat{b}_{\mathbf{k},s}$ is the Hamiltonian of the free field of the environment and $\hat{\mathbf{A}}_E$ its corresponding vector potential. In addition, we include in the model an external potential U and $\mathbf{A}_{\mathrm{BB}}$ describes the electromagnetic radiation (treated classically) emitted by the blackbody sources. In the Coulomb gauge, $\boldsymbol{\nabla} \cdot \mathbf{A} = 0$, one can separate the total Hamiltonian,

$$\hat{H}_T = \hat{H}_S + \hat{H}_E + \hat{I}_{SE}, \tag{4.2}$$

where we have included the system–blackbody interaction in the system Hamiltonian,

$$\hat{H}_S = \sum_{i=1}^{N} \Big(\hat{\mathbf{p}}_i^2/2 + U(\mathbf{r}_i, t) - \mathbf{A}_{\mathrm{BB}}(\mathbf{r}_i, t) \cdot \hat{\mathbf{p}}_i\Big), \tag{4.3}$$

and the quadratic term $\mathbf{A}_{\mathrm{BB}}^2$ in the external potential U. The interaction between the system and environment consists of two terms

$$\hat{I}_{SE} = \sum_{i=1}^{N} \Big(- \hat{\mathbf{p}}_i \cdot \hat{\mathbf{A}}_E(\hat{\mathbf{r}}_i) + \frac{1}{2}\hat{\mathbf{A}}_E^2(\hat{\mathbf{r}}_i)\Big), \tag{4.4}$$

where we have neglected the direct interaction of the environmental field with the blackbody radiation. This can be justified by observing that the photon–photon interaction is small. Consequently the contributions of the terms where, e.g., a photon from the blackbody scatters with the free field and then is absorbed by the system, are negligible. In second-quantised form the vector-field of the environment can be written as

$$\hat{\mathbf{A}}_E(\mathbf{r}) = \sum_{\mathbf{k},s} p_{\mathbf{k},s} \left(\hat{b}_{\mathbf{k},s} \exp(i\mathbf{k} \cdot \mathbf{r}) + \hat{b}_{\mathbf{k},s}^{\dagger} \exp(-i\mathbf{k} \cdot \mathbf{r})\right) \boldsymbol{\epsilon}_{\mathbf{k},s}, \tag{4.5}$$

where $p_{\mathrm{k}} = \sqrt{2\pi/(\omega_k V)}$ and $\hat{b}_{\mathbf{k}}^{\dagger}$ is the creation operator for a free-field mode with polarisation direction $\boldsymbol{\epsilon}_{\mathbf{k},s}$. Finally, by exploiting the field expansion $\hat{\Psi} = \sum_{\alpha} \hat{c}_{\alpha}(t)\phi_{\alpha}(\mathbf{r})$, the system–environment interaction can be written, in the Coulomb gauge as

$$\begin{aligned} \hat{I}_{SE} &= \int \mathrm{d}V\, \hat{\Psi}^{\dagger}(\mathbf{r}, t)\Big[- \hat{\mathbf{p}} \cdot \hat{\mathbf{A}}_E(\mathbf{r}) + \hat{\mathbf{A}}_E^2(\mathbf{r})\Big] \hat{\Psi}(\mathbf{r}, t) \\ &= \big(I_{SE}\big)_a + \big(I_{SE}\big)_b, \end{aligned} \tag{4.6}$$

where

$$\big(\hat{I}_{SE}\big)_a = \sum_{\alpha,\beta,\mathbf{k},s} \hat{c}_{\alpha}^{\dagger}(t)\hat{c}_{\beta}(t)\Big\{\hat{b}_{\mathbf{k},s}\, \tilde{g}_{\alpha\beta,\mathbf{k},s} + \hat{b}_{\mathbf{k},s}^{\dagger}\, \tilde{g}_{\alpha\beta,-\mathbf{k},s}\Big\}, \tag{4.7}$$

$$\tilde{g}_{\alpha\beta,\mathbf{k},s} = i p_{\mathbf{k}} \int \mathrm{d}V \phi_{\alpha}^{*}(\mathbf{r}) e^{i\mathbf{k}\cdot\mathbf{r}} \boldsymbol{\epsilon}_{\mathbf{k},s} \cdot \boldsymbol{\nabla}\phi_{\beta}(\mathbf{r}), \tag{4.8}$$

and

$$\begin{aligned}\left(\hat{I}_{SE}\right)_b \;=\; \sum_{\substack{\alpha,\beta,\mathbf{k}_1\\ \mathbf{k}_2,s_1,s_2}} c^\dagger_\alpha(t)\hat{c}_\beta(t)\Big\{ & \hat{b}_{\mathbf{k}_1,s_1}\hat{b}_{\mathbf{k}_2,s_2}\, h_{\alpha,\beta,\mathbf{k}_1,\mathbf{k}_2,s} + \hat{b}_{\mathbf{k}_1,s_1}\hat{b}^\dagger_{\mathbf{k}_2,s_2}\, h_{\alpha,\beta,\mathbf{k}_1,-\mathbf{k}_2,s} \\ & + \hat{b}^\dagger_{\mathbf{k}_1,s_1}\hat{b}_{\mathbf{k}_2,s_2}\, h_{\alpha,\beta,-\mathbf{k}_1,\mathbf{k}_2,s} + \hat{b}^\dagger_{\mathbf{k}_1,s_1}\hat{b}^\dagger_{\mathbf{k}_2,s_2}\, h_{\alpha,\beta,-\mathbf{k}_1,-\mathbf{k}_2,s}\Big\},\end{aligned} \tag{4.9}$$

$$h_{\alpha,\beta,\mathbf{k}_1,\mathbf{k}_2,s} = p_{\mathbf{k}_1}p_{\mathbf{k}_2}\int \mathrm{d}V\phi^*_\alpha(\mathbf{r})\phi_\beta(\mathbf{r})e^{i(\mathbf{k}_1+\mathbf{k}_2)\cdot\mathbf{r}}\boldsymbol{\epsilon}_{\mathbf{k}_1,s_1}\cdot\boldsymbol{\epsilon}_{\mathbf{k}_2,s_2}. \tag{4.10}$$

Here, the operators $\hat{c}^\dagger_\alpha$ create the α-th energy eigenstate of the initial Hamiltonian $\hat{H}_S(0)$. The energy eigenstates will serve as a natural basis set for our following considerations. These former equations describe the interaction of a bosonic environment with the electronic system under the influence of the time-dependent classical blackbody field. One has to realise that those cannot be solved exactly and approximations are needed. However, as we are interested in thermal transport, we need to ensure thermalisation and therefore we will investigate in the following whether those equations are capable of describing thermalisation correctly.

First of all, we will assume that the system size is small in comparison to the wavelengths of the electromagnetic field (dipole approximation). Going beyond this dipole approximation is straightforward, but for the sake of simplicity we will use it in the following. Furthermore, we will neglect the quadratic terms in the free-field, $\hat{\mathbf{A}}_E$, as we assume that the coupling to the environment is small. This leads to

$$\hat{I}_{SE} = \sum_{\alpha,\beta,\mathbf{k},s} g_{\alpha\beta,\mathbf{k},s}\,\hat{c}^\dagger_\alpha\hat{c}_\beta\left(\hat{b}_{\mathbf{k},s} + \hat{b}^\dagger_{\mathbf{k},s}\right), \tag{4.11}$$

where we have defined a new coupling constant, $g_{\alpha\beta,\mathbf{k},s} = ip_{\mathbf{k}}\int \mathrm{d}V\phi^*_\alpha(\mathbf{r})\boldsymbol{\epsilon}_{\mathbf{k},s}\cdot\boldsymbol{\nabla}\phi_\beta(\mathbf{r})$.

As we are interested only in the system dynamics, we will examine the dynamics of the expectation value of the operator $\hat{c}^\dagger_\alpha\hat{c}_\beta$,

$$f_{\alpha\beta} = \langle\hat{c}^\dagger_\alpha\hat{c}_\beta\rangle. \tag{4.12}$$

This can be derived from the equation of motion for $\hat{c}^\dagger_\alpha\hat{c}_\beta$,

$$i\partial_t f_{\alpha\beta} = \langle[\hat{c}^\dagger_\alpha\hat{c}_\beta,\hat{H}_S]\rangle + \sum_{\gamma,\mathbf{k}}\left\{g_{\beta\gamma,\mathbf{k}}\Big(\langle\hat{b}_{\mathbf{k}}\hat{c}^\dagger_\alpha\hat{c}_\gamma\rangle + \langle\hat{b}^\dagger_{\mathbf{k}}\hat{c}^\dagger_\alpha\hat{c}_\gamma\rangle\Big) - g_{\gamma\alpha,\mathbf{k}}\Big(\langle\hat{b}_{\mathbf{k}}\hat{c}^\dagger_\gamma\hat{c}_\beta\rangle + \langle\hat{b}^\dagger_{\mathbf{k}}\hat{c}^\dagger_\gamma\hat{c}_\beta\rangle\Big)\right\}, \tag{4.13}$$

where we included the spin index s in the components of $\mathbf{k}$. The solution of the former equation requires the knowledge of the dynamics of $\hat{b}_{\mathbf{k}}\hat{c}^{\dagger}_{\alpha}\hat{c}_{\beta}$, which is readily obtained from Heisenberg's equation of motion,

$$\begin{aligned} i\partial_t \hat{b}_{\mathbf{k}}\hat{c}^{\dagger}_{\alpha}\hat{c}_{\beta} &= [\hat{b}_{\mathbf{k}}\hat{c}^{\dagger}_{\alpha}\hat{c}_{\beta}, \hat{H}_S] + \omega_{\mathbf{k}}\hat{b}_{\mathbf{k}}\hat{c}^{\dagger}_{\alpha}\hat{c}_{\beta} \\ &\quad + \sum_{\gamma,\delta,\mathbf{l}} g_{\gamma\delta,\mathbf{l}} \Big\{ \hat{c}^{\dagger}_{\alpha}\hat{c}_{\beta}\hat{c}^{\dagger}_{\gamma}\hat{c}_{\delta}\delta_{\mathbf{k},\mathbf{l}} + \Big(\hat{b}_{\mathbf{k}}(\hat{b}_{\mathbf{l}} + \hat{b}^{\dagger}_{\mathbf{l}}) - \delta_{\mathbf{k},\mathbf{l}}\Big)\Big(\hat{c}^{\dagger}_{\alpha}\hat{c}_{\delta}\delta_{\gamma\beta} - \hat{c}^{\dagger}_{\gamma}\hat{c}_{\beta}\delta_{\delta\alpha}\Big)\Big\}. \end{aligned} \tag{4.14}$$

A similar equation holds for $\hat{b}^{\dagger}_{\mathbf{k}}\hat{c}^{\dagger}_{\alpha}\hat{c}_{\beta}$. These equations of motion are not in a closed form, and any attempt to solve them by investigating the dynamics of the operators appearing on the right hand side leads to an infinite hierarchy of equations. For this reason, we decouple the dynamics of the system and the field, i.e., we assume that *

$$\langle \hat{b}_{\mathbf{k}}\hat{b}^{\dagger}_{\mathbf{l}}\hat{c}^{\dagger}_{\alpha}\hat{c}_{\beta}\rangle \approx \langle \hat{b}_{\mathbf{k}}\hat{b}^{\dagger}_{\mathbf{l}}\rangle\langle \hat{c}^{\dagger}_{\alpha}\hat{c}_{\beta}\rangle. \tag{4.15}$$

With this approximation, Eq. (4.14) is solved with a standard integration technique. Furthermore, by using that the initial-state correlation vanishes,

$$\langle \hat{b}^{\dagger}_{\mathbf{k}}\hat{c}^{\dagger}_{\alpha}\hat{c}_{\beta}\rangle(0) = \langle \hat{b}_{\mathbf{k}}\hat{c}^{\dagger}_{\alpha}\hat{c}_{\beta}\rangle(0) = 0, \tag{4.16}$$

and that the environment is in thermal equilibrium,

$$n_B(\omega_{\mathbf{k}}, T_E) = \sum_{\mathbf{l}} \langle \hat{b}_{\mathbf{k}}(\hat{b}_{\mathbf{l}} + \hat{b}^{\dagger}_{\mathbf{l}}) - \delta_{\mathbf{k},\mathbf{l}}\rangle, \tag{4.17}$$

we arrive at

---

*Here, we want to note that this is equivalent to a perturbative expansion up to second order in the coupling parameter g for the equation of motion (4.13).

$$
\begin{aligned}
i\partial_t f_{\alpha\beta} \;=\;& \left\langle \left[\hat{f}, \hat{H}_S \right] \right\rangle_{\alpha\beta} + i \sum_{\mathbf{k},\mathbf{l}} \int_0^t \mathrm{d}\tau \, C_{\mathbf{k},\mathbf{l}}(\tau,t) \Big\langle \Big[\hat{U}(\tau,t)\hat{V}_{\mathbf{l}}\hat{f}(\tau)\hat{U}^\dagger(\tau,t)\hat{V}_{\mathbf{k}} \\
& -\hat{U}(\tau,t)\hat{f}(\tau)\hat{V}_{\mathbf{l}}\hat{U}^\dagger(\tau,t)\hat{V}_{\mathbf{k}} - \hat{V}_{\mathbf{k}}\hat{U}(\tau,t)\hat{V}_{\mathbf{l}}\hat{f}(\tau)\hat{U}^\dagger(\tau,t) \\
& +\hat{V}_{\mathbf{k}}\hat{U}(\tau,t)\hat{f}(\tau)\hat{V}_{\mathbf{l}}\hat{U}^\dagger(\tau,t) \Big] \Big\rangle_{\alpha\beta} \\
& -2 \int_0^t \mathrm{d}\tau \sum_{\gamma,\delta,\sigma,\zeta,\mathbf{k},\mathbf{l}} V^*_{\delta\gamma,\mathbf{k}} V^*_{\sigma\zeta,\mathbf{l}} \sin(\omega_{\mathbf{k}}(t-\tau)) \Big\{ \delta_{\beta\gamma} U_{\delta\alpha}(\tau,t) \langle \hat{c}^\dagger_\alpha \hat{c}_\delta \hat{c}^\dagger_\sigma \hat{c}_\zeta \rangle(\tau) U^*_{\delta\alpha}(\tau,t) \\
& -\delta_{\delta\alpha} U_{\beta\gamma}(\tau,t) \langle \hat{c}^\dagger_\gamma \hat{c}_\beta \hat{c}^\dagger_\sigma \hat{c}_\zeta \rangle(\tau) U^*_{\beta\gamma}(\tau,t) \Big\}. \qquad (4.18)
\end{aligned}
$$

Here, we have introduced the bath-correlation function

$$
\begin{aligned}
C_{\mathbf{k},\mathbf{l}}(\tau,t) &= \left\langle \{ \hat{b}_{\mathbf{k}}(\tau) + \hat{b}^\dagger_{\mathbf{k}}(\tau) \} \{ \hat{b}_{\mathbf{l}}(t) + \hat{b}^\dagger_{\mathbf{l}}(t) \} \right\rangle \\
&= \big(n(\omega_{\mathbf{k}},T) + 1 \big) e^{-i\omega_{\mathbf{k}}(\tau-t)} + n(\omega_{\mathbf{k}},T) e^{i\omega_{\mathbf{k}}(\tau-t)}, \qquad (4.19)
\end{aligned}
$$

and defined $\hat{U}(\tau,t) = \hat{T}_+ e^{-i\int_\tau^t \mathrm{d}t' \hat{H}_S(t')}$, where $\hat{T}_+$ is the time-ordering operator, and we have introduced the hermitian operator $V^*_{\beta\alpha,\mathbf{k}} = g_{\alpha\beta,\mathbf{k}}$. Equation (4.18) describes a fermionic system under the influence of a classical blackbody radiation, where the system can dissipate to or gain energy from the environment. This Heisenberg equation of motion for the expectation value of the operator $\hat{f}$ is quite similar to our NMME for the state of the system. While the terms important for thermalisation describing the spontaneous emission and absorption of a photon from the surrounding proportional to $n(\omega_{\mathbf{k}},T)$ and $n(\omega_{\mathbf{k}},T) + 1$ appear in both equations, additional terms are present in Eq. (4.18) and the time-ordering operator acts in the memory integral. Like we have done in Appendix B, one can show that the thermal equilibrium state is a steady state of this equation of motion when the bath-correlation function fulfils the detailed-balance relation and no temperature gradient is applied by the blackbodies. One can easily prove that the detailed-balance condition is satisfied by our correlation function, Eq. (4.19). Then, without any thermal gradient, the system evolving according to Eq. (4.18) should reach thermal equilibrium with the free field radiation. On the other hand, when external sources introduce a thermal force, the system does not to reach equilibrium in general. However, we expect the system to reach a steady-state regime in the long-time limit. This expectation is rooted in the observation that stimulated and spontaneous emissions grow when the system is strongly driven until a balance is reached between the energy absorbed from the external fields and that emitted.

4.2 Results

In the following we will demonstrate and test the theory on a model system of fundamental importance. We will study heat transport induced by the blackbody fields in a small two dimensional spin-less tight-binding system sketched in Fig. 4.2. First of all, we check whether known results are reproduced. For this, we prove that the system relaxes or not in the long-time limit to its thermal equilibrium, and find that our system also shows a 'Kramers turnover'-like behaviour [65, 69]. as expected. The tight-binding sites are labeled by the numbers one to six, and they are connected via nearest-neighbour hopping. Here, the vector potentials $\mathbf{A}_L$ and $\mathbf{A}_R$ represent the electromagnetic field from two blackbodies at positions x = -∞ and x = +∞ with temperatures T_L and T_R, respectively. In addition, the system is embedded in an environment at temperature T_E.

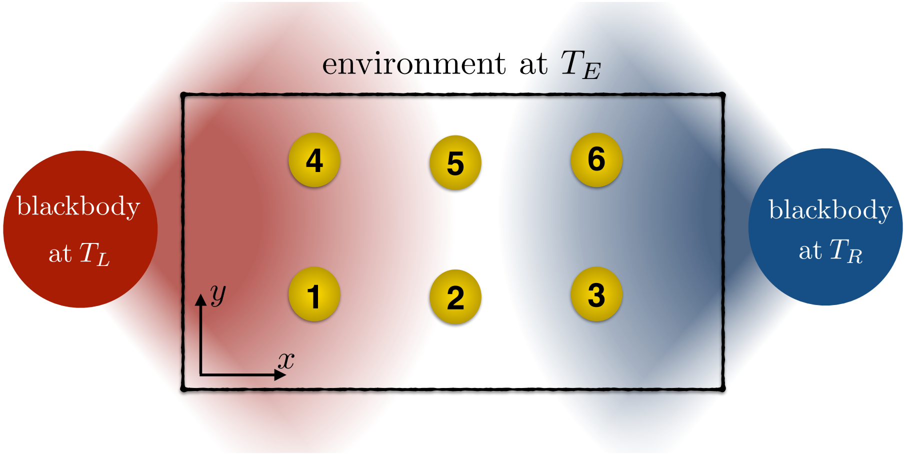

FIGURE 4.2: Sketch of the set-up under consideration. The tight-binding sites are labeled by 1 to 6 and are connected on the left and right side to two blackbody radiations at different temperature, T_L and T_R. At the same time, the system is embedded in an environment at temperature T_E.

As these blackbodies are far away from the system, their fields can be approximated as a superposition of plane waves traveling in positive (or negative) x-direction, weighted according to their temperature,

$$\mathbf{A}_{L,R}(r,t) = \mathbf{E_0} \int \mathrm{d}\Omega \sqrt{\Omega n_B(\Omega, T_{L,R})} \sin\left(\Omega t \pm kx + \phi(\Omega)\right), \tag{4.20}$$

where $\mathbf{E_0}$ = $E_0\mathrm{e}_y$, and E_0 is the strength of the corresponding electric field, e_y is the unit vector in the y-direction, and $\phi(\Omega) \in [0, 2\pi]$ are uncorrelated random phase factors. As before, n_B is the Bose–Einstein distribution. Here, one might use more realistic, and also complicated, models for the correlation of thermal radiation [70, 71]. However as a first test we will work with this simple model. The vector potentials $\mathbf{A}_L$ and $\mathbf{A}_R$ couple to the leftmost and rightmost sites, respectively, and will introduce a local temperature gradient in the system. Note that in general the potentials penetrate into the system, but for this small model, we assume that the system rapidly screens the external radiation. This blackbody radiation enters through the Peierls transformation of the hopping parameter

$$\mathcal{T}_{ij}^{A} = \mathcal{T}_{ij}\, \exp\left(-i \int_{\mathbf{R}_i}^{\mathbf{R}_j} \mathrm{d}\mathbf{r} \cdot \left(\mathbf{A}_L(r,t) + \mathbf{A}_R(r,t)\right)\right), \tag{4.21}$$

into the tight-binding Hamiltonian

$$\hat{H}_S = \sum_{\langle i,j \rangle} \mathcal{T}_{ij}^{A} \hat{c}_i^{\dagger} \hat{c}_j. \tag{4.22}$$

Here, the operator $\hat{c}_i^{\dagger}$ creates an electron at site i with position $\mathbf{R}_i$, and we assume a single electron to be present in the whole system. The sum $\langle i,j \rangle$ denotes summation over nearest neighbours only.

The coupling to the environmental degrees of freedom will be described by a master equation, where the power spectrum, essentially the Fourier transform of Eq. (4.19), is given by

$$\widehat{C}(\omega) = \frac{4|\omega|^3}{c^3}\left[n(|\omega|, T_E) + \Theta(-\omega)\right] \tag{4.23}$$

for $|\omega| < \omega_c$, where $\Theta(\omega)$ is the Heaviside step function and ω_c is a cutoff frequency determined by the dimensions of the system. For $|\omega| > \omega_c$, the power spectrum is set to vanish. This cutoff is necessitated by the assumption made in the dipole approximation that the electromagnetic field is uniform in the region of space occupied by the system. According to Eq. (2.28), the corresponding coupling operator, entering the master equation, is given by

$$\hat{V} = -\sum_{i,j} \mathbf{u} \cdot \langle W_i | \mathbf{r} | W_j \rangle\, \hat{c}_i^{\dagger} \hat{c}_j, \tag{4.24}$$

where $|W_i\rangle$ is the single-particle state localised at site i. As we are only interested in the steady-state energy current through this simple tight-binding system, we approximate the memory kernel of the non-Markovian equation (4.18) by setting $\int_0^t \mathrm{d}\tau \hat{f}(\tau)[\ldots] \to \int_{-\infty}^{\infty} \mathrm{d}\tau \hat{f}(t)[\ldots]$. This approximation does not change the long-time limit of the equation of motion and hence is suitable to study steady-state dynamics [72]. In order to calculate the energy transport one has to define an energy current in the system via the continuity equation. With the local energy-density operator,

$$\hat{h}_i = \frac{1}{2}\sum_{\langle j\rangle}\left(\mathcal{T}^A_{ij}\hat{c}^\dagger_i\hat{c}_j + \text{h.c.}\right), \tag{4.25}$$

one can define the total current in the *x*-direction via

$$\hat{j}^x_T = -\dot{\hat{h}}_1 - \dot{\hat{h}}_4 + \dot{\hat{h}}_3 + \dot{\hat{h}}_6, \tag{4.26}$$

where $\dot{\hat{O}} = i[\hat{H}_S, \hat{O}] + \partial_t\hat{O}$ and $\langle j\rangle$ indicates the sum over nearest neighbours. As a first test of the novel thermal transport theory we examine the relaxation dynamics of the tight-binding system driven by a left and right blackbody radiation kept at temperature k_BT = 10 a.u., the same temperature as the environment. We choose $\mathcal{T}_{ij}$ = 0.5 a.u. as an energy-scale for the system, and for the coupling to the environment we set $\gamma = \sqrt{2/(\pi c^3)}$ = 0.05. For the energy scale of the blackbody radiations, we have normalised both left and right radiation with the time-averaged Poynting vector, ⟨S⟩, set to 15/(μ_0· c). In Fig. 4.3 the dynamics of the occupation probabilities of the eigenstates of the Hamiltonian (4.22) in the one-electron sector is shown for the system without thermal gradient. One can see that the system relaxes towards a steady state, characterised by zero energy transport in the system, which can be seen in the inset of Fig. 4.3. Here, *N* indicates the number of realisations of the stochastic noise we have averaged over to mimic the blackbody radiation in Eq. (4.20).

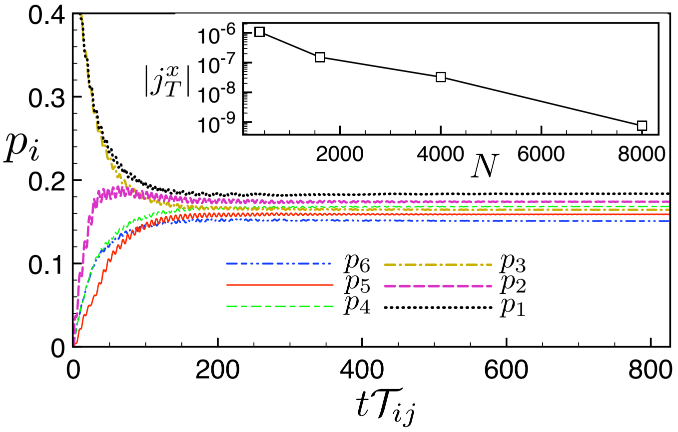

FIGURE 4.3: Relaxation dynamics of the occupation probabilities of the eigenstates of the unperturbed Hamiltonian (4.22). This results have been obtained by averaging over 4 000 realisations of the stochastic noise. The inset shows the vanishing energy current through the system when the number of runs of the stochastic process, *N*, increases. (Figure taken from [73])

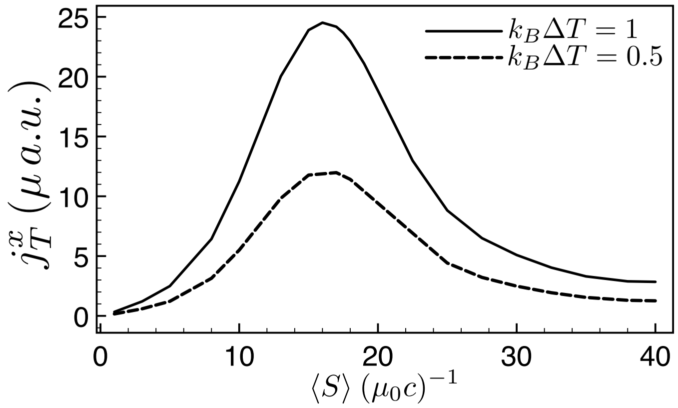

FIGURE 4.4: Dependence of the steady-state energy current on the coupling strength $\langle S\rangle$ for k_BT_E = 10 a.u. and N = 4 000. A turnover in the energy current can be observed. (Figure from [73])

To further verify the theory we find an expected turnover behaviour as seen in Fig. 4.4 [65, 69]. The turnover can be understood by considering that for small energy flux, when increasing the flux, more states are excited and can contribute to transport. On the other hand, at large fluxes, some of the states are fully occupied and are not able to contribute to transport anymore. At intermediate energy fluxes, a peak of the energy current must be achieved. In general, this behaviour cannot be described by perturbative theories for thermal transport such as the Redfield theory [69]. We have set the temperature gradient to ΔT = (T_L-T_R)/2.

In Fig. 4.5 the energy current is plotted versus the introduced thermal gradient, ΔT, from the blackbodies. A linear dependence on the thermal gradient can be found for $\Delta T \ll T$ (see inset). At large ΔT, a maximum in the energy current is reached. This implies that the system can sustain up to a maximum energy flow fixed the external conditions. Also, the position of the maximum of the energy current shifts to the right with increasing temperature of the environment. This might be relevant for technological applications since the maximum efficiency can be tuned according to the working conditions.

In conclusion, we have presented a novel theoretical framework to investigate thermal and energy transport, where the thermal imbalance in the system is introduced by the radiation from two classical blackbodies. Our theory also includes an environment, with which the system can exchange energy. Through the environment, the fundamental concept of thermal relaxation of the system is included, which is not the case in other thermal transport theories. The theory can also be used in different set-ups. For example, we can consider one blackbody only, to adapt to different experiments. Further discussions and conclusions can be found in chapter 7.

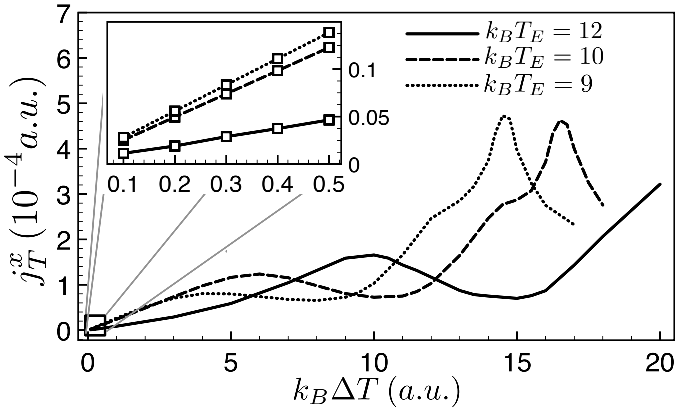

FIGURE 4.5: Energy current in the tight-binding system of Fig. 4.2 versus temperature gradient introduced by the blackbody radiation around the environmental temperature T_E. For this plot, we have used $\langle S \rangle = 15/\mu_0 c$ close to the maximum current of Fig. 4.4, and $N = 4\,000$. (Figure from [73])

Chapter 5

Influence of Decoherence on Thermo-Electric Transport

Non-equilibrium thermodynamics was developed to understand the flow of particles and energy between two heat reservoirs. The best-known example of this is Clausius' formulation of the second law of thermodynamics stating that heat cannot flow from a cold bath to a hot one. This is firmly based on the assumption that a macroscopic body in equilibrium is characterised by a single parameter, called its temperature. When two objects with different temperatures are in thermal contact, energy will flow from the hotter body to the body with lower temperature. For macroscopic bodies, the measurement of this process does not influence the flow of energy and particle between them. However, when moving from macroscopic systems down towards the length scale where the classical and quantum worlds meet, quantum effects has to be taken into account. In quantum physics, for instance an electron in an atom can be excited and not excited at the same time — it can be at two positions at a time. But when one measures it, only one of the two states is observed randomly and the coherent state is destroyed. This measurement can be though of an interaction with a classical system that destroys all quantum coherence. This raises the question of what might happen when the system interacts instead with a small quantum system, called a quantum observer. This quantum observation might break only locally quantum coherence continuously by a dynamical process known as decoherence [22]. Depending on how strong and where these quantum measurements are performed, novel quantum phenomena might arise. Decoherence has been shown to affect the efficiency of transport in molecular devices and biological systems [23]. In order to include decoherence into a thermodynamic formalism, the observer is modelled by a quantum decoherence bath. In contrast

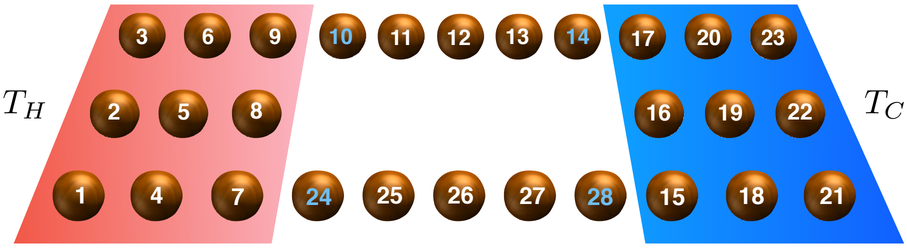

FIGURE 5.1: The considered thermo-electric transport device, where the nine leftmost and rightmost atoms are connected to thermal baths at temperature T_H and T_C, respectively. Due to this temperature imbalance, energy will flow from the hot to the cold side through the two branches. This device will be used to study interesting phenomena arising from a local quantum observations on the atomic sites indicated by the blue numbers.

to reservoirs in classical thermodynamics, this quantum bath has no temperature connected to it [74]. This observer acts as a new source of energy and entropy, which is not only able to change the flux of energy but also to influence the flows of particle as we will see.

5.1 Formalism

In this section we focus on the influence of a quantum observer on thermo-electric transport in two nano-scale transport devices and its thermodynamic implications. Unlike previous works [3], we consider an observer that is interested in knowing if a particle is or is not localised in only one specific region of a quantum transport device. This is inspired by the double-slit thought experiment. Therefore, we will consider a quantum transport device with two parallel branches for transport, as shown in Fig. 5.1. This device is coupled to two heat baths of different temperatures, T_H and T_C. Additionally, the device contains one particle in it, and the particle cannot escape via the baths. This mimics the situation where a device is heated and cooled by lasers on each side and the particle current is corralled inside the device. The quantum observer can look for the particle weakly at only one small segment of the devices, in this process, localising the quantum wave function. With this setup, we study steady-state heat and particle flow as a function of quantum decoherence on different parts of the device.

This device is modelled by the Hamiltonian

$$\hat{H} = \sum_i v_i \hat{c}_i^\dagger \hat{c}_i - \mathcal{T} \sum_{\langle i,j \rangle} \left(\hat{c}_i^\dagger \hat{c}_j + \hat{c}_j^\dagger \hat{c}_i \right), \tag{5.1}$$

where $c_i^\dagger$ creates an electron at the atomic site i. The hopping parameter $\mathcal{T}$ is uniform for the whole system and v_i is the on-site energy. To introduce a thermal imbalance ΔT in the transport device, we connect the nine leftmost and rightmost atoms to thermal baths kept at temperature T_H and T_C, respectively. These temperatures are chosen around an average temperature T_E as $T_{H,C} = T_E \pm \Delta T/2$. The applied temperature gradient will drive the system out of its equilibrium and energy will flow from the hot to the cold reservoir. In order to study this flow, we define the local energy-density operator

$$\hat{h}_i = -\frac{1}{2}\mathcal{T}\sum_{\langle j\rangle}\left(\hat{c}_i^\dagger\hat{c}_j + \hat{c}_j^\dagger\hat{c}_i\right) + v_i\hat{c}_i^\dagger\hat{c}_i. \tag{5.2}$$

The continuity equation

$$-\frac{d\hat{h}_i}{dt} = -i[\hat{H},\hat{h}_i] = \hat{j}_{i,i+1} - \hat{j}_{i-1,i} \tag{5.3}$$

is used to define the energy-current operator that describes the heat flow from site 12 to 13 [75],

$$\begin{aligned} \hat{j}^E_{\text{up}} &= \frac{i}{2}\left[v_i\hat{c}_{12}^\dagger\hat{c}_{12} - v_i\hat{c}_{13}^\dagger\hat{c}_{13}, -\mathcal{T}(\hat{c}_{12}^\dagger\hat{c}_{13} + \hat{c}_{13}^\dagger\hat{c}_{12})\right] \qquad (5.4)\\ &+ \frac{i\mathcal{T}^2}{2}\left(\left[\hat{c}_{12}^\dagger\hat{c}_{13} + \hat{c}_{13}^\dagger\hat{c}_{12}, \hat{c}_{13}^\dagger\hat{c}_{14} + \hat{c}_{14}^\dagger\hat{c}_{13}\right] + \left[\hat{c}_{11}^\dagger\hat{c}_{12} + \hat{c}_{12}^\dagger\hat{c}_{11}, \hat{c}_{12}^\dagger\hat{c}_{13} + \hat{c}_{13}^\dagger\hat{c}_{12}\right]\right). \end{aligned}$$

Analogously, the energy current of the lower branch, j^E_{down}, can be defined. Moreover, by considering the electronic density, the upper and lower particle current, j^p_{up} and j^p_{down}, are given in the standard way.

To model the coupling to the thermal baths (H and C) and to the quantum observer (D) we use an equation of motion for the state of the system, $\hat{\rho}$, similar to the NMME (2.17). As we are only interested in the steady-state transport regime, we will use a Markovian version of (2.17),

$$\begin{aligned} \partial_t\hat{\rho}(t) &= -i\big[\hat{H},\hat{\rho}(t)\big] + \sum_{a=H,C,D}\left(\hat{K}_a\hat{\rho}(t)\hat{S}_a + \hat{S}_a\hat{\rho}(t)\hat{K}_a^\dagger - \hat{S}_a\hat{K}_a\hat{\rho}(t) - \hat{\rho}(t)\hat{K}_a^\dagger\hat{S}_a\right)\\ &= -i\big[\hat{H},\hat{\rho}(t)\big] + \sum_{a=H,C,D}\hat{\mathcal{L}}_a[\hat{\rho}(t)]. \qquad (5.5) \end{aligned}$$

Here, $\hat{K}$ is defined for the hot and cold baths by

$$\hat{K}_{H,C} = \lambda^2\int_{-\infty}^{\infty}\mathrm{d}\tau\, C_{H,C}(\tau)e^{-i\hat{H}\tau}\,\hat{S}_{H,C}\,e^{i\hat{H}_S\tau}. \tag{5.6}$$

As before in this thesis, the thermal baths are modelled by assuming that the electronic system is in contact with the radiation inside a cavity. The corresponding coupling operator and bath-correlation function have been derived in section 2.3. In order to model the local coupling of the thermal baths to a specific region, either to the left (*H*) or the right side (*C*) of the system, we modify the coupling operator in Eq. (2.28) by

$$\hat{S}_{H,C} = -q\,\mathbf{u}\cdot\hat{\mathbf{r}}\,M_{H,C}(\hat{\mathbf{r}}). \tag{5.7}$$

Here, the introduced mask function $M_{H,C}(\hat{\mathbf{r}})$ is either one, for $\mathbf{r} \in (H, C)$, or otherwise zero. In addition, $\mathbf{u}$ is the polarisation direction of the modes in the cavity, which is parallel to the branches. In order to model the local observation at site *k* within the same formalism, we consider the quantum decoherence bath with[*]

$$\hat{K}_D = \frac{1}{2}\gamma_D^2 |k\rangle\langle k|, \tag{5.8}$$

where γ_D is the coupling strength and $|k\rangle$ is the wave function that describes a particle located at site *k*. In this way the local observer breaks quantum coherence only locally at site *k*.

---

[*] The coupling strength of the thermal bath, λ, and of the observer, γ_D, indicate how strong the thermal baths acts in comparison to the local observer. As the master-equation approach is perturbative, both should be small.

5.2 Results

Figure 5.2 shows the dependence of the steady-state particle and energy current on the decoherence strength γ_D and the applied temperature gradient ΔT. We have chosen v_i = 1 eV = 0.037 a.u., $\mathcal{T}$ = 0.5 eV, $k_B T_E$ = 0.008 a.u. and $\lambda = 0.2$. In plots (a) to (c) the local measurement is done at site 10, indicated by the eye. In Fig. 5.2 (c) the particle current in the upper branch is plotted versus the temperature gradient (*x*-axis) and the decoherence strength (*y*-axis). Without a local observation, γ_D = 0, no steady-state particle current is flowing in the upper branch. When a local observation is performed at site 10, a particle current starts to flow in the upper branch from the left to right side, indicated by a positive current in red. As this is a steady-state current and the particle is conserved inside the system, the corresponding current in the lower branch must be exactly the opposite of it. This means a particle ring-current is created which is flowing in clockwise direction as a result of the local measurement. This ring-current can be enlarged by increasing the decoherence strength. In Fig. 5.2 (b) the energy current is shown versus γ_D and the temperature gradient. While the curved upper surface corresponds to the energy current in the upper branch of the device, j^E_{up}, the flat contour-plot below corresponds to the energy current in the lower branch. Also here, a positive current (red) indicates a flow from left to right, while a negative heat current (blue) indicates that energy is flowing from right to left. Without observing the system, γ_D = 0, the energy currents in both branches are directed from the left to the right reservoir. In accordance with the second law of thermodynamics, heat flows from the hot to the cold region. By letting the quantum observer measure the system locally at site 10, this energy flow is increased in its natural direction.

Surprisingly, this situation changes strongly when the observation is instead performed at site 14, as shown in Fig. 5.2 (d)–(f). Here, the local measurement creates an electrical ring-current in counter-clockwise direction, as seen in Fig. 5.2 (f). That is, depending on where the observation is done, the direction of the electrical current can be controlled. This effect is a consequence of the localisation of the electronic wave function due to the quantum observation. Note that the electron density is around four times higher at sites in the leads compared to the sites in the branches. Therefore, when the quantum observer acts on site 14 as in Fig. 5.2 (d), the electron is pulled out of the right lead and provided with kinetic energy. An electronic current start to flow in the upper branch from the right lead to the left lead. However, when instead the measurement is done at site 10, close to the left lead, the observer takes out the electron from the left lead and the current flows in the opposite direction. An even more interesting effect happens if we

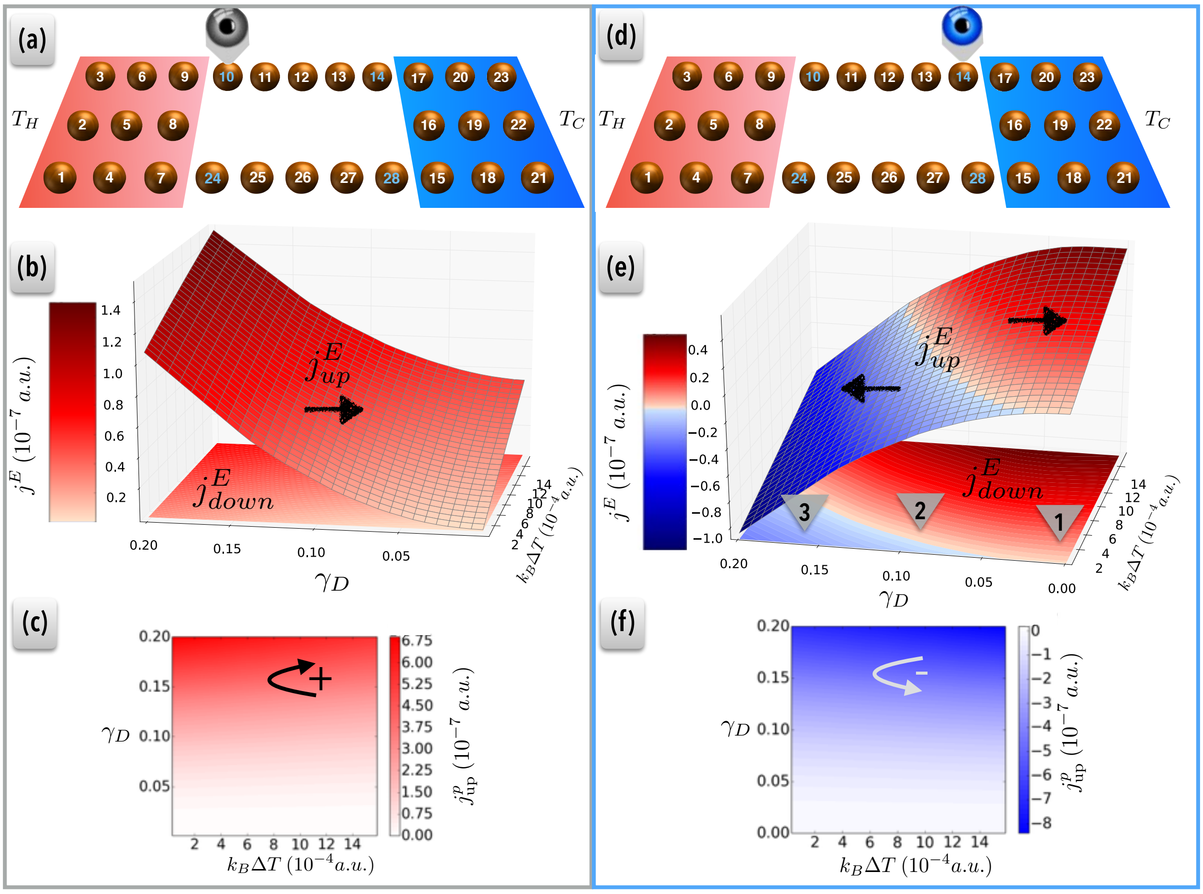

FIGURE 5.2: Particle and energy steady-state currents. While in (a)–(c) the observation is performed at site 10, in (d)–(f) the quantum observer acts on site 14. Plots (c) and (f) show the particle current in the upper branch as a function of the thermal imbalance and the decoherence strength. Plots (b) and (e) show the steady-state energy current in the upper branch (curved surface) and lower branch (flat surface below). Depending on where and how strong the measurement is done, the particle and energy currents can be modified separately.

look at the heat flows in the upper and lower branches of the device in Fig. 5.2 (e). When no observation is performed (triangle 1 in Fig. 5.2 (e)), heat flows from the hot to the cold reservoirs in both branches. By increasing the strength of the local observation at site 14, we are able to reverse both heat currents in the upper and lower branch (triangle 3). This leads to a situation where the energy flows from cold to hot, against the thermal gradient. Additionally, for intermediate γ_D (triangle 2) we are able to introduce also energy ring-currents in counter-clockwise direction. These results indicate that particle eddies can be created and controlled by the presence and location of the quantum decoherence. Note that a classical thermal bath is not able to introduce this particle ring-current, while the quantum observer is capable to influence not only the flows of energy but also the flow of particles.

Another promising applications of thermo-electric transport devices at the nanoscale are quantum ratchets that have been studied to control the transport of particles and heat [76–78]. A ratchet is a transport device that can produce directed flows induced by thermal or quantum fluctuations [79]. In order to model such a ratchet we introduce a spatial asymmetry in our transport device. Therefore, we change the on-site energy levels on the parallel tracks of the device as can be seen in Fig. 5.3 (a). In the upper branch (sites 10–14), the on-site energy increases per site per 10 % from the left to the right as can be seen on the diameter of the sites. In the lower branch instead, the on-site energies increase from the right to the left. Therefore, we create a quantum ratchet by adding two rectifiers on each branch facing in opposite direction. This could be experimentally realisable with techniques developed for constructing quantum ratchets in graphene [80], atom traps [81] or for molecular junctions [82]. We chose this type of anti-parallel ratchets configuration to break the top-down symmetry and therefore illustrate the differences of observing in the top or bottom branches. Figure 5.3 (c) shows that even without a quantum observer, an electrical current flows in clockwise direction. This is because the ratchet acts similar to the principle of a “salmon ladder”. For instance in the upper branch there is a small probability of the particle to hop from the left side each step up the ladder due to thermal fluctuations, but there is a very low probability for the particle on the right side to climb up the big drop of the ladder to then go down the ladder. Most interestingly, by adding quantum decoherence on site 14, at the top branch, the particle current changes direction, going against the natural direction of the ratchet, as can be seen in Fig. 5.3 (c). The energy currents, as illustrated in Fig. 5.3 (b), have similar regimes as before. As a function of decoherence, both upper and lower energy current can go with and against the thermal gradient. In Fig. 5.3 (b) also an intermediate regime can be seen, where the energy current flows as a ring current. As before, the situations changes when the observation is instead performed at site 28, in the bottom branch. The particle current in Fig. 5.3 (f) is always in the preferred direction of the ratchet, but this current can be significantly increased with stronger observation strength. Comparing the particle flow in (f) to that in (c) highlights how dramatic the flows can change depending on where the observer is acting. Figure 5.3 (e) shows how the energy current has regimes both with the thermal gradient and against, but also decoherence regimes where the energy flows in opposite directions in the top and bottom branches.

We demonstrated the influence of a quantum observer on the flow of energy and particles in two transport devices. Here, the position where the observer acts controls the flow of particles, leading to clockwise or counter-clockwise electrical currents inside the device. In addition, by

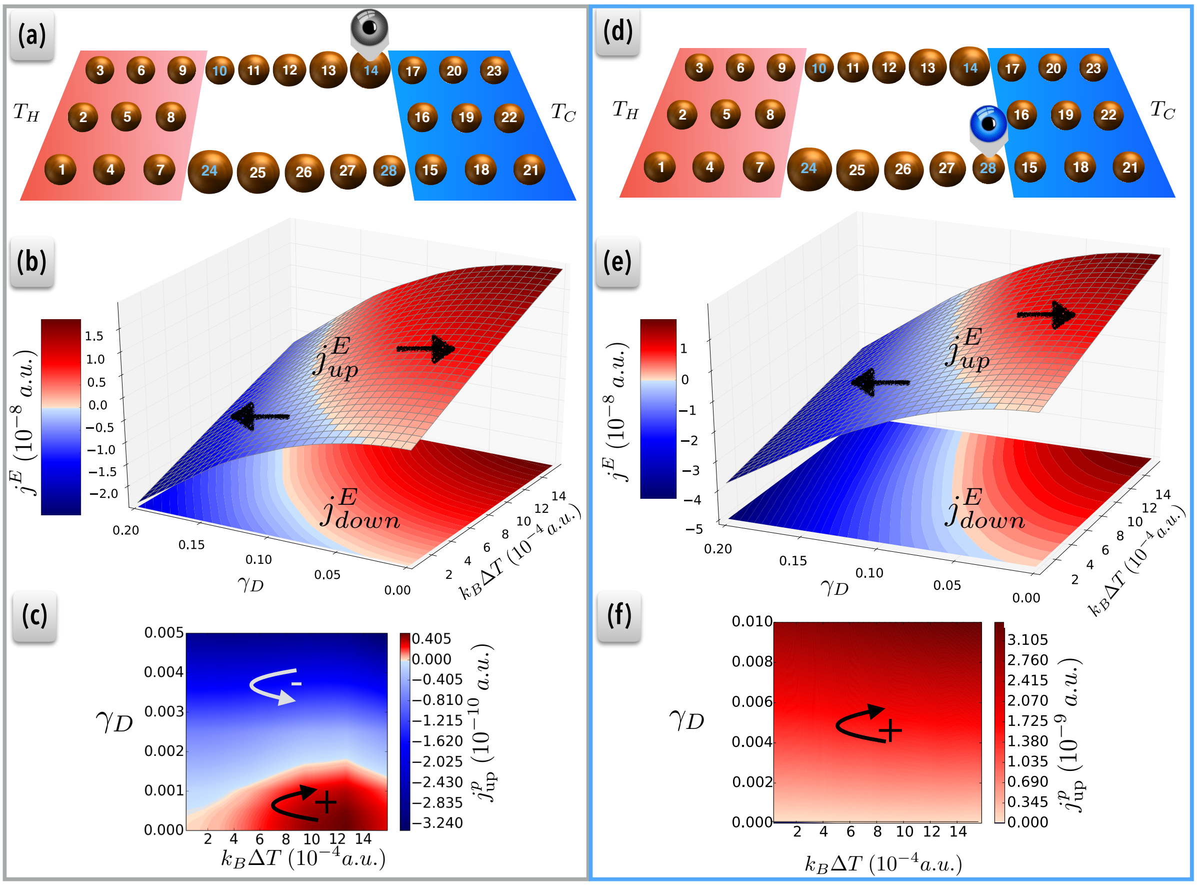

FIGURE 5.3: Particle and energy steady-state currents. Influence of a quantum observation on the thermo-electric flows in a quantum ratchet. In the subplots (a)–(c) the observation is performed at site 14, while in (d)–(f) the observer acts on site 28.

controlling the strength of decoherence in some configurations, we can change the direction of the energy flow even leading to a heat flowing from a cold reservoir to a hot one. It may appear that some of the previous results violate Clausius' formulation of the second law of thermodynamics. Obviously, this is not the case, and to clarify this we will examine the behaviour in terms of non-equilibrium thermodynamic concepts in the quantum regime. Therefore, we review the entropy production rate equation [83] in its more general form,

$$\dot{S} = \Phi + P. \tag{5.9}$$

Here, S is the total entropy of the system and Φ is the net entropy flow into the system. Furthermore, P is the entropy production rate due to irreversibility inside the system, and it is always non-negative. For a system at steady state between two temperatures, T_H and T_C, $\dot{S}$ is equal to zero and

$$\Phi = \Phi_H + \Phi_C = -\frac{\dot{Q}_H}{T_H} - \frac{\dot{Q}_C}{T_C}. \tag{5.10}$$

Here, $\dot{Q}_H$ and $\dot{Q}_C$ are the heat flows to the hot and cold reservoirs, respectively. This leads to

$$\frac{\dot{Q}_H}{T_H} + \frac{\dot{Q}_C}{T_C} = P \geq 0. \tag{5.11}$$

In the case that the only energy exchange happens via the two baths, the continuity equation, $\dot{Q}_H = -\dot{Q}_C$, leads to the familiar relationship of the second law of thermodynamics: heat goes from hot to cold bodies through the system. However, by adding quantum decoherence, it is possible to have heat flowing in more complicated ways, even against the thermal gradient. This is because decoherence can create a heat flow without a temperature associated with it. This changes the continuity equation to $\dot{Q}_H + \dot{Q}_C + \dot{Q}_D = 0$. However, the addition of this bath does not add a new entropy flow to Eq. (5.10). Instead, it does change the entropy production P by adding irreversibility to the system. To show this, we examine the entropy flow of the decoherence bath. For the coupling described by a master equation, the entropy flow into the system due to the local observer can be written as [74]

$$\Phi_D = -\mathrm{Tr}\left[\hat{\mathcal{L}}_D[\hat{\rho}]\hat{\sigma}_D\right]. \tag{5.12}$$

Here, $\hat{\sigma}_D$ is the stationary state of the decoherence bath that couples to site k, $\hat{\sigma}_D = |k\rangle\langle k|$, and $\hat{\mathcal{L}}_D$ is defined in Eq. (5.5) and given by

$$\hat{\mathcal{L}}_D[\hat{\rho}] = \gamma_D^2\left(\langle k|\hat{\rho}|k\rangle|k\rangle\langle k| - \frac{1}{2}|k\rangle\langle k|\hat{\rho} - \frac{1}{2}\hat{\rho}|k\rangle\langle k|\right). \tag{5.13}$$

Inserting the former equation into Eq. (5.12) gives $\Phi_D = 0$. This means that a decoherence bath changes the energy flow in the system, without having an entropy flow connected with it. Thus, a local observation can directly change the entropy production inside the system, P. This allow us to add disorder to the system by purpose and we have seen that this leads to new types of dynamical states, such as particle ring-currents in our quantum device. This reminds on the early works of Prigogine [83]: “Irreversible processes may lead to a new type of dynamic states of matter called ‘dissipative structures’ ”. These dissipative structures have been used to explain non-equilibrium systems such as living organisms or hurricanes [84]. The role of having an observer looking can be used to change the thermodynamics of a system. However, this can be exploited even further in the quantum regime by breaking coherence at only some parts of the system: Irreversibility is added only to certain regions of the system. This changes the dynamics of the system by modifying the flows of particle and energy such that it gives rise to new regimes analogous to dissipative structures, except that here it comes from a purely quantum source. Our quantum-observer effect might be a good example of the fact that disorder may be a source of order and the first occurrence of dissipative structures at the quantum level.

To summarise, we demonstrated how a quantum measurement can change the direction and magnitude of heat flows, even having it going against the temperature gradient, depending on where and how strong these observations are. We also show how, under these observations, particle ring-currents can be created and controlled. Therefore, the choice of location of these quantum measurements can provides full control of the direction of the energy flow and of the particle currents separately. Even though this seems baffling from a thermodynamic point of view, by treating quantum measurements as a thermodynamic bath we clarify this. Creating and controlling particle ring-current could lead to novel ways to generate and control magnetic fields [85]. Additionally, studying the role of decoherence may lead to advances in novel thermoelectric devices operating at the quantum scale. This study also highlights the role of observers in quantum systems. From a fundamental point of view, it illustrates how Schrödinger's cat paradox has important implications for thermodynamics as well as for transport at the nanoscale.

Chapter 6

Optical and Electronic Properties of Layered 2D Materials

In the previous chapters, we have studied the interaction of model fermionic or bosonic systems with radiation, where the quantum nature of the latter has been important. There, we have treated the radiation within different approaches, ranging from the classical treatment via minimal coupling over deterministic quantum methods within master equations, to quantum stochastic methods within the stochastic Schrödinger equation. In this last chapter of the thesis we will consider instead the interaction of real materials with light. While we will treat the radiation classically, which is a good approximation for the coupling of fields of high intensity to macroscopic systems, we will improve on the description of the electronic system by modelling it from first principles via DFT and the *GW* approximation. The theoretical investigation of the interaction of real materials with light will give us insights into optical absorption behaviour, electronic properties and excitonic effects and allow us to compare with modern experiments.

I will introduce in section 6.1 the full electronic many-body problem, for which a complete description may be obtained by solving the Schrödinger equation directly. Due to the large number of degrees of freedom, the N-particle wave function is much too large to be stored numerically. Moreover, it contains much more information than necessary for calculating relevant physical properties. DFT provides an alternative description of many-body systems in terms of the electronic density, circumventing the computational costly task of finding the electronic many-body wave function via the solution of the Schrödinger equation. This theory is in principle exact, yielding the same physical observables as the standard quantum-mechanical approach at the price of having to approximate an unknown but universal exchange–correlation density-functional. As the thesis is not mainly about the fundamentals of DFT, but it is used in this last chapter, I will explain only briefly the underlying concepts and refer to further literature about the details of DFT and many-body perturbation theory.

As an extremely interesting system to study the interaction of real materials with light, layered 2D materials have been chosen. The reason for choosing those materials is twofold: One the one hand, 2D materials have established their place as candidates for the next generation optoelectronic devices. They present outstanding mechanical and electrical properties and can be easily integrated with conventional silicon technologies. Comparing them to the their higher (3D) and lower (1D) dimensional counterparts, those materials offer high electric field tunability. In addition, layered materials often bring new functionalities and applications beyond those of industry standard transistors and photodetectors such as stronger light–matter interaction [25, 26], flexibility and transparency [27, 28], and the opportunity to combine layered materials into van der Waals heterostructures [86, 87]. A family of these materials are the **transition metal dichalcogenides (TMDCs)**, as for instance, MoS_2, $MoSe_2$, WS_2, and WSe_2. TMDCs have shown semiconducting properties, like a direct gap and tunability, superior to certain extent to those of graphene and could form a basis for novel transistors and photodetectors. Ideally, these materials should have a gap comparable with that of Silicon to ease the integration on the existing technology. However, TMDCs show a direct bandgap only when reduced to the single layer form due to interlayer interaction, which might limit their systematic use. The broad family of layered materials is only so far barely explored and there still exist many members that remain to be investigated [88]. The group IV trichalcogenides, for instance, are interesting when compared with the well-studies TMDCs because in particular titanium trisulphide, TiS_3, present a direct gap of 1 eV in bulk and few layered samples [89]. Additionally, TiS_3 shows an extremely fast optical response: an ideal property for the next generation of photodetectors [90–92]. Moreover, trichalcogenides have reduced in-plane bonding symmetry which again differentiates them from the more well-known TMDCs and it has been predicted that TiS_3 could be a promising electrode material for Li and Na in batteries [93], as photoelectrode for H_2 photogeneration [94], and nano-electronics and optics [95], presenting also strong anisotropic behaviour and non-linearity both in the electronic and optical properties [91, 92, 96, 97].

Therefore, we will study the optical and electronic properties of TiS_3 in section 6.2 to 6.5. In section 6.2 we will demonstrate (experimentally) and investigate theoretically the control over the morphology of TiS_3 by changing the temperature during the growing process. At a growth temperature of 400 °C the material displays a 2D morphology of flower-like nanosheets whereas at higher growth temperature (500 °C) TiS_3 shows belt-like nanoribbon structure. Most interestingly, the nanoribbons and nanosheets also display different electronic and optical properties.

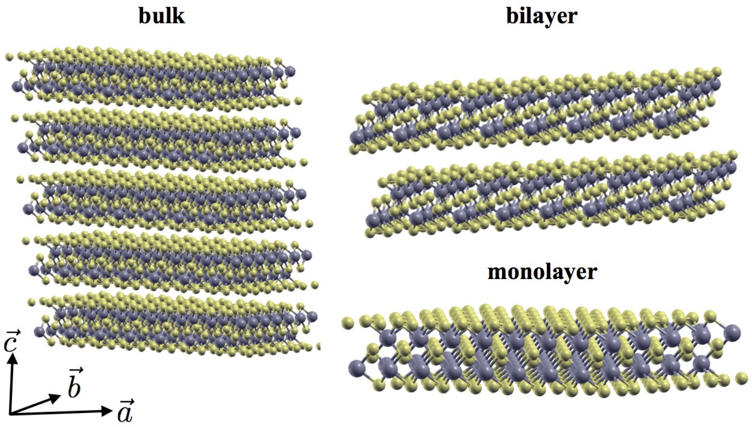

FIGURE 6.1: The three different atomic structures under investigation. Bulk TiS_3 is a layered material where the different layers are essentially weakly interacting. The unit-cell vectors for the bulk are shown in the left figure. For monolayer and bilayer structures the $\mathbf{a}$ and $\mathbf{b}$ vectors are essentially the same.

In addition, we will investigate in section 6.3 with a combination of *ab initio* and experimental methods, the effect of compressive and tensile strain on few layered TiS_3. We found that it is extremely sensitive to external conditions and this can become of extreme interest for tailoring both the electronic and optical properties of TiS_3 based devices. Those results can be of highest significance to the community of two-dimensional materials, fast photodetectors as well as battery technology.

After the investigation of the electronic properties of TiS_3, we will present in section 6.4 and 6.5 a combined study of the electronic and optical bandgap of layered TiS_3. While in section 6.4 we study the in-plane anisotropy of the electrical and optical properties of few-layer TiS_3 flakes, in section 6.5 we concentrate on the excitonic effects to determine its exciton binding energy. Therefore, we combine scanning tunnelling spectroscopy and photo-electrochemical measurements with *GW* and BSE calculations. We find in good agreement between theory and experiment a binding energy of the order of 100 meV, which is orders of magnitude larger than that of common semiconductors and comparable to bulk TMDCs, making TiS_3 a highly interesting material for optoelectronic application and for studying excitonic phenomena even at room temperature.

Last but not least, in section 6.6 we study another member of the 2D materials, namely, In_2Se_3. This material is a very interesting direct gap semiconductor with promising application in ultraviolet photodetection. We report an observed variation of the optical bandgap due to quantum confinement, which is among the largest reported to date in 2D semiconductors materials, comparable to this of atomically thin black phosphorus.

While the experiments have been done by our collaborators, all calculations and theoretical investigation have been performed by me under the supervision of Roberto D'Agosta. The plane-wave code Yambo [98] is used to calculate quasiparticle corrections and optical properties, while the electronic structure calculations and structure optimisations have been performed by the DFT pseudopotential plane-wave method as implemented in the PWSCF code of the Quantum-Espresso package [99]. All the configurations are ionically relaxed using the Broyden–Fletcher–Goldfarb–Shanno's procedure available within the Quantum-Espresso package.

6.1 Density Functional Theory and Beyond

Let us consider a system of N electrons subjected to an external potential $v_{\text{ext}}(\mathbf{r})$ described by the Hamiltonian

$$\hat{H}(\mathbf{r}_1, \mathbf{r}_2, ..., \mathbf{r}_N) = \sum_{j}^{N} \left(-\frac{1}{2}\hat{\boldsymbol{\nabla}}^2_{\mathbf{r}_j} + v_{\text{ext}}(\mathbf{r}_j) \right) + \frac{1}{2}\sum_{j \neq k}^{N} \frac{1}{|\mathbf{r}_j - \mathbf{r}_k|} \,. \tag{6.1}$$

Here, the external potential includes the attraction between electrons and the fixed nuclei and any external electric fields. The last term of Eq. (6.1) describes the electron–electron interaction, V. The solution of the time-independent Schrödinger equation gives the energy eigenvalues E_i and the eigenstates of the system

$$\hat{H}|\Psi_i\rangle = E_i|\Psi_i\rangle, \tag{6.2}$$

where the state corresponding to the lowest energy eigenvalue E_0 is called the ground state. Unfortunately, this many-body wave function depends on all $3N$ coordinates. The storage and handling of such a function, even for relatively small systems, is intractable. As an example, let us think of a system of seven electrons (a simple nitrogen atom) with its 21 coordinates. If we discretise the space in ten entries per direction, its wave function has 10^{21} entries. If we further assume that it takes one byte per entry, we would need around 2×10^{11} DVDs to store the ground-state wave function. This imaginary collection of DVD's would weight around a million tons. Hence, to study successfully the properties of our electronic system one would like to calculate the expectation values of the relevant operators indirectly, i.e., without calculating the wave functions itself. The Hohenberg–Kohn theorem states that the ground-state electronic density,

$$n_0(\mathbf{r}) = \int |\Psi_0(\mathbf{r},\mathbf{r}_2,...,\mathbf{r}_N)|^2 \mathrm{d}r_2^3...\mathrm{d}r_N^3, \tag{6.3}$$

alone already determines the external potential and hence the many-body Hamiltonian and all ground-state properties uniquely [100]. In principle every observable can be calculated from n_0 of a system alone. DFT is based on the Hohenberg–Kohn theorem, and it is based on the knowledge of the density $n_0(\mathbf{r})$ instead of the full many-body wave function of the N-particle system. The Hohenberg–Kohn theorem is an existence and uniqueness theorem: it proves that the ground state of the system can be obtained from its density alone, however, it does not tell us how to do so in practice. To overcome this impasse, Kohn and Sham [101] proposed the use of an auxiliary non-interacting system instead, the **Kohn–Sham** (**KS**) system, with the same density as the interacting system. The essence of the KS scheme is that the ground-state density of the interacting system of interest can be calculated as the ground-state density of the auxiliary KS system of non-interacting particles which are moving in a local effective potential by solving self-consistently the set of KS equations [101],

$$\begin{aligned}
\hat{h}_{\mathrm{KS}}|\phi_i\rangle &= \epsilon_i|\phi_i\rangle, && (6.4)\\
\hat{h}_{\mathrm{KS}} &= -\frac{1}{2}\hat{\boldsymbol{\nabla}}^2 + v_{\mathrm{ext}}(\mathbf{r}) + \frac{1}{2}\int \mathrm{d}r'^3 \frac{n(\mathbf{r}')}{|\mathbf{r}-\mathbf{r}'|} + v_{\mathrm{xc}}[n](\mathbf{r}), && (6.5)\\
n(\mathbf{r}) &= \sum_{j=1}^{N} |\phi_j(\mathbf{r})|^2, && (6.6)\\
\int \mathrm{d}r^3 n(\mathbf{r}) &= N. && (6.7)
\end{aligned}$$

Here, the KS wave functions ϕ_i and eigenvalues ϵ_i do not, in general, have a direct physical meaning. However, these wave functions can be used to construct the true density of the interacting system according to Eq. (6.6). The difficulty of the original problem is transferred into the unknown exchange and correlation potential, $v_{\mathrm{xc}}[n](\mathbf{r})$. In principle the solution of the KS equations with the exact exchange–correlation potential, would yield single-particle eigenstates whose electronic density is the same as that of the interacting system. The exact xc-potential, including all non-trivial many-body effects, is unknown and has to be approximated. The KS scheme provides very good results for the ground-state energies and densities for a large variety of systems. However, the eigenvalues obtained from the solution of the KS equations, except for the highest occupied (which equals the negative of the vertical ionisation energy of the system [102, 103]), do not have any physical meaning. When KS eigenvalues are used to calculate, for example, the electronic bandgap of semiconductors the results may have significant errors. Usually, bandgaps are underestimated by DFT and the quality of the band structure depends strongly on the studied material. In order to obtain accurate bandgaps we have to go beyond the KS scheme and employ a **quasiparticle** (**QP**) description. The QP energies are those needed to add or remove an electron from the system. These energies are experimentally accessible via direct and inverse photo-emission experiments.[*] We will briefly describe the QP concept within **Many-Body Perturbation Theory** (**MBPT**) by discussing the Green's-function formalism, the self-energy concept and the GW approximation. We suggest to the reader Refs. [104] and [105] for a deeper discussion on many-particle physics. Furthermore, we will consider briefly how to include the electron–hole binding by going beyond the GW approximation.

While DFT is an effective one-particle scheme and in principle capable to predict ground-state properties correctly, it often fails to accurately predict properties of the excited system or the absorption of light. In order to go beyond DFT for the calculation of electronic excitations, the GW approximation is nowadays widely used. In the GW method, the key ingredients are the screened Coulomb interaction W and the one-particle Green's functions G. The latter contains more information than a simple density, but much less than the many-body wave function. Besides the physical quantities already accessible through the density, one-particle Green's functions make accessible the single-particle excitation spectrum, that is, the band structure. Moreover, in order to calculate optical absorption spectra of insulators and semiconductors, one needs to include the binding between the excited electron (in the conduction band) and the hole that it leaves behind in the valence band. The electron and the hole can interact so strongly that they will form a bound state, called an exciton. To describe these excitonic effects, one

---

[*] As an interesting side note that does not get mentioned often enough in this context: Bandgaps are not the result of a single experiment but of two separate quite different measurements (direct and inverse photo-emission spectroscopy). As such, one could argue that the bandgap is not even an observable, and the often proclaimed "failure" of DFT is a moot point. DFT is not designed at all to give electronic bandgaps, not even bandstructures.

should resort to a two-particle formalism by solving the **Bethe–Salpeter Equation** (**BSE**) for the two-particle correlation function.

In the following, we will describe the basic concepts of MBPT, by introducing the one-particle Green's function and the self-energy Σ, which is a non-hermitian operator containing all the correlation and exchange effects of the many-body system. The Green's function gives access to the QP excitation energies and band structure. In order to calculate the Green's function one can solve for instance Hedin's equations. A widely used approximation to solve these equations is the *GW* approximation. In this thesis, I will not describe in detail the theory of two-particle Green's functions or the BSE, but I will state the fundamental assumptions in order that the reader is able to follow its application later in this chapter. A more detailed discussion of the basic physical ideas reviewed in this section can be found in MBPT textbooks [104, 106] and the reviews of Strinati [107] or Onida [108].

In contrast to the non-interacting KS system of DFT, in MBPT a particle interacts with and perturbs the particles in its surroundings. In the MBPT picture, the QP can be thought of as a particle moving through the system, enclosed by a cloud of other particles that are being pushed away or dragged along by its motion. This whole entity moves through the system like a weakly interacting particle [109], called a QP. The interacting-particle problem can be described via weakly interacting QPs, described by a screened potential W rather than by the bare coulomb potential, V. This allows us to perform a perturbative expansion with respect to the weak QP interaction. The one-particle Green's function expresses the probability for the propagation of a QP from position $\mathbf{r}_2$ at time t_2 to $\mathbf{r}_1$ at time t_1 (for $t_1 > t_2$) and is defined (at zero temperature)

$$G(1,2) = -i\langle N|\hat{T}[\Psi_H(1)\Psi_H^{\dagger}(2)]|N\rangle, \tag{6.8}$$

where $1 = \{\mathbf{r}_1, t_1\}$. Here, $|N\rangle$ is the ground-state vector of the N-particle interacting system, Ψ_H is the annihilation field operator in the Heisenberg picture,

$$\Psi_H(\mathbf{r},t) = e^{i\hat{H}t}\Psi(\mathbf{r})e^{-i\hat{H}t}, \tag{6.9}$$

and $\hat{T}$ is the time-ordering operator. One can define an equation of motion for the one-particle Green's function by using the functional derivate technique [107, 110]. This equation of motion depends on the two-particle Green's function that describes the correlated propagation of two QPs. Consequently, in order to solve the equation of motion one has to deal with a hierarchy of equations for Green's functions of all orders. However, it is possible to formally close this hierarchy by introducing the self-energy Σ through the Dyson equation,

$$G(1,2) = G_0(1,2) + \int \mathrm{d}(3,4) G_0(1,3)\Sigma(3,4)G(4,2), \tag{6.10}$$

where G_0 is the Hartree Green's function, solution of the Hartree system (defined by $\hat{h}_0 = -\frac{1}{2}\hat{\boldsymbol{\nabla}}_r^2 + v_{\text{ext}}(\mathbf{r},t) + V_H(\mathbf{r})$),

$$[\omega - \hat{h}_0(\mathbf{r}_1)]G_0(\mathbf{r}_1,\mathbf{r}_2,\omega) = \delta(\mathbf{r}_1 - \mathbf{r}_2), \tag{6.11}$$

with V_H as the Hartree potential. In the Dyson equation (6.10) the correlation and exchange contributions are accounted for via an operator that is in principle unknown, the self-energy Σ. The Green's function can be expressed in the basis of energy-dependent wave functions, $\phi_i(\mathbf{r},\omega)$, which form an orthonormal and complete basis set for each ω

$$G(\mathbf{r}_1,\mathbf{r}_2,\omega) = \sum_i \frac{\phi_i(\mathbf{r}_1,\omega)\phi_i^*(\mathbf{r}_2,\omega)}{\omega - E_i(\omega)}, \tag{6.12}$$

where the wave functions and the energies E_i are solutions of the equation

$$\hat{h}_0(\mathbf{r})\phi_i(\mathbf{r},\omega) + \int \mathrm{d}r'^3 \Sigma(\mathbf{r},\mathbf{r}',\omega)\phi_i(\mathbf{r}',\omega) = E_i(\omega)\phi_i(\mathbf{r},\omega). \tag{6.13}$$

As Σ is a non-hermitian operator the energies E_i are in general complex and the imaginary part gives the lifetime of the excitation. If the energy spectrum presents sharp peaks, $E_i(\omega) \approx E_i^{\text{QP}}$, we arrive at the QP equations

$$\hat{h}_0(\mathbf{r})\phi_i^{\text{QP}}(\mathbf{r}) + \int \mathrm{d}r'^3 \Sigma(\mathbf{r},\mathbf{r}',E_i^{\text{QP}})\phi_i^{\text{QP}}(\mathbf{r}') = E_i^{\text{QP}}\phi_i^{\text{QP}}(\mathbf{r}). \tag{6.14}$$

Solving these equations provides the QP energies and band structure. However, the self-energy is unknown and the MBPT gives us a practical scheme to solve such a task. This scheme, also called Hedin's equations, consists of five coupled integral equations for the self-energy Σ, the screened interaction W, the polarisability P, the vertex function Γ, and the Green's function

[111],

$$\begin{aligned}
\Sigma(1,2) &= i\int \mathrm{d}(3,4)G(1,4)W(1,3)\Gamma(4,2,3), &(6.15)\\
G(1,2) &= G_0(1,2)+\int \mathrm{d}(3,4)G_0(1,3)\Sigma(3,4)G(4,2), &(6.16)\\
\Gamma(1,2,3) &= \delta(1,2)\delta(1,3)+\int \mathrm{d}(4,5,6,7)\frac{\delta\Sigma(1,2)}{\delta G(4,5)}G(4,6)G(7,5)\Gamma(6,7,3), &(6.17)\\
P(1,2) &= -i\int \mathrm{d}(3,4)G(1,3)G(4,1)\Gamma(3,4,2), &(6.18)\\
W(1,2) &= V(1,2)+\int \mathrm{d}(3,4)W(1,3)P(3,4)V(4,2), &(6.19)
\end{aligned}$$

which have to be solved self-consistently. Here, the polarisation P represents the variation of the induced density with respect to a variation of the external plus Hartree potential,

$$P(1,2) = \frac{\delta n(1)}{\delta\big(v_{ext}(2)+V_H(2)\big)}, \tag{6.20}$$

and is related to the dielectric function by

$$\epsilon(1,2) = \delta(1,2) - \int \mathrm{d}(3)V(1,3)P(3,2). \tag{6.21}$$

Furthermore, the dielectric function is linked to the screened Coulomb potential via $W = \epsilon^{-1}V$. One strategy to solve Eqs. (6.15)–(6.19) would be to start with $\Sigma = 0$ and calculate in the order, first the Green's function G (at this step G_0), then the vertex function (only a δ-function), the independent particle polarisability P_0) (also called Random Phase Approximation polarisability), the screening W_0) and the self-energy $\Sigma = iG_0\mathrm{W}_0$, which is now updated. This procedure can be repeated and solved self-consistently, keeping the vertex function proportional to the δ-function. However, in practice one typically stops after one iteration. This approximation is called the non-self-consistent G_0W_0 approximation [112], or simply G_0W_0. In the GW approach the existence of polarisation effects that screen the propagation of an extra particle is explicitly taken into account, so that GW is a dynamically screened approximation. Note, when performing G_0W_0 calculations, also called single-shot GW, the resulting QP corrections to the band structure are starting point dependent. For this reason, the choice of the mean-field results, in general the KS eigenvalues and eigenfunctions employed to calculate G and W, is quite important. Clearly, this procedure is justified when the starting wave functions are already close to the QP ones. This is indeed the case in many systems, and therefore G_0W_0 has been extremely successful in describing electron addition and removal energies for metals, semiconductors and insulators [113–115], and is one of the methods of choice for the description of direct and inverse photoemission experiments [116–118].

The *GW* approximation has led to important improvements in the description of band-gap energies and single-particle excitations effects. However, *GW* may fail to describe neutral excitation spectra, such as absorption spectra, for systems with significant electron–hole binding. This is because the *GW* method, both single-shot and self-consistent, describes excitations that change the number of particle of the system, by adding or removing an electron. However, reflectivity, absorption and fluorescence spectroscopies involve neutral excitations, where the total number of electrons in the system is constant. Such processes are two-particle excitations. For a proper description of such excitations it is necessary to include the vertex function Γ in Eq. (6.18). This inclusion via Hedin's equation (6.17) is crucial for the accurate description of two-particle excitations. This is the aim, and the success, of the BSE [119] by taking a second iteration in Hedin's equation. For a general review we refer to references [107] and [120]. The solution of the BSE yields very accurate results in the calculation of optical properties of solids with continuum and bound excitons, in bulk and nano-structured systems (see reference [120] and references therein).

6.2 TiS_3 Transistors from Nanoribbons or Nanosheets*

In our article [91], we demonstrate the control over morphology of TiS_3 to obtain nanosheets with large surface area which facilitates the exfoliation of TiS_3 down to a single layer. Films of TiS_3 can be obtained by the reaction of titanium with sulphur [121]. In the presence of sulphur excess (more than 75 at% of sulphur) and at a temperature below 632 °C, TiS_3 starts to grow [122]. As seen in Fig. 6.2, the form of the obtained TiS_3 depends strongly on the temperature during the growing process. In this figure, **scanning electron microscopy (SEM)** images of separate TiS_3 samples grown at 400 °C (Fig. 6.2 (a)), 450 °C (Fig. 6.2 (b)) and 500 °C (Fig. 6.2 (c)) are shown.

---

*This section is a part of the article
"TiS_3 transistors with tailored morphology and electrical properties", Advanced Materials **27**, 2595–2601 (2015), by J. O. Island, M. Barawi, R. Biele, A. Almazán , J. M. Clamagirand, J. R. Ares, C. Sánchez, G. A. Steele, H. S. J. van der Zant, J.V. Alvarez, R. D'Agosta, I. J. Ferrer, and A. Castellanos-Gomez
Here, we discuss only part of the work relevant for the thesis. Further experimental details can be found in the article and the supporting material.

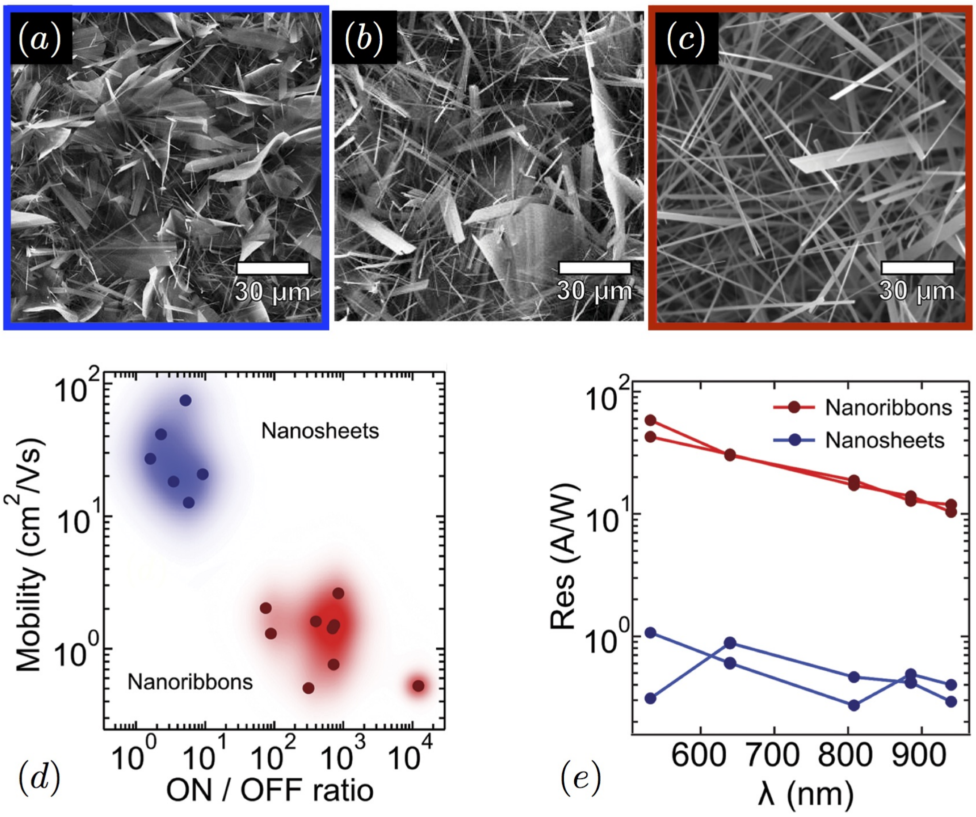

FIGURE 6.2: SEM images of the TiS_3 film grown at (a) 400 °C (nanosheets), (b) 450 °C, and (c) 500 °C (ribbons). (d) Mobility versus ON/OFF ratio for nanoribbons and sheets. (e) Responsivity versus wavelength for two representative devices for both nanoribbons and nanosheets using a 500 μW laser excitation. (Figure reused from our article [91])

These plots indicate that at a growth temperature of 400 °C the material displays a 2D morphology of flower-like nanosheets whereas at higher growth temperature (500 °C) TiS_3 grows as belt-like nanoribbons. The electronic properties of the two morphologies (1D nanoribbons and 2D sheets) are compared by fabricating **field-effect transistors (FETs)** of the same approximate thickness but different morphology. Measurements at room temperature are then made in a vacuum probe station. In order to compare the electrical properties between the ribbons and sheets, measurements are made along the same axis. The b-axis, which correspond to the high mobility axis, has been determined in order to measure the transfer curves of the FET devices. From this, the FET mobility has been extracted through,

$$\mu = \frac{L}{WC_iV_b}\frac{\partial I}{\partial V_g}, \tag{6.22}$$

where L is the channel length, W the channel width, C_i is the capacitance to the gate electron, and V_b is the voltage bias. On the one hand, for the nanosheet FET a resistivity at zero back-gate voltage of 0.09 Ω, mobility of 73 $cm^2\,V^{-1}\,s^{-1}$ and a ON/OFF current ratio of five has been measured. While on the other hand, for the ribbon device a resistivity of 56 Ω, which is two orders of magnitude larger than the sheet device and a mobility of 0.5 $cm^2\,V^{-1}\,s^{-1}$, have been found. Furthermore, the ON/OFF ratio for the nanoribbon FET is around 300 (at a bias voltage of 1 V). Exploring further the difference in the electronic properties, we plot the mobility versus the ON/OFF ratio in Fig. 6.2 (d) for all measured ribbon and sheet devices. This scatterplot demonstrates a clear difference between the ribbons (grown at 500 °C) and the sheets (grown at 400 °C). While the sheets have a more doped semiconductor behaviour (high mobility and low ON/OFF current ratio), the nanoribbons have a more semiconducting behaviour (low mobility and a high ON/OFF ratio). Furthermore, the photoresponse is measured. In Fig. 6.2 (e), we plot the responsivity versus the excitation wavelength for a representative ribbon and sheet FET device. Here, the responsivity $R = I_{\text{ph}}/P$ is measured with the same biasing conditions for each device (V_b = 100 mV, V_g = 40 V). Here, I_{ph} is the photocurrent and P is the power of the laser. The nanoribbon device has a responsivity which is two order of magnitude larger than the sheet device. A plausible explanation of the low ON/OFF current ratio, high mobility and reduced photoresponse of the nanosheet grown at 400 °C might be the presence of sulphur vacancies which have been shown to induce a strong n-type doping in dichalcogenides [123–126].

In order to understand and clarify those findings, we performed first-principle investigations of the electronic structure of TiS_3. The electronic band structure for the clean TiS_3 and the system

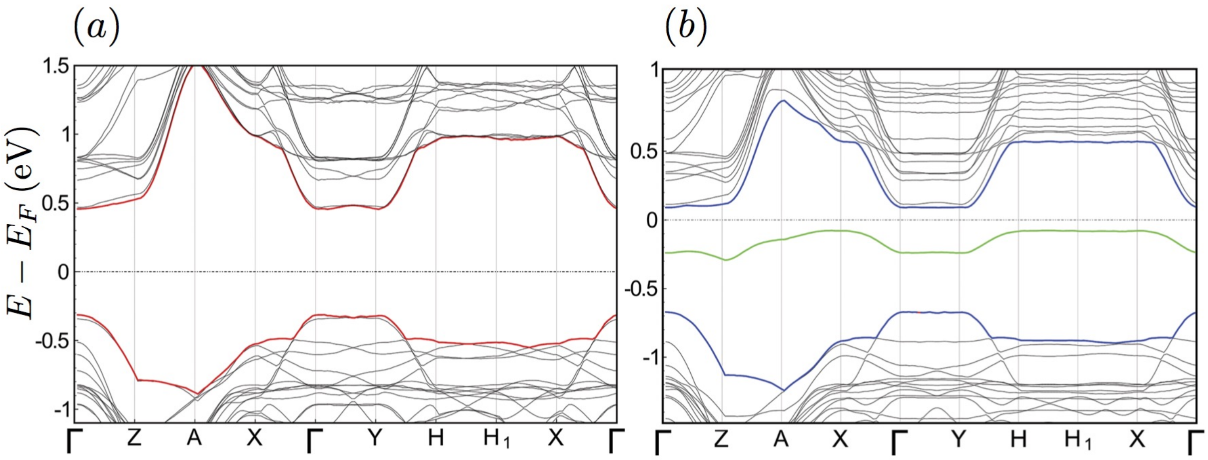

FIGURE 6.3: (a) Electronic band structure for the clean TiS_3. (b) Electronic band structure for the doped TiS_3 with sulphur vacancies. It is seen that the presence of the vacancy creates a localised electronic state below the Fermi energy (green), therefore the S vacancy acts as n-dopant. (Figure reused from [91])

with a fairly large density of S vacancies (2%) are reported in Fig. 6.3. Comparing Fig. 6.3 (a) and (b), it is seen that the presence of the vacancy creates a localised electronic state below the Fermi energy, therefore the S vacancy acts as n-dopant. Indeed, this state in fully occupied, and it increases the free carrier (electron) density. On the other hand, the vacancies do not affect the direct gap at the Γ-point that remains about 0.8 eV, as the localised vacancy state has a fairly small density of states. Therefore, it is unlikely detected during the measurement of the optical gap. Indeed, the bandgap from UV-vis measurements is the same in the two samples. In addition, the calculated energy difference between the ground state energy for the clean and doped TiS_3 is about 300 meV which indicates that the vacancy will most likely be filled in a S rich atmosphere at large temperature. Indeed, in a S rich atmosphere, a vacancy will reach the surface and rapidly recombine with a S atom from the atmosphere. This could explain why the nanosheets grown at 400 °C are more rich in vacancies and therefore act as a strongly doped semiconductor. Nonetheless, we can see in Fig. 6.3 (b) that the vacancy state (green line) is not fully localised, although, the effective mass of the electrons in this state is fairly large. This finite dispersion is probably an artefact of the large density of vacancies we can investigate within our numerical approach. We have considered in our analysis all the three possible configurations with a vacancy (due to symmetry the other three are equivalent to those). We have found that only one configuration is electronically active, the other two are higher in energy with respect both to the clean system which provides the ground state configuration and to the vacancy that is electronically more active, and do not significantly affect the electronic properties of TiS_3.

As the experiments have been performed by the Mire group in Madrid, experimental details can be found in the corresponding article and its supporting information. However, we have calculated the electronic properties of bulk TiS_3. By starting from the lattice parameters provided experimentally [91], we have built a $2\times2\times2$ supercell to reduce the vacancy density as much as possible. We have therefore optimised the atomic positions with a residual force after relaxation of 0.001 a.u., for both the pristine system and with a vacancy. The exchange–correlation potential is described self-consistently within the generalised gradient approximation throughout the Perdew–Burke–Ernzerhof's functional, and the Trouiller–Martins' norm-conserving pseudopotential both for Ti and S is used to model valence electron–nuclei interactions. The energy cut-off for the plane wave basis set is put at 30 Ry with a charge density cut-off of 240 Ry. The path for the calculations of the $\mathbf{k}$-points in the band structure follows the nomenclature for the monoclinic structure reported in reference [127].

In conclusion, we find that apart from the morphological difference, the exfoliated nanoribbons and nanosheets also display different electronic and optical properties. The FETs fabricated using nanosheets have high mobilities up to $73\,\mathrm{m^2\,V^{-1}\,s^{-1}}$ while those fabricated using individual nanoribbons present lower mobilities but higher gate tunability and optical response. As argued before within DFT calculations, these differences can be attributed to an increased concentration of sulphur vacancies in the nanosheets compared with the nanoribbons (n-type doping). This demonstrated control over the morphology and electrical properties of TiS_3 opens the door to other members of the trichalcogenides family, broadening the collection of materials which can be exfoliated down to a single layer and incorporated in next generation electronics. This work constitutes a first step towards exploiting the almost unexplored trichalcogenide family in 2D electronics application such as chemical sensors or van der Waals heterostructures where a large surface area is highly beneficial.

6.3 Strain-induced Band-Gap Engineering in Layered TiS_3[*]

The exfoliation of a few layer TiS_3 is a relatively recent achievement [90]. As we have seen in the previous section, it is possible to obtain different morphologies as well as control several distinct electrical properties of TiS_3. In particular, the presence of S vacancies has an important effect on the electronic transport properties of few-layer nanoribbons [91, 128]. In this section, we show that one can additionally control the bandgap by inducing compressive and expansive uniaxial strain. By DFT calculation we find that the monolayer and bilayer exhibit a transition from a direct to an indirect gap when the strain is increased in the direction of easy transport. The ability to control the bandgap and its nature can have wide impact in the use of TiS_3 for optical and electrical applications. Additionally, we verify our prediction by stretching a thin TiS_3 sample and by measuring the bandgap via optical absorption spectroscopy. We experimentally find a bandgap increase of up to 10% upon tensile stress applied along the easy-transport direction.

We have calculated the electronic band structure of mono- and bilayer TiS_3 within DFT and we found that they are direct gap semiconductors with a DFT gap of 0.31 eV and 0.27 eV,

---

[*] This section is based on the article *"Strain-induced bang-gap engineering in layered TiS_3"*, submitted (2016), by R. Biele, E. Flores, J. R. Ares, C. Sanchez, I. J. Ferrer, G. Rubio-Bollinger, A. Castellanos-Gomez, and R. D'Agosta.

respectively.* For these two materials considered here, a more refined calculation based on non-self-consistent *GW* method (or hybrid functionals) opens up the gap to the experimental levels (about 1 eV) [92]. In order to study the strain-induced bandgap modulation, we applied a stress by deforming the length of the unit-cell vector in either the $\mathbf{a}$ or the $\mathbf{b}$ direction and relaxed the atomic positions.† Figure 6.4 shows the bandgap change ΔE_G for mono- and bilayer $\mathrm{TiS_3}$. E_G refers to the bandgap of the material when strain is not applied. Interestingly, a compression in $\mathbf{b}$ direction leads to a reduction of the direct gap up to -3$\%$, applying -4$\%$ or more strain transforms the gap into an indirect one by keeping the gap constant at around one third of its original value. A positive strain in the $\mathbf{b}$ direction leads to a monotonic increase of the gap, by keeping it nature (direct) unchanged. Moreover, while a compression in the $\mathbf{a}$ direction increases the direct gap up to a strain of around -3$\%$, increasing the strain further leads to a reduction of the gap. When the unit cell is expanded in the $\mathbf{a}$ direction the gap first decreases until a strain of around 5$\%$ and by stretching the material further the bandgap increases. That the monolayer and bilayer $\mathrm{TiS_3}$ shows a direct–indirect transition for a compression in the *b*-direction, might have important consequences to tailor the optical and electronic response of possible $\mathrm{TiS_3}$ based phototransistor.

To better understand this transition, the band structure for the unstrained and 5$\%$-strained monolayer in the $\mathbf{b}$ direction is shown in Fig. 6.5. We clearly see that the conduction bands are almost untouched by the compression, while the valence bands develop a local maximum between Γ and *H*, reducing the gap and changing its nature. Interestingly, the reduction of the bandgap in the transition from direct to indirect is here more marked than what has been reported in $\mathrm{TiS_3}$ nano-ribbons, where the reported bandgap modification is of only a few meV [129], in certain cases below the accuracy of the pseudo-potentials used in DFT.

In order to experimentally verify the predicted effect of strain on the electronic band structure of $\mathrm{TiS_3}$ we study the optical absorption spectra of a thin $\mathrm{TiS_3}$ ribbon subjected to uniaxial strain. The strain is applied by exploiting the buckling-induced de-lamination process that takes place when a thin elastic film, deposited onto an elastomeric substrate, is subjected to an uniaxial compressive strain [130, 131]. The trade-off between the bending rigidity of the thin-film

---

[*] Note that those values are different than the ones from section 6.2, as here we are using for Ti a pseudopotential that includes semi-core states for the valence electrons. This is needed to perform on top of the DFT results the *GW* approximation.

[†] We here neglect the effect of the Poisson's deformation induced in the other two axes of the unit cell. Preliminary results have shown this effect to be negligible with Poisson's ratios of the order of 0.04–0.08.

and the thin-film/elastomeric substrate adhesion forms wrinkles that delaminate from the elastomeric substrate where the thin-film is uni-axially stretched. We address the reader to reference [132] for more details on the buckling-induced de-lamination process. Figure 6.6 (a) shows a sketch of the process followed to fabricate the uni-axially strained TiS$_3$ sample. A gelfilm substrate (a commercially available elastomeric substrate) is uni-axially stretched by 30%, then TiS$_3$ is deposited onto the stretched surface and the strain is suddenly released yielding to the buckling-induced de-lamination to the TiS$_3$ (see Fig. 6.6 (b)) with flat regions (released stress) and delaminated wrinkles (accumulated tensile stress). For thin TiS$_3$ ribbons (10 nm to 30 nm thick, like the one studied here) the wrinkles are 100 nm–300 nm in height, the estimated maximum tensile strain on the topmost part is in the order of 0.3–0.7% [130, 133]. The change in the band structure induced by the applied uniaxial strain along $\mathbf{b}$ is probed by a recently developed hyper-spectral imaging based absorption spectroscopy technique. We address the reader to Ref. [134] for details on this technique. Figure 6.6 (c) shows the absorption spectra α^2 acquired on nine flat regions and on top of four wrinkles. The intercept with the horizontal axis of the relationship α^2 vs. energy gives an estimate of the bandgap (valid for direct gap semiconductors, for indirect ones it should be $\alpha^{1/2}$ vs. energy). The obtained bandgap value in the flat region, 0.99 eV, is in good agreement with the value determined by conventional absorption spectroscopy and by photocatalysis measurements on bulk material [92, 135]. On the

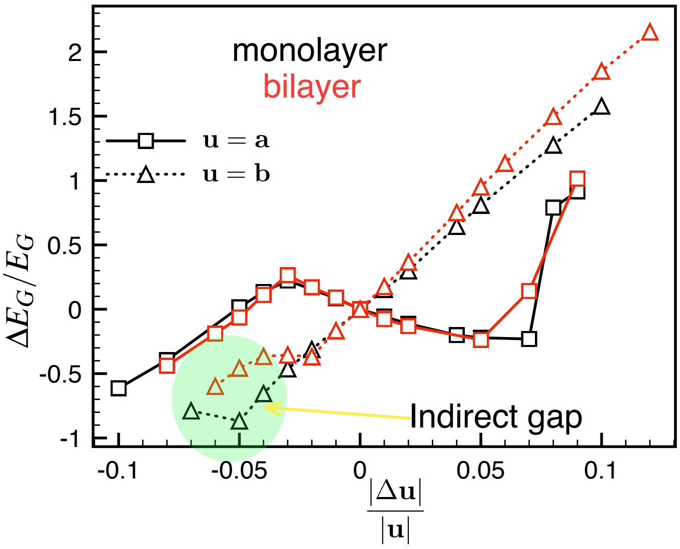

FIGURE 6.4: Modulation of the direct bandgap of mono- (black) and bilayer (red) TiS$_3$ by applying tensile or compressive strain, along the unit-cell vector $\mathbf{a}$ or $\mathbf{b}$. All gaps are direct except the green shaded area: A direct to indirect gap transition is predicted when negative strain is applied to the $\mathbf{b}$ direction at around -4%.

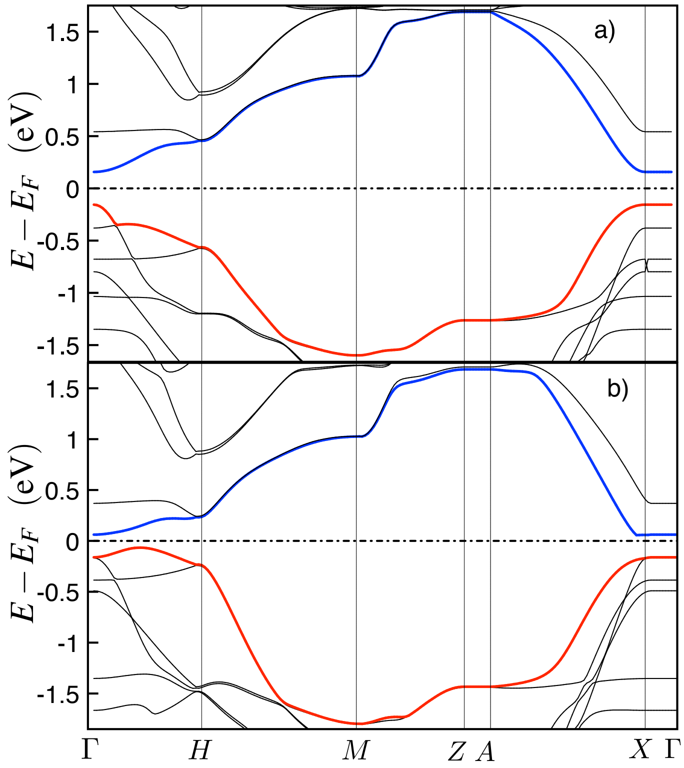

FIGURE 6.5: Electronic bands for the monolayer TiS_3 for the relaxed cell structure (top) and the one where we compressed 5% the unit cell in the $\mathbf{b}$ direction (bottom). In blue and red we represent the conduction and valence band, respectively. a) The upper plot, corresponding to the relaxed unit cell, shows an direct gap at the Γ-point. b) The compressed structure shows a decreased indirect gap between Γ and H. The compression strongly modifies the valence band between these two points. All the energies have been rescaled to the Fermi energy E_F.

topmost part of the wrinkles the slope of the absorption band edge increases considerably yielding an estimated bandgap value of 1.08 eV, 90 meV higher than on the unstrained TiS_3. This experimental observation proves that 0.3–0.7% uniaxial tensile strain along $\mathbf{b}$ locally changes the band structure opening the bandgap, without changing the nature of the bandgap which remains direct (as evidenced by the marked linear behaviour of the absorption band edge in the representation α^2 vs. energy). The experimental value also confirms the quite high sensitivity of these samples as predicted by our calculations. From Fig. 6.4 one can infer for small amplitude strains the linear relation $\Delta E_G/E_G \simeq 20\ |\Delta\mathbf{u}|/|\mathbf{u}|$ for strains in the $\mathbf{b}$ direction in relatively good agreement with the experimental value of 13–30. Note that the large uncertainty of the experimentally determined strain tunability stems from the difficulty in estimating the actual strain applied to the sample.

To calculate the electronic band structure, we have performed DFT calculations. For both Ti

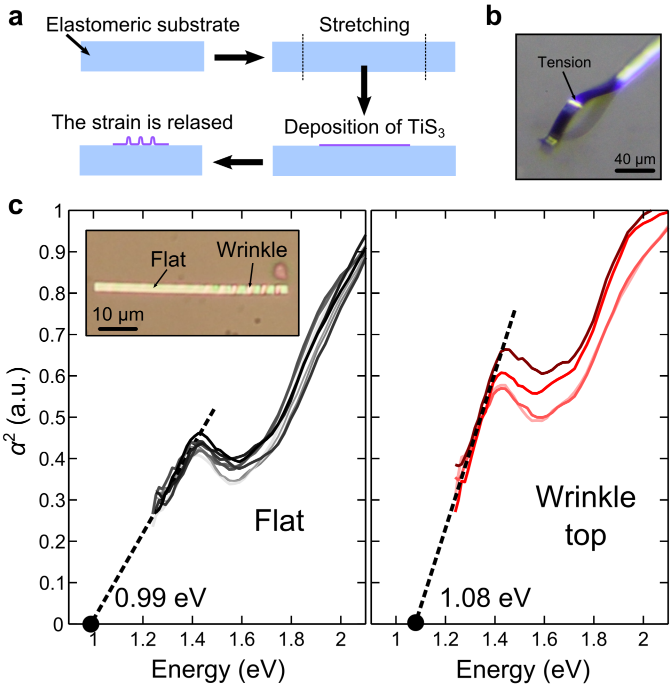

FIGURE 6.6: (a) Schematic diagram of the steps employed to fabricate uni-axially strained TiS_3 exploiting the buckling-induced de-lamination process. (b) High-angle optical microscopy image of a delaminated wrinkle occurring on a thin TiS_3 ribbon. (c) Optical absorption spectra acquired on nine different flat regions (left) and on the topmost part of four wrinkles on a thin TiS_3 ribbon (shown in the inset). The intercept with the horizontal axis indicates the estimated bandgap value in the different regions.

and S, the electron exchange–correlation potential is evaluated within the generalised gradient approximation throughout the Perdew–Burke–Ernzerhof's functional. For S the Martins–Troulliers' pseudopotential is used, while for Ti the Goedecker–Hartwigsen–Hutter–Teter's pseudopotential, including semi-core states for the valence electrons, is used [136, 137]. These pseudopotentials are norm-conserving and scalar relativistic. By starting from the experimental parameters for the unit cell [91] and the spectroscopical atomic configuration [138], we have optimised the atomic positions with a residual force after relaxation of 0.001 a.u.. The kinetic energy cutoff for the basis set is put at 220 Ry, while the cutoff for the charge density is 880 Ry. The sampling of the Brillouin zone for the mono- and bilayer material we used a **k**-point mesh of 14×14×4. The parameters chosen ensure a convergence of the DFT bandgap within an accuracy of around 0.01 eV. We have not included van der Waals corrections in these calculations since from our previous experience we have seen they have essentially no effect on the electronic bands.

In conclusion, we have done a systematic investigation of the bandgap modifications of monolayer and bilayer TiS_3 material when the system is subject to compressive and tensile strain. We found at zero applied strain for the mono- and bilayer material a direct bandgap of 0.31 eV and 0.27 eV, respectively. These values, although in good agreement with other theoretical calculations, are about 1/3 of the experimental bandgap value, a not surprising result considered that DFT usually underestimate the electronic bandgap. We found that the gap can be controlled by inducing strain in certain directions along the primitive axes of the unit cell. Most interestingly, we found that the gap of the monolayer and bilayer material changes from direct to indirect when compressive strain is induced along the preferred transport axis (b in Fig. 6.1). We tested our predictions by inducing strain in a TiS_3 sample: the gap increases when the system is under tensile strain, in agreement with the theoretical predictions of Fig. 6.4. This behaviour is mostly noticeable, since for other two dimensional di-calchogenides materials the gap always closes for tensile strain, and can open a set of potential application for TiS_3.[*] At the moment we are reaffirming our results by calculating the *GW* corrections to the strain-induced bandgap modification. First results indicate that the *GW* approximation opens the gap for the unstrained and strain materials and that the nature of the gap coincides with the DFT ones. In addition, to better compare with the experiment we are planning to solve the BSE for the strained cases. This will give us access to the optical gap, however, we do not expect a crucial difference between the optical and electrical gap. In our experience the exciton binding energy is relatively small in comparison to the bandgap for this material.

6.4 Electrical and Optical Anisotropy of TiS_3[†]

The isolation of atomically-thin van der Waals materials has triggered a strong research focus on this broad family which can be exfoliated from bulk layered crystals [26, 141, 142]. However, research has been mainly focused to boron nitride, graphene, and the Mo– and W– based

---

[*] During the elaboration of this work we became aware of two theoretical works where, the general properties of the MX_3 materials (where M = Ti, Zr and Hf; while X = S, Se, Te) [139], the effects of tensile a strain on the bandgap of single layer [140] and nano-ribbons [131] of TiS_3 are studied. However, those works just include tensile strain and hence do not report the strong direct–to–indirect gap transition found here. They report a insignificant transition of a few meV for tensile strain. This value is close to the accuracy of the DFT numerics and a negligible effect.

[†] This section is based on the article
"Titanium trisulfide (TiS_3): a 2D semiconductor with quasi-1D optical and electronic properties", Scientific Reports **6**, 22214 (2016), by J. O. Island, R. Biele, M. Barawi, J. M. Clamagirand, J. R. Ares, C. Sánchez, H. S.J. van der Zant, I. J. Ferrer, R. D'Agosta, A. Castellanos-Gomez.

TMDCs [143, 144]. These materials have largely isotropic in-plane optical and electrical properties. Breaking this in-plane symmetry could lead to interesting anisotropic effects advancing the functionalities of 2D materials. For instance, anisotropic 2D materials could be used to fabricate passive optical polarisers. TiS_3 is a promising material due to its bonding asymmetry [145]. Differences in the Ti–S bond length along the a (2.65 Å) and b (2.45 Å) axes can be found. These differences lead to highly conducting 1D chains along the b-axis and result in strong anisotropic properties [97]. *Ab initio* calculations have reported electron mobility for the b-axis of more than $10\,000\,\mathrm{cm^2\,V^{-1}\,s^{-1}}$ (higher than MoS_2) and a-axis mobilities of more than an order of magnitude less [97]. Up to date, an experimental investigation of the anisotropic properties of TiS_3 is still missing.

Therefore in our article [146], we investigate the electrical and optical properties of few-layer TiS_3, considering especially in-plane anisotropic effects. We use a combination of angle resolved polarisation Raman spectroscopy, optical transmission and electrical transport measurements to study the anisotropic behaviour of thin TiS_3. At room temperature the electrical conductivity shows an anisotropy of $G_{max}/G_{min} = 2.1$ and can even reach $G_{max}/G_{min} = 4.4$ at low temperatures. Additionally, we report that the Raman spectra of thin flakes show strong in-plane anisotropy. This could be useful to align few-layer TiS_3. Interestingly, the optical absorption of TiS_3 depends on the relative orientation between the incident polarised light and the lattice of the material. This strong linear dichroism is a magnitude greater than that observed for other anisotropic 2D materials. In order to better understand and confirm these results we have investigated theoretically the absorption and transmittance spectra in the **random phase approximation (RPA)** [147, 148].

Here in this thesis, we will concentrate on the anisotropic optical properties of TiS_3 by discussing the optical transmission measurements, the calculated absorption and transmittance spectra. Details on the study of anisotropic effects in the electrical transport properties, as well as the angle resolved polarisation Raman spectroscopy, can be found in [146]. Essentially, the Raman spectroscopy has been used to determine the crystalline orientation of exfoliated TiS_3 nanosheets whose b-axis direction cannot be distinguished at a glance from the material morphology like in the case of nanoribbons. The aligned TiS_3 nanosheets, grown at 400 °C as reported in section 6.2, have been used to study the optical anisotropy using transmission mode optical microscopy. In order to study the optical properties with a transmission microscope, a linear polariser is located between the condenser lens and the microscope light source.

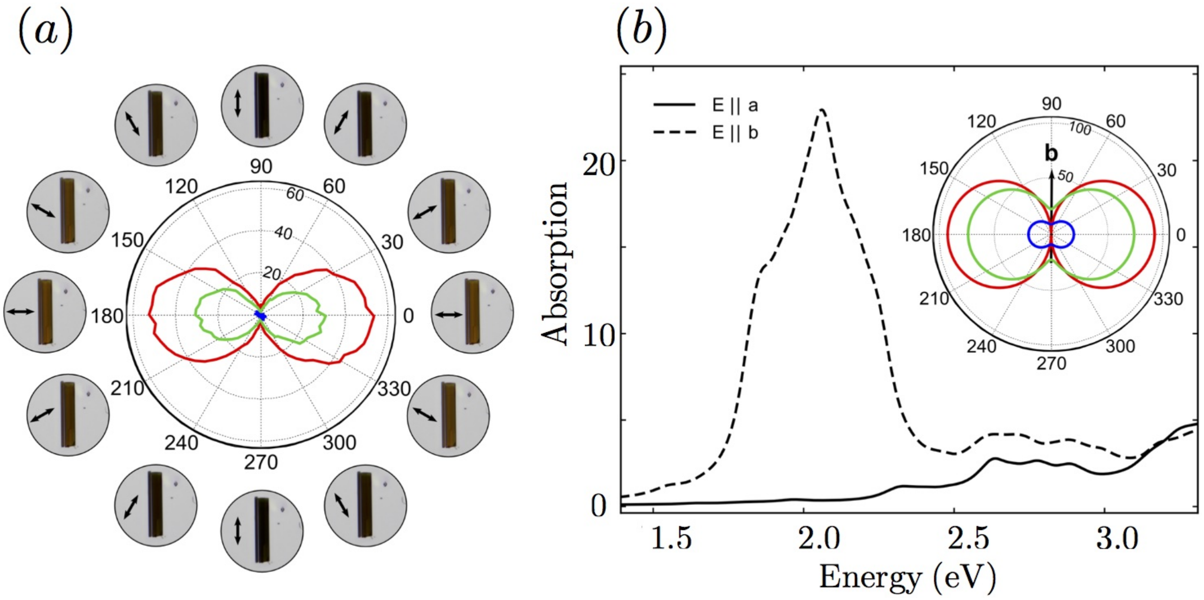

FIGURE 6.7: (a) Transmittance of the red, green, and blue channels as a function of the excitation polarisation angle. (b) Calculated RPA absorption spectra when the field is aligned parallel to the *b*-axis (black dashed line) and *a*-axis (black solid line). The inset shows the transmittance in the *a*–*b*-plane for energies red (1.9 eV), green (2.3 eV), and blue (2.72 eV) excitations. (Plots reused from our article [146])

While the polariser is rotated in steps of around three degrees, transmission images are obtained. Through normalising of the intensity measured on the TiS_3 by the intensity measured on the nearby bare substrate, the transmission is calculated.

Figure 6.7 (a) shows the dependence of the transmission on the angle between the polarised light and the *b*-axis of the TiS_3 sheet. One can see a strong variation in the optical absorption when changing the polarisation angle of the incident light in respect to the crystal structure. The transmission reaches a minimum value when the incident light is polarised parallel to the *b*-axis. The high conducting 1D chains, parallel to the *b*-axis, absorb the light with a polarisation that is parallel to it. This behaviour is very similar to that of a wire grid polariser. The reader can find similar measurements made on a nanoribbon, where the *b*-axis can be easily determined in the appendix C. The ratio between the *b*-axis and the *a*-axis transmission can reach values as high as 30 and decreases for thinner flakes (see appendix C Fig. C.2). For a direct comparison, we measure the transmission of multilayer black phosphorus and MoS_2 flakes of similar absolute transmission which present transmission ratios of approximately 1.4 and approximately 1, respectively (see Fig. C.3 in appendix C).

To better understand and confirm this linear dichroic behaviour, we perform DFT calculations in combination with many-body techniques to calculate the absorption spectrum for bulk TiS_3. Figure 6.7 (b) shows the calculated absorption spectra for bulk TiS_3 when the electric field is aligned parallel to the a-axis (black solid line) and b-axis (black dashed line). Across the visible wavelengths, the absorption is much larger when the excitation field is parallel to the b-axis than when it is parallel to the a-axis. The inset in Fig. 6.7 (b) shows the calculated transmittance in the a–b-plane for red (1.9 eV), green (2.3 eV), and blue (2.72 eV) excitations. We find qualitative agreement with our experimental findings. The transmittance is maximum (lowest absorption) for light polarised perpendicular to the b-axis and minimum (highest absorption) for light polarised along the b-axis. Additionally, for polarisations perpendicular to the b-axis, the maximum transmittance decreases with increasing excitation energy (red to blue, 1.9 eV to 2.72 eV).

Both for Ti and S, the exchange–correlation potential is described self-consistently within the generalised gradient approximation throughout the PBE functional. For S a norm-conserving Martins–Troulliers' pseudopotential is used, while for Ti a norm-conserving Goedecker–Hartwigsen–Hutter–Teter's pseudopotential, including semi-core states for the valence electrons, is used [136, 137]. We have relaxed the atomic positions and the unit cell vectors with a residual force after relaxation of 0.001 a.u. by starting from the atomic positions provided in [91]. The kinetic energy cutoff for the plane wave basis set is 180 Ry. The sampling of the Brillouin zone is $10\times10\times10$ according to the Monkhorst–Pack scheme. As DFT tends to underestimate the electronic bandgap, we performed non-self-consistent G_0W_0 [149, 150] calculations in order to get accurate values for the electronic band structure. The local field effects in the screening calculations have been taken into account and we carefully converged the electronic quasi-particle gap. The G_0W_0 corrected DFT bands have been used to calculate the absorption spectra in the RPA. To construct the kernel in the RPA we have considered 30 valence and 120 conduction bands. The size of the response function has been carefully converged, hence local field effects corresponding to charge oscillations are accurately included.

In summary, we present optical measurements of the in-plane anisotropy of TiS_3. From electrical measurements we calculate an anisotropy in the in-plane conductivity of 2.1 at room temperature and 4.4 at a temperature of 25 K [146]. Furthermore, through optical transmission measurements and DFT calculations we show that TiS_3 exhibits strong linear dichroism where the ratio in the transmission between the b-axis and a-axis reaches values as high as 30. The strong anisotropic properties of TiS_3 set it apart from the commonly studied 2D materials which have largely isotropic properties and makes it an interesting material for future applications.

6.5 Electronic Bandgap and Exciton Binding Energy of TiS_3[*]

The discovery of single-layer TMDCs has boosted the interest on layered semiconducting materials. Layered Mo– and W– based dichalcogenides present very exotic optical properties like an unusual large exciton binding energy, 100–1 000 times larger than that of conventional 3D semiconductors. This makes it possible to observe a plethora of excitonic effects even at room temperature. The bandgap of Mo– and W– dichalcogenides, however, limits their application to only part of the visible spectrum. Therefore, a narrower direct bandgap semiconductor, which also presents a large exciton binding energy, would be highly desirable for applications aiming to exploit excitonic physics in the near-infrared part of the spectrum (such as night-vision imaging or fiber-optic-communication). TiS_3 has triggered a lot of recent interest because of its direct bandgap of around 1.0 eV that bridges the gap between graphene (zero gap) and single-layer MoS_2 and WS_2 (1.8–1.9 eV). In our article [92] we present **scanning tunnelling microscope** (**STM**) and **scanning tunnelling spectroscopy** (**STS**) characterisation of this material. This allows us to determine the exciton binding energy and, as far as we know, we report the first *ab initio* calculations of the optical absorption of TiS_3. Therefore, our results open the door for future works on the barely studied trichalcogenides family.

As we have seen in section 6.2 that TiS_3 grows on layered ribbon-like shape showing n-type conduction behaviour with mobilities up to 73 $cm^2\,V^{-1}\,s^{-1}$ and ultrahigh photoresponse up to 2 910 $A\,W^{-1}$. Here, we investigate the electronic and optical bandgap in TiS_3 ribbons, which are 30 to 130 layers thick. The electronic bandgap is measured within STS while the optical gap is determined by photo-electrochemical measurements, obtaining experimentally 1.2 eV and 1.07 eV, respectively. In order to confirm those values, we have calculated the electronic bandgap within the G_0W_0 approximation and the optical gap by solving the BSE. For the electronic bandgap we find a value of 1.15 eV and for the optical gap we find 1.05 eV, which are both in good agreement with the experimental data. From these two values we are able to estimate the exciton binding energy of TiS_3 ribbons as the difference between the electronic bandgap and the optical one. The theoretical binding energy of bulk of 100 meV coincide well with the experimental binding energy of 130 meV. This exciton binding is around two orders

---

[*] This section is a part of the article *"Electronic bandgap and exciton binding energy of layered semiconductor TiS_3"*, Advanced Electronic Materials **1**, 9 (2015), by A. J. Molina-Mendoza, M. Barawi, R. Biele, E. Flores, J.R. Ares, C. Sánchez, G. Rubio-Bollinger, N. Agraït, R. D'Agosta, I. J. Ferrer, and A. Castellanos-Gomez.

of magnitude larger compared to common semiconductors and thus making TiS_3 a extremely promising nano-material for the investigation of exitonic effects.

TiS_3 ribbons are transfered onto a gold substrate in order to prepare the STS and photo-electrochemical measurements. For this, a viscoelastic stamp is brought into contact with the TiS_3 ribbons grown at 500 °C. By peeling off the stamp, several ribbons were transferred to the stamp and placed onto the gold surface. Further details about this process can be found in the Supporting Information of [92]. Optical microscopy images and **atomic force microscopy** (**AFM**) images can be seen in Fig. 6.8 (a). This sample is studied with a STM at ambient conditions [151]. Regions of the sample uncovered with TiS_3 can be easily distinguished by their high conductance at zero bias in the current–versus–voltage curves (called IVs hereafter). Figure 6.8 (b) compares STS IVs acquired on TiS_3 ribbons and on gold. While for gold the curve profile is that expected for a metal–vacuum–metal junction, for TiS_3 it shows a clear drop of the current down to zero when the bias voltage shifts the Fermi level within the TiS_3 bandgap. The STM tip is then placed onto a TiS_3 ribbon and 205 IVs have been measured on different samples. By averaging over those 205 IVs the measured value for the valence band is E_{VB} = (-0.64±0.06) eV, while for the conduction band the measured values is E_{CB} = (0.47±0.06) eV. Here, we can see a shift of the Fermi level towards the conduction band, indicating n-type semiconducting behaviour. Additionally, in STS measurements at ambient conditions one needs to take into account that the current–voltage curves are thermally broadened, which leads to a slightly underestimation of the bandgap value. The thermal broadening is induced by the temperature dependence of the Fermi–Dirac distribution function, which enters via the requirement that electrons tunnel in STS from occupied states in the tip to unoccupied states in the sample [152]. Therefore, in our STS measurements at temperature T, the bandgap has been reduced by $E_t \approx 3.5 k_B T = 90\,\mathrm{meV}$ [152]. This leads to an electronic bandgap of around 1.20 eV. The interested reader can found more details in our corresponding article [92].

On the other hand, with photo-electrochemical measurements the optical bandgap was determined. Details about this techniques can be found in [92] in the Experimental Sections. The photocurrent response density as a function of the light wavelength for TiS_3 is represented in a so-called Tauc plot [153] in Fig. 6.9 (a). The optical gap (1.05 eV) can be found by the point where the linear approximation of the data intersects the horizontal axis. Depending on the shape of the spectra, this method gives also insights about the nature of the gap [153]. The linear fit $(I_{\mathrm{ph}} h\nu)^n$ versus $h\nu$ for $n = 1/2$ indicates an indirect transition while $n = 2$ demonstrates a direct transition. We find two direct transitions at 1.05 eV and 1.29 eV. Here, the first

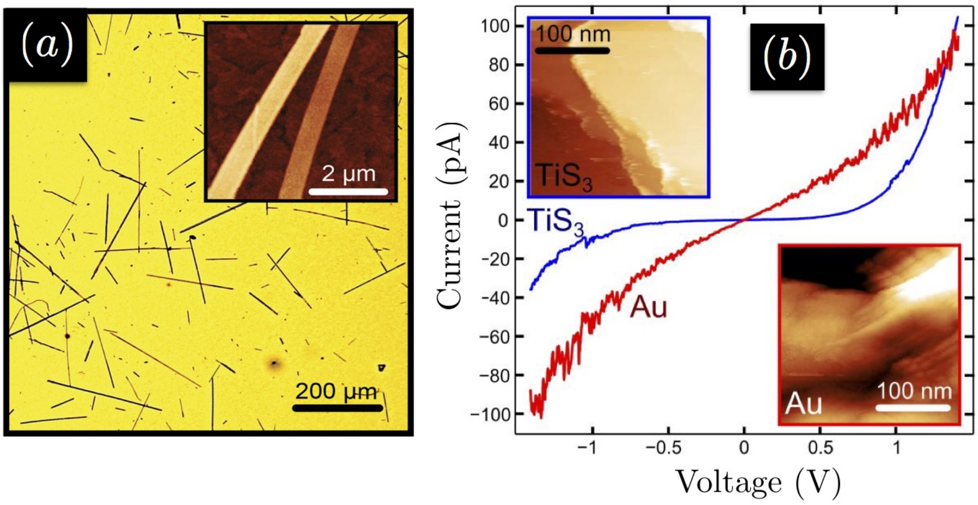

FIGURE 6.8: (a) Optical microscopy image of TiS_3 ribbons on a gold substrate. Inset: AFM topographic image of two TiS_3 ribbons. (b) STS current–voltage characteristics of TiS_3 (blue) and bare gold (red). Insets: STM topographic images of TiS_3 (blue frame) and bare gold (red frame). (Plots taken from [146])

transition corresponds to the formation of the first excitonic state. These values agree well with previously reported ones obtained for TiS_3 samples grown under different condition [135, 154].

To interpret our experimental results, we performed state-of-the-art DFT calculations in combination with many-body techniques. We first investigated the electronic structure of bulk TiS_3 within DFT. As the experimentally studied TiS_3 ribbons are relatively thick, this might be well described with bulk TiS_3. Additionally, we performed G_0W_0 calculations on top of the DFT electronic bands in order to get an accurate value for the electronic bandgap. To access the optical properties, like the optical gap, one has to include the interaction between the excited electron in the conduction band with the hole created in the valence band. For this we solved the BSE starting from the G_0W_0 corrected DFT results [149, 150]. In Fig. 6.9 (b) the absorption spectra of bulk TiS_3 are shown with (BSE) and without (RPA) electron–hole interaction. The absorption peak in the RPA spectrum at $E_{\mathrm{el}} = 1.15\,\mathrm{eV}$ coincides with the electronic bandgap, while the peak of the BSE spectrum at $E_{\mathrm{op}} = 1.05\,\mathrm{eV}$ gives the optical gap. The peaks at around 1.2 eV correspond to an optical transition to a higher energy level in the conduction band, as mentioned in reference [91]. Hence, the exciton binding energy is 100 meV, in excellent agreement with the experimental results.

Both for Ti and S, the exchange–correlation potential is described self-consistently within the generalised gradient approximation throughout the PBE functionals. For S the Martins–Troulliers' pseudopotential is used, while for Ti the Goedecker–Hartwigsen–Hutter–Teter's

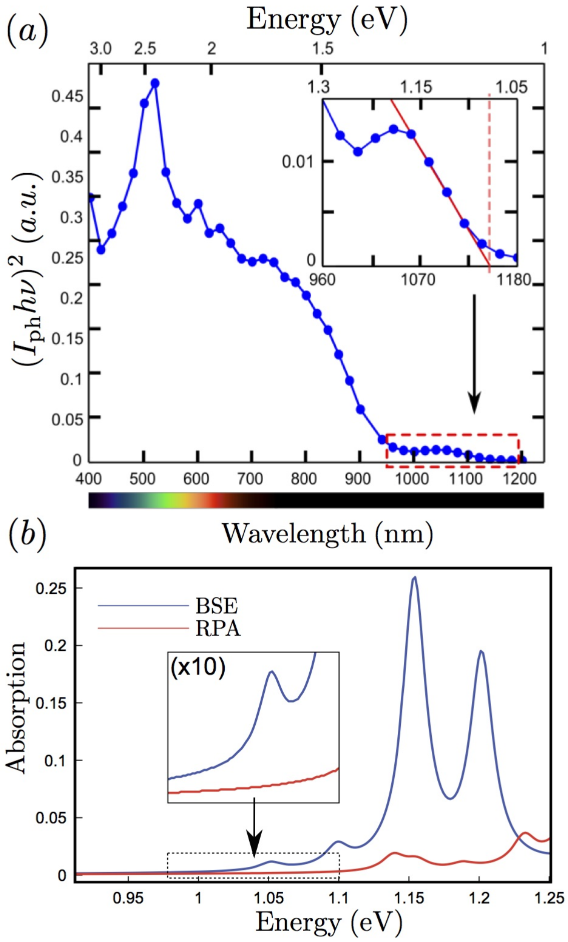

FIGURE 6.9: (a) Photocurrent density as a function of light wavelength. The optical bandgap is determined by a linear interpolation as described in the text and shown in the inset. (b) Calculated absorption spectra for TiS$_3$ within RPA (red) and by solving the BSE (blue). The first small peak of the BSE spectrum at 1.05 eV indicates the optical gap, while the first peak of the RPA spectrum at 1.15 eV coincides with the electronic bandgap. (Plots taken from [146])

pseudopotential, including semicore states for the valence electrons, is used [136, 137]. These pseudopotentials are norm conserving and scalar relativistic. By starting from the lattice parameters provided in reference [91] we have optimised the atomic positions with a residual force after relaxation of 0.001 a.u.. The kinetic energy cutoff for the plane wave basis set is put at 180 Ry, while the cutoff for the charge density is 720 Ry. The sampling of the Brillouin zone is 10×10×10 according to the Monkhorst–Pack scheme. To go beyond the DFT–PBE level the electronic structure is further corrected by means of non-self-consistent G_0W_0 approximation. The screening in the G_0W_0 calculation is treated within the so-called plasmon pole approximation [149, 150]. The local field effects in the screening calculations have been taken into account and we carefully converged the electronic quasiparticle gap. When looking at two-particle properties such as absorption of light, one has to include the interaction between the excited electron in the conduction bands with the hole created in the valence band. For this we solved the BSE using the recursive Haydock method to access the optical gap [155–157]. To construct the BS kernel in the static approximation we considered 30 valence and 70 conduction bands [158]. The position of the first peak in the optical spectrum, which corresponds to the optical gap, has been carefully converged for example with respect to the $\mathbf{k}$ point sampling, the components to be summed in the exchange part and those of the screened coulomb potential of the BSE kernel. In order to make the first peak in the BSE spectrum better visible, in Fig. 6.9 we have plotted only the transitions between the highest occupied and the lowest unoccupied electronic states. Increasing the number of considered bands in the BSE spectrum does not shift the first peak position, however it becomes difficult to spot it as its amplitude is small.

To summarise, we have measured the electronic and optical bandgap of layered TiS_3 ribbons. Within STS and photo-electrochemical measurements we find 1.2 eV for the electronic and 1.07 eV for the optical bandgap. With this we are able to calculate the exciton binding energy of TiS_3 ribbons as 130 meV. Additionally, we have obtained by RPA and BSE calculations, 1.15 eV for the electronic bandgap and 1.05 eV for the optical bandgap. These theoretical results are in good agreement with the experimental values. The binding energy of TiS_3 is around two orders of magnitude larger than that of typical semiconductors such as germanium, silicon or gallium arsenide.

6.6 Quantum Confinement Effect in the Optical Properties of Ultra-thin In_2Se_3[*]

In this last section of the chapter, we will study the effect of quantum confinement in the optical and electronic bandgap of atomically thin α-In_2Se_3 crystals. In_2Se_3 is a very interesting direct gap semiconductor, with promising application in ultraviolet photo-detection. We observe a marked thickness-dependent shift in the optical absorption spectra acquired on mechanical exfoliated α-In_2Se_3 flakes. This observed variation of the optical bandgap due to quantum

---

[*] This section is based on the submitted article
"Strong quantum confinement effect in the optical properties of ultrathin In_2Se_3", submitted (2016), by J. Quereda, R. Biele, G. Rubio-Bollinger, N. Agraït, R. D'Agosta, and A. Castellanos-Gomez.

confinement is among the largest reported to date in 2D semiconductors materials, comparable to that of atomically thin black phosphorus. For instance, the bandgap in Mo– and W– based TMDCs increases from a value of about 1.3 eV (indirect gap) for bulk to 1.9 eV (direct gap) for a single layer [26, 159]. A stronger effect has been found more recently for black phosphorus ranging from around 0.3 eV (direct) for bulk up to 1.75 eV for a single layer [160]. Those thickness-dependent bandgap variations can be very advantageous for applications as photodetectors as one can select the sensible photon energy windows by simple changing the material thickness. However, up to now there is a broad spectral window from 2 to 3 eV uncovered by 2D materials that could be very relevant for applications requiring ‘solar blind’ semiconducting materials (not absorbing within the visible spectrum) but responsive to near-UV light.

Here, we report a very strong quantum confinement effect in the optical properties of α-In_2Se_3 flakes. While for the thicker flakes (95 nm) we find experimentally an optical bandgap of around 1.45 eV, thin flakes shows a remarkable increase of their optical bandgap, reaching up to 2.8 eV for the thinnest flake (3.1 nm) studied here. To better understand and support the experimental findings, we have performed DFT calculations in combination with many-body techniques. Our calculations serve to obtain the band structure for bulk α-In_2Se_3 from where we extract the effective mass of the exciton and the electronic bandgap of 1.4 eV in good agreement with the experiment. Furthermore, we have also calculated the optical gap by solving the BSE. Our results indicate a relatively small binding energy of the exciton. Those results, we have used to estimate theoretically the quantum confinement effect of the optical gap via a square quantum well potential.

Atomically thin In_2Se_3 flakes are prepared by mechanical exfoliation of a bulk α-In_2Se_3 crystal and transferred to a poly-dimethylsiloxane substrate. This substrate has been selected because of its high transparency in the visible range and low interaction with thin flakes. Figure 6.10 (a) shows an optical image of the In_2Se_3 flake with regions of different thickness, as well as an AFM scan along the dashed line. The optical absorption has been studied by using a homemade hyper-spectral imaging setup described in details elsewhere [161]. This is carried out by sweeping the excitation wavelength and acquiring transmission mode images of the In_2Se_3 crystal at each wavelength.

Figure 6.10 (b) shows five of those wavelength-dependent optical transmittances for different thickness, ranging from 3.1 nm to 25 nm. Interestingly, we find that for any given illumination wavelength the optical transmittance decreases monotonically with the flake thickness, as

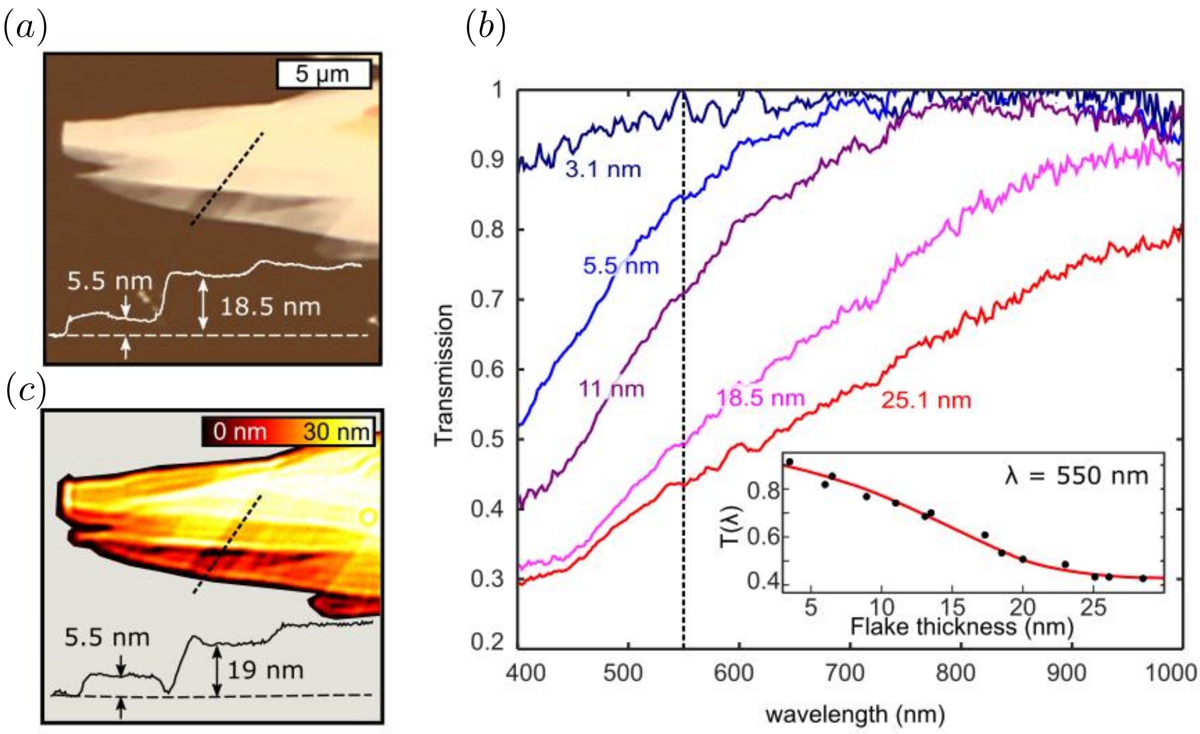

FIGURE 6.10: (a) Transmission optical image of a In_2Se_3 flake with regions of different thickness. Inset: AFM height profile along the dashed black line. (b) Dependence on the transmission versus wavelength curves on the thickness of the flake (3.1 nm to 25.1 nm). Inset: Optical transmission at a wavelength of 550 nm as a function of the flake thickness, where the red curve shows the interpolation of the measured data to a smoothed spline function. (c) Thickness colormap obtained from the hyper-spectral and AFM measurements. For different illumination wavelengths we compare the transmission obtained at each image cell with the corresponding transmission–versus–thickness curve.

shown in the inset for λ = 550 nm. Consequently, this allows to estimate the flake thickness of In_2Se_3 by measuring the transmittance at a fixed illumination wavelength. In addition, this also enables us to generate a thickness map from the measured hyper-spectral images, as can be seen in Fig. 6.10 (c). Here, the inset shows a line profile along the same path measured in the AFM scan of Fig. 6.10 (a). There is a good agreement between the obtained thickness with that measured by AFM. The reader can find more details about the analysis employed to generate the 2D thickness maps from the hyper-spectral datasets in the supporting information of [162].

The absorption coefficient α can be calculated from its transmittance T and its thickness as

$$\alpha(\lambda) = -\frac{\log_{10}(T(\lambda))}{d}. \tag{6.23}$$

According to Tauc *et al.* [163], near the absorption edge α of a direct gap semiconductor follows

$$(\alpha\hbar\omega)^2 = A^2(\hbar\omega - E_g^{\mathrm{opt}}), \tag{6.24}$$

where A is a material-dependent constant and E_g^{opt} is the optical energy gap. In order to determine the optical bandgap, one represents $(\alpha\hbar\omega)^2$ versus the photon energy $\hbar\omega$, and fits the absorption band edge to a linear function. According to the previous equation, the intersection of this linear fit with the horizontal axis yields the value of the optical bandgap. In Fig. 6.11 (a) Tauc plots for the seven In_2Se_3 flake regions with different thickness, as well as their linear fit near the absorption edge can be seen. The optical bandgap strongly depends on the flake thickness, ranging from around 1.45 eV for bulk material to a value of 2.8 eV for the thinnest measured flake. The inset of Fig. 6.11 (b) shows a colormap representing the energy at which the absorption reaches a limit of 10^5 cm^{-1} at each sample position, which is called isoabsorption map. Note that when a small absorption limit is set, the isoabsorption energy approaches the optical bandgap value and thus the isoabsorption map represents accurately the spatial variation of the bandgap. Figure 6.11 (b) shows a comparison between the bandgap extracted from the isoabsorption map and from the linear fit of the Tauc plots.

To gain a deeper understanding on the thickness-dependent bandgap of In_2Se_3, we performed DFT calculations, in combination with many-body techniques. First of all, we investigate the electronic structure of bulk In_2Se_3 within DFT. Furthermore, we have also performed G_0W_0 calculations in order to get an accurate bandgap value to compare with the experiment. Figure 6.12 shows a comparison between the DFT band structure and the G_0W_0 bands. While DFT underestimates the bandgap, G_0W_0 corrects it to 1.40 eV, which is in excellent agreement with the experiment. To access the binding energy and hence the optical gap, we included the interaction between the excited electron with the hole created in the valence band. For this we have solved the BSE starting from the G_0W_0 corrected DFT results [155, 156], leading to a relatively small binding energy of around 80 meV for bulk In_2Se_3.

The evolution of the optical bandgap with the flake thickness can be modelled using a square quantum-well potential of infinite height [164, 165],

$$E_{\mathrm{2D}}^{\mathrm{opt}}(d) = E_{\mathrm{bulk}}^{\mathrm{el}} - E_b + \frac{\pi^2\hbar^2}{2d^2\mu^c}, \tag{6.25}$$

where $E_{\mathrm{bulk}}^{\mathrm{el}}$ is the electronic bandgap for bulk In_2Se_3 (1.4 eV from the G_0W_0 calculations), E_b is the exciton binding energy (E_b = 0.08 eV from the BSE calculation), d is the crystal

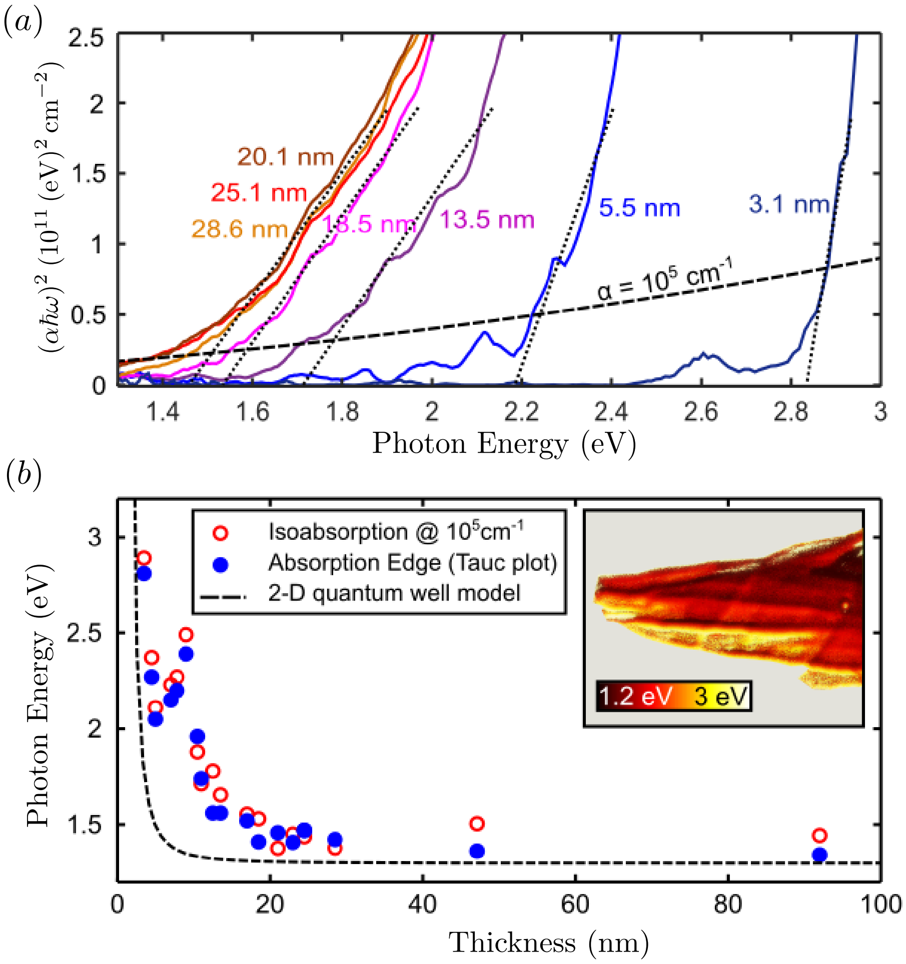

FIGURE 6.11: (a) Tauc plots of the optical absorption for the In_2Se_3 crystal for seven regions with different thickness. The dotted lines show the Tauc extrapolation of the absorption edge in order to obtain the optical bandgap. Furthermore, we show by the black dashed curve when the absorption coefficient takes a value of 10^5 cm^{-1} (isoabsorption energy). (b) Thickness dependence of the optical bandgap energy estimate from the Tauc plots (blue dots) and the isoabsorption at $\alpha = 10^5$ cm^{-1} (red empty circles). The dashed line is a theoretical estimation of the optical bandgap using a 2D quantum well model.

thickness and μ^c is the exciton reduced mass along the c-axis (perpendicular to the layers). This reduced mass has been obtained from the G_0W_0 calculated electron ($m_e^c = 0.13\, m_e$) and hole ($m_h^c = 0.87\, m_e$) effective masses as $\mu^c = (\frac{1}{m_h^c} + \frac{1}{m_e^c})^{-1}$. The estimated bandgap energy via Eq. (6.25), as shown in Fig. 6.11, reproduces the dependence of the optical bandgap on the flake thickness, increasing progressively as the thickness d of the flake decreases. However, compared with the experimental data, the theoretical curve seems to be displaced horizontally towards lower values of thickness. This effect could be attributed to the surface oxidation of the In_2Se_3 crystals under ambient conditions [166], which effectively would reduce the thickness of the In_2Se_3 layer, causing an increase of the measured optical bandgap. On the other hand, it

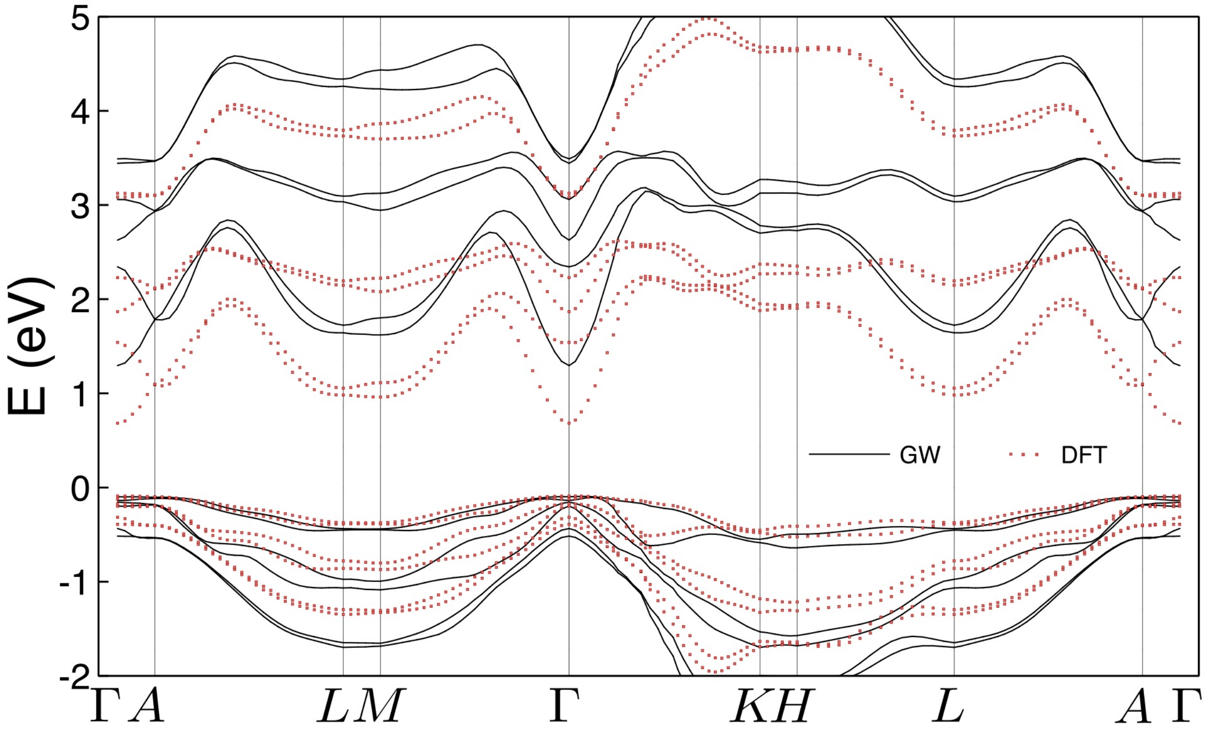

FIGURE 6.12: Band structure for bulk In_2Se_3 within DFT and G_0W_0. While DFT underestimates the bandgap, G_0W_0 corrects it to 1.40 eV, which is in good agreement with the experiment. The effectives masses have been obtained by approximating the bands around the Γ point in the *c*-direction by a quadratic function.

must be noted that the square quantum-well model used here is rather simple as it does not take into account fine details of the thickness-dependent band structure of the crystal. Figure 6.13 shows a comparison of the bandgap shift observed in different atomically thin semiconductors due to the effect of quantum confinement. We observe experimentally a bandgap shift of 1.4 eV, ranging from 1.4 eV in bulk crystals to 2.8 eV in 3.1 nm thick flakes. This unusually high bandgap change, induced by quantum confinement, is among the highest observed in two-dimensional semiconductors [167, 168], comparable with the one observed in atomically thin black phosphorus. Therefore, the bandgap of atomically thin In_2Se_3 crystals can be tuned to cover a wide region of the near ultraviolet spectrum.

For the theoretical investigation, both for In and Se the exchange–correlation potential is described self-consistently within the generalised gradient approximation throughout the PBE functional. The norm-conserving Martins–Troulliers' pseudopotentials are used for both elements, additionally for In semi-core states for the valence electrons have been considered. We have relaxed the atomic positions with a residual force of 0.001 a.u.. The kinetic energy cutoff

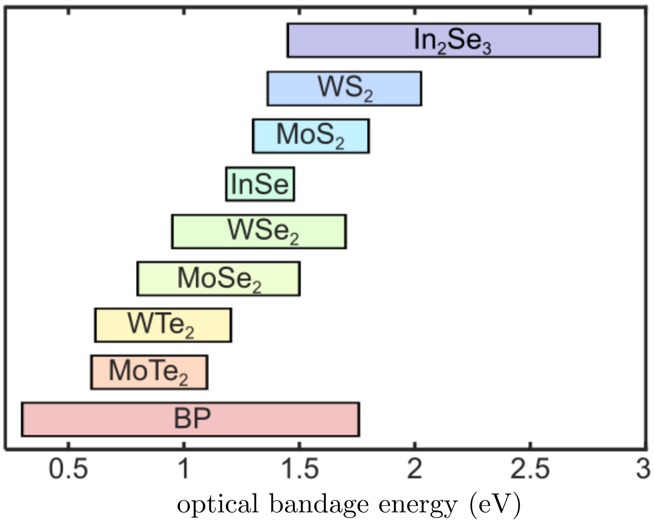

FIGURE 6.13: Comparison of the bandgap values for different van der Waals semiconductor crystals. The horizontal bars spanning a range of energies indicate that the bandgap can be tuned over that range by changing the number of layers.

for the plane-wave basis set is 180 Ry, while the cutoff for the charge density is 480 Ry. The sampling of the Brillouin zone is 9×9×9 according to the Monkhorst–Pack scheme. Local field effects in the screening calculations have been taken into account and we have converged the electronic quasiparticle gap within 0.02 eV. To construct the Bethe–Salpeter kernel in the static approximation we have considered 16 valence and 20 conduction bands. The position of the first peak in the optical spectrum, which corresponds to the optical gap, has been carefully converged for example with respect to the **k** point sampling, the components to be summed in the exchange part and those of the screened coulomb potential of the Bethe–Salpeter kernel.

In summary, we studied the effect of quantum confinement in the optical properties of atomically thin α-In_2Se_3 crystals. We measured the optical absorption spectra of exfoliated In_2Se_3 crystals with thicknesses ranging from 3.1 nm to 25.1 nm, observing a strong thickness-dependent shift of the optical bandgap, from 1.45 eV in the thicker flakes to 2.8 eV in the 3.1 nm thin flakes. In fact, the bandgap variation observed in atomically thin In_2Se_3 due to the effect of quantum confinement is among the largest reported to date in 2D semiconductor materials, and is comparable to that of atomically thin black phosphorus. We performed density functional theory calculations, in combination with many-body techniques, to estimate the bandgap of the bulk In_2Se_3, as well as its exciton binding energy and exciton effective mass. A 2D square quantum well model allowed to reproduce the observed strong thickness dependence of the optical bandgap. In conclusion, this work shows that atomically thin α-In_2Se_3 is a very attractive and barely explored material, specially promising for applications involving tunable near-UV photo-detection.

Chapter 7

Conclusions

In this thesis, different aspects of the interaction of radiation with quantum systems have been studied. This kind of interaction has a wide range of applications, especially nowadays at the nanoscale. When moving from macroscopic systems towards the nanoscale, one reaches the quantum coherence length of many materials, and quantum entanglement effects become more important. Approximations that worked out for macroscopic systems may fail at the nanoscale. Therefore, I have first of all investigated the conditions for thermal relaxation within open quantum systems [72], and we have seen in section 2.2 that those are related to the non-Markovian nature of the equations of motion. The bath-correlation function enters the memory term in the equation of motion. We have seen that this bath-correlation function has to fulfil the detailed-balance relation as a necessary condition for thermal relaxation. This memory term make the equation of motion hard to solve, and by approximating the non-Markovian behaviour one might lose thermalisation. As such, I have numerically investigated in chapter 3 a time-local (time-convolutionless) version of a *non-Markovian* stochastic Schrödinger equation [169], and I have shown that it describes correctly the approach to thermal equilibrium and energy transport as obtained from a general non-Markovian master equation. This is remarkable, since one might expect a more complex time-non-local stochastic Schrödinger equation to be required for reproducing the dynamics of a non-Markovian master equation. This time-convolutionless stochastic Schrödinger equation allows us to study relaxation dynamics and temperature in fermionic and bosonic systems with a stochastic Schrödinger equation that contains non-Markovian effects, at the numerical cost of a Markovian equation. Moreover, contrary to other approximations, e.g., the Born–Markov approximation to the Redfield equation [32], this stochastic equation reproduces the full dynamics of the non-Markovian master equation, and therefore could be used to investigate the transient dynamics and the approach to equilibrium. Additionally, compared to master equations, the time-convolutionless stochastic Schrödinger equation also shows more advantageous scaling with the number of states, which is particularly useful for large systems. However, before such an equation can be applied by scientist not specialised in the numerics of stochastic equations, further theoretical work on integration techniques of such stochastic equations [35] is required. While Itô's calculus is designed for white-noise processes, a corresponding calculus for coloured noise, needed for the time-propagation of the time-convolutionless stochastic Schrödinger equation, is still missing.

After the foundations of thermal relaxation within open quantum systems have been studied, I have addressed out-of-equilibrium quantum systems to study thermal transport. Therefore, I have introduced a novel theoretical framework to investigate energy transport [73] in chapter 4, where the thermal imbalance in the system is introduced by radiation from two classical blackbodies. This theory also takes into account an environment, with which the system can exchange energy. Therefore, the formalism includes the fundamental concept of thermal relaxation of the system. The theory could also be used in different set-ups, e.g., we can consider one blackbody only, to adapt to different experiments. As this formalism relies on the knowledge of the external vector potential, we can foresee that its combination with the powerful techniques of time-dependent current density functional theory will provide a novel *ab initio* tool to study thermal transport in many-body systems. Moreover, within the same formalism we can investigate phonon thermal transport. Thereby combined with the time-dependent current DFT, the model provides a unified way to investigate *ab initio* electrical and thermal transport beyond linear response. Non-linear regimes are important since in seeking for, e.g., the maximum efficiency of a thermoelectric energy converter, we might need to go beyond the standard linear response [170]. Since the formalism is fully dynamic we have direct access to transient regimes. This allows the investigation of how the steady-state is approached, and whether or not this steady-state is unique or depends on the history of the system [171]. However, I would like to emphasise that one needs to improve on how the black-body radiation is modelled. Here, for our numerical investigation we have suggested classical stochastic fields without thermal correlation [70, 71].

When moving from macroscopic systems towards the nanoscale, the measurement process might influence a quantum system and hence has to be taken into account. Therefore, we have studied in chapter 5, with the techniques provided in the previous chapters, the influence of a local measurement in a quantum transport device. Depending on where and how strong these observations are, the direction and magnitude of heat flows can be changed, even having it going against the temperature gradient. Additionally, particle ring-currents can be created and controlled by these observation. Therefore, the choice of location of these quantum measurements can provides full control of the direction of the energy flow and of the particle currents separately. It has appeared that some of these results violate Clausius' formulation of the second law of thermodynamics. To clarify this, we examined the behaviour in terms of non-equilibrium thermodynamic concepts in the quantum regime.

For the investigation of realistic applications of the radiation–matter interaction in nanotechnology, it is also important to have a tool that allows to predict accurately the important properties of real materials within moderate numerical cost. Therefore, I have performed first principle studies within DFT and many-body perturbation theory for 2D layered materials [91, 92, 146, 162, 172, 173]. These materials have established their place as candidates for the next generation of opto-electronic devices, as they present outstanding mechanical and electrical properties and can be easily integrated with conventional silicon technologies. In order to avoid being repetitive, results obtained in the last chapter are not restated here, as they are freshly in mind. The conclusions can be found at the end of each section of chapter 6. However, I would like point out that it was fascinating to see how to model real materials numerically: Starting with placing the atoms in their positions and relaxing their relative coordinates. This allowed us to study their electronic and optical properties, and we could see that the results agreed so well with the 'real world', by reproducing and even explaining or predicting experiments. To summarise the last chapter, electronic and optical properties of TiS_3 and In_2Se_3 have been theoretically and experimentally investigated. I hope that this constitutes as a first step towards exploiting the trichalcogenide family in 2D opto-electronical applications. These applications include chemical sensors, van der Waals heterostructure, FETs, passive optical polarisers, fast photodetectors as well as battery technology.

Although the first principle studies of 2D layered materials and the work done in the thesis on open quantum systems seem to be unconnected at first sight, they are not. Indeed both deal with the interaction of radiation with matter. On the one hand, in the chapters about open quantum systems, the quantum nature of the radiation has been emphasised and the electronic system has been modelled without spending too much efforts. On the other hand, in chapter 6 many-body electronic systems have been described highly accurately within DFT and the radiation has been considered classically. The synthesis of these two approaches, describing the interaction of real materials with photons, is an promising field for future investigations. First work in this direction has been undertaken by generalising the theorem of time-dependent DFT and time-dependent current DFT to the case of open quantum systems. This has been done for both, the reduced density matrix and the stochastic Schrödinger equation formalism [174–177]. However, as in the case of any DFT theory, the form of the functional is unknown, therefore the quality of the results obtained depends on the approximations we are able to make for this functional. At the moment, this is an open area of research. The hope is obviously that standard approximations that have been proven very useful in the past, will provide a solid foundation to explore the reach of this approach. While those approaches solve the time-evolution of an open quantum systems, where the system is described within DFT simultaneously, a first step in this direction would be to investigate the system of interest within DFT or many-body perturbation theory first. This would allow to gain access to its ground-state and excited-state properties and can then be used as an input for the calculation of the dynamics of the open system. At the moment we are working on this approach within photosynthetic systems. By studying the coherent energy transport in these systems, we hope to understand the dynamics of light harvesting in photosynthesis and to answer open questions [178–181].

I hope you, the reader, enjoyed this journey through the fascinating world of the interaction of matter with light in nanoscale systems and also found inspiration and ideas for your own research.

Acknowledgements

I would like to express my special appreciation and thanks to my supervisors Roberto D'Agosta and Angel Rubio. They guided me through but also gave me the freedom to explore physics myself and helped me to become an independent researcher. Without their guidance, advice and support, none of this work would have been possible.

Thanks to my collaborators Andres, Nicolas, Jorge, Mariam, Isabel, Cesar, Joshua and Aday for their time, ideas and fruitful discussions. Special thanks go to Carsten Timm for always helping me when needed and for the hospitality of his group at the TU Dresden.

Thank you to all my friends and colleagues in the Nano-Bio Spectroscopy Group, still here or already gone: Thanks to Nicole, Johanna, Quim, Marius, Jessica, Mehdi, Alison, Duncan, Livia, Alejandro(s), Andre, Hannes, Joseba, Kaike, Leonardo, Bruno, Fulvio, Stefan, Ilya, Ali, Elham, Seymur, Amilcare, Umberto, Elena, Juan, Ask, Philipp, Andrea, Lorenzo, Yann, Matteo and Victor. Without you the time would not have been the same.

Special thanks go to Cristina Garcia and Cecilia Benguria for their never-ending help with the paperwork in all those years. I would also express my thankfulness to all the proofreaders of the thesis: Roberto, Carsten, Duncan, Hannes and Ask. Thanks.

I have been lucky to have friends who made my time here in San Sebastian very enjoyable. Thanks to Nico and Fer to show me how a real Argentinian asado is done. Also thanks to my flatmates Johanna, Andre, Aina, Pablo, Arte and Cora.

Finally, I acknowledge support from MICINN (FIS2010- 21282-C02-01 and PIB2010US-00652), the Grupos Consolidados UPV/EHU del Gobierno Vasco (IT-319-07) and ACI-Promociona (ACI2009-1036), and the financial support of CONSOLIDER-INGENIO 2010 NanoTherm (CSD2010-00044), and the Ministerio de Educacion, Cultura y Deporte (FPU12/01576).

Appendix A

Derivation of the stochastic Schrödinger Equation[†]

We begin by considering a subsystem described by the Hamiltonian $\hat{H}_S$ coupled to an external environment, given by $\hat{H}_B$, through an interaction potential $\lambda\hat{W}$, the Schrödinger equation for the closed system reads ($\hbar = 1$)

$$i\partial_t|\Psi(t)\rangle = (\hat{H}_S + \hat{H}_B + \lambda\hat{W})|\Psi(t)\rangle. \tag{A.1}$$

This differential equation describes the exact dynamics of the closed system. However, the exact microscopic description of the dynamics of the macroscopic environment and its influence on the subsystem are in most cases neither feasible nor relevant. Consequently, this equation will serve as a starting point for the derivation of an equation of motion for the reduced wave function expressed in the Hilbert space of the subsystem. The following deduction is very much in the spirit of Gaspard and Nagaoka [34], who used the so-called Feshbach projection-operator method [182, 183] to derive a NMSSE.

Considering a complete and orthonormal basis for the environment,

$$\mathbb{1}_B = \sum_n |n\rangle\langle n|,\ \hat{H}_B|n\rangle = \epsilon_n|n\rangle,\ \langle m|n\rangle = \delta_{mn}, \tag{A.2}$$

[†] This appendix is part of the article *“A stochastic approach to open quantum systems”*, Topical Review in Journal of Physics Condensed Matter **24**, 273201 (2012), by R. Biele and R. D’Agosta.

the total wave function can be written as

$$|\Psi(t)\rangle = \sum_n |\phi^n(t)\rangle \otimes |n\rangle. \tag{A.3}$$

Due to the normalisation of the total wave function, $1 = \langle\Psi|\Psi\rangle = \sum_n \langle\phi^n|\phi^n\rangle$, the coefficient wave functions $|\phi^n\rangle$ are not normalised and the square of their norm can be interpreted as the probability that the environment is in the state $|n\rangle$. Consequently, the wave functions $|\phi^n\rangle$ form a statistical ensemble for the state of the total system. In order to extract a typical representative of this ensemble, we define the projection operators

$$\hat{P} \equiv \mathbb{1}_S \otimes |l\rangle\langle l|, \qquad \hat{Q} \equiv \mathbb{1}_S \otimes \sum_{n\neq l} |n\rangle\langle n|\,, \qquad \hat{P}+\hat{Q} = \mathbb{1}. \tag{A.4}$$

By applying the operator $\hat{P}$ to the total wave function, we extract the l-th coefficient wave function, $\hat{P}|\Psi\rangle = |\phi^l\rangle \otimes |l\rangle$. Correspondingly, $\hat{Q}|\Psi\rangle$ contains the information of the remaining wave functions of the ensemble. The Feshbach projection-operator method is conveniently performed in the interaction picture

$$i\partial_t|\Psi_I(t)\rangle = \lambda\hat{W}(t)|\Psi_I(t)\rangle. \tag{A.5}$$

Here, the total wave function and the potential are given by

$$|\Psi_I(t)\rangle = e^{i\hat{H}_B t}e^{i\hat{H}_S t}|\Psi(t)\rangle, \qquad \hat{W}(t) = e^{i\hat{H}_B t}e^{i\hat{H}_S t}\hat{W}e^{-i\hat{H}_S t}e^{-i\hat{H}_B t}, \tag{A.6}$$

where we have used $[\hat{H}_S, \hat{H}_B] = 0$. The idea behind the Feshbach projection method is to split the Schrödinger equation (A.5) for the closed system into two. The first contains information about the time evolution of a typical representative of the ensemble, $\hat{P}|\Psi\rangle$, while the other is a differential equation for $\hat{Q}|\Psi\rangle$, describing the time evolution of the remaining coefficients. Thus, by solving the second equation and inserting its solution into the first, one obtains a closed differential equation for $\hat{P}|\Psi\rangle$. To follow this plan, we apply the projection operators (A.4) to the time-dependent Schrödinger equation (A.5),

$$i\partial_t\hat{P}|\Psi_I(t)\rangle = \lambda\hat{P}\hat{W}(t)\hat{P}|\Psi_I(t)\rangle + \lambda\hat{P}\hat{W}(t)\hat{Q}|\Psi_I(t)\rangle, \tag{A.7}$$

$$i\partial_t\hat{Q}|\Psi_I(t)\rangle = \lambda\hat{Q}\hat{W}(t)\hat{Q}|\Psi_I(t)\rangle + \lambda\hat{Q}\hat{W}(t)\hat{P}|\Psi_I(t)\rangle. \tag{A.8}$$

The second expression is an inhomogeneous linear differential equation for $\hat{Q}|\Psi_I(t)\rangle$ and can be solved by the method of variation of constants, to get

$$\hat{Q}|\Psi_I(t)\rangle = \hat{U}(t)\hat{Q}|\Psi_I(0)\rangle - i\lambda \int_0^t \mathrm{d}t' \hat{U}(t-t')\hat{Q}\hat{W}(t')\hat{P}|\Psi_I(t')\rangle, \tag{A.9}$$

where $\hat{U}(t)$ is the time-evolution operator of the corresponding homogeneous differential equation and thus obeys $i\partial_t \hat{U}(t) = \lambda \hat{Q}\hat{W}(t)\hat{Q}\hat{U}(t)$. Inserting Eq. (A.9) into Eq. (A.7) leads to a closed differential equation for $\hat{P}|\Psi_I\rangle$,

$$\begin{aligned} i\partial_t \hat{P}|\Psi_I(t)\rangle \;=\; & \lambda \hat{P}\hat{W}(t)\hat{P}|\Psi_I(t)\rangle + \lambda \hat{P}\hat{W}(t)\Big(\hat{U}(t)\hat{Q}|\Psi_I(0)\rangle \\ & -i\lambda \int_0^t \mathrm{d}t' \hat{U}(t-t')\hat{Q}\hat{W}(t')\hat{P}|\Psi_I(t')\rangle\Big). \end{aligned} \tag{A.10}$$

It is worth mentioning that until now no approximations have been made; Eq. (A.10) describes the exact time evolution of the *l*-th coefficient of the total wave function. Hence, this can be considered as a suitable starting point for a derivation beyond the weak-coupling approximation. Unfortunately, Eq. (A.10) is as difficult to solve as the Schrödinger equation for the closed system (A.1). To make further progress we assume that the subsystem is weakly coupled to the environment and perform a perturbation expansion up to second order in the coupling parameter λ,

$$\begin{aligned} i\partial_t \hat{P}|\Psi_I(t)\rangle = \lambda \hat{P}\hat{W}(t)\hat{P}|\Psi_I(t)\rangle + \lambda \hat{P}\hat{W}(t)\hat{Q}|\Psi_I(0)\rangle - i\lambda^2 \hat{P}\hat{W}(t) \int_0^t \mathrm{d}t' \\ \times \Big(\hat{Q}\hat{W}(t')\hat{Q}|\Psi_I(0)\rangle + \hat{Q}\hat{W}(t')\hat{P}|\Psi_I(t')\rangle\Big) + \mathcal{O}(\lambda^3), \end{aligned} \tag{A.11}$$

where the time-evolution operator $\hat{U}(t)$ has been expanded to second order in λ. Until now the derivation has been quite generic, no restrictions on the interaction $\hat{W}$ or the Hamiltonians of the subsystem or environment have been imposed. In the following, we assume the interaction potential to be of linear form,

$$\hat{W} = \sum_a \hat{S}_a \otimes \hat{B}_a, \tag{A.12}$$

in the operators $\hat{S}_a$ and $\hat{B}_a$ of the subsystem and the environment, respectively. These operators can always be redefined as hermitian operators [34], thus we assume them to be so. If needed, this restriction can easily be lifted.

By multiplying (A.11) from the left with $\langle l|$ and assuming that $\langle l|\hat{B}_a(t)|l\rangle$ vanishes [*], it simplifies to

$$i\partial_t|\phi_I^l(t)\rangle = |f(t)\rangle - i\lambda^2\sum_{a,b}\hat{S}_a(t)\int_0^t \mathrm{d}t'\hat{S}_\beta(t')\langle l|\hat{B}_a(t)\hat{B}_b(t')|l\rangle|\phi_I^l(t')\rangle, \tag{A.13}$$

where the forcing term

$$|f(t)\rangle = \lambda\sum_{a,b,n\neq l}\hat{S}_a(t)\left\{\langle l|\hat{B}_a(t)|n\rangle - i\lambda\int_0^t \mathrm{d}t'\hat{S}_b(t')\langle l|\hat{B}_a(t)\hat{B}_b(t')|n\rangle\right\}|\phi_I^n(0)\rangle \tag{A.14}$$

describes the influence of all the other bath modes on the l-th coefficient wave function and one sees that the initial conditions $|\phi^n(0)\rangle$ enter here as an essential ingredient. By assuming that at $t = 0$ the subsystem is in a pure state and the bath is in thermal equilibrium, the total density operator can be written as

$$\hat{\rho}_T(0) = |\phi(0)\rangle\langle\phi(0)| \otimes \hat{\rho}_B^{\mathrm{eq}} = |\phi(0)\rangle\langle\phi(0)| \otimes \frac{e^{-\beta\hat{H}_B}}{Z_B}, \tag{A.15}$$

where β is the inverse of the temperature and $Z_B = \mathrm{Tr}_B\, e^{-\beta\hat{H}_B}$. Nevertheless, as we interested in the wave function corresponding to this density operator one assumes that the initial wave function is given by

$$|\Psi(0)\rangle = |\phi(0)\rangle \otimes \sum_n\sqrt{\frac{e^{-\beta\epsilon_n}}{Z_B}}e^{i\theta_n}|n\rangle, \tag{A.16}$$

where $\{\theta_n\}$ are independent random phases uniformly distributed over the interval $[0, 2\pi]$. Therefore, the initial conditions can be written as

$$|\phi^n(0)\rangle = \langle n|\Psi(0)\rangle = |\phi(0)\rangle\sqrt{\frac{e^{-\beta\epsilon_n}}{Z_B}}e^{i\theta_n} = |\phi^l(0)\rangle e^{-\frac{\beta}{2}(\epsilon_n-\epsilon_l)}e^{i(\theta_n-\theta_l)}, \tag{A.17}$$

where we have used the fact that all coefficient wave functions at $t = 0$ are proportional to the same state $|\phi(0)\rangle$ of the subsystem and thus they can be expressed in terms of the l-th. With the

---

[*] This condition can be either fulfilled through a redefinition of the systems Hamiltonian $\hat{H}_S$ or through the choice of the operators $\hat{B}_\alpha$.

help of this, the forcing term (A.14) can be simplified further,

$$\begin{aligned} |f(t)\rangle &\approx \lambda \sum_{a,n(\neq l)} \hat{S}_a(t)\Big\langle l\Big|\hat{B}_a(t)\Big[|\phi^l(0)\rangle \\ &\quad -i\lambda\sum_b\int_0^t \mathrm{d}t'\hat{S}_b(t')\hat{B}_b(t')|\phi^l(0)\rangle\Big]\Big|n\Big\rangle e^{-\frac{\beta}{2}(\epsilon_n-\epsilon_l)}e^{i(\theta_n-\theta_l)}, \qquad \text{(A.18)} \\ &\approx \lambda \sum_{a,n(\neq l)} \hat{S}_a(t)\langle l|\hat{B}_a(t)|n\rangle|\phi_I^l(t)e^{-\frac{\beta}{2}(\epsilon_n-\epsilon_l)}e^{i(\theta_n-\theta_l)} = \lambda\sum_a \gamma_a^l(t)\hat{S}_a(t)|\phi_I^l(t)\rangle. \qquad \text{(A.19)} \end{aligned}$$

Where we have assumed that the expression in the square brackets gives approximetely the time evolution of the l-th coefficient wave function in the interaction picture up to second order in λ for Eq. (A.13). Besides this the stochastic noise is incoorporated in

$$\gamma_a^l(t) = \sum_{n(\neq l)} \langle l|\hat{B}_a(t)|n\rangle e^{-\frac{\beta}{2}(\epsilon_n-\epsilon_l)}e^{i(\theta_n-\theta_l)}, \qquad \text{(A.20)}$$

which depends on a specific coefficient wave function. In order to eliminate this dependence, a thermal average leads to

$$\gamma_a(t) = \sum_l \frac{e^{-\frac{\beta}{2}\epsilon_l}}{\sqrt{Z_B}}\gamma_a^l(t) = \frac{1}{\sqrt{Z_B}}\sum_{l,n(\neq l)}\langle l|\hat{B}_a(t)|n\rangle e^{-\frac{\beta}{2}\epsilon_n}e^{i(\theta_n-\theta_l)}. \qquad \text{(A.21)}$$

Additionally, one needs to assume the expectation value of an operator from the bath for a typical eigenstate $|l\rangle$ is approximately equivalent to a thermal average of the temperature of the bath,

$$\langle l|\hat{B}_a(t)\hat{B}_b(t')|l\rangle \approx \mathrm{Tr}_B\left[\hat{\rho}_B^{\mathrm{eq}}\hat{B}_a(t)\hat{B}_b(t')\right] \equiv C_{ab}(t-t'). \qquad \text{(A.22)}$$

For a more complete analysis on the validity of this assumption see [184–188].

If the bath is large enough, $\gamma_a(t)$ consists of a sum of many complex oscillating terms which leads to random Gaussian behaviour according to the central limit theorem. Hence, the noise is characterised by its mean value and its variance,

$$\overline{\gamma_a(t)} = 0, \qquad \overline{\gamma_a(t)\gamma_b(t')} = 0, \qquad \overline{\gamma_a^*(t)\gamma_b(t')} = C_{ab}(t-t'), \qquad \text{(A.23)}$$

where the relations $\overline{e^{i(\theta_n+\theta_m)}} = 0$, $\overline{e^{i(\theta_n-\theta_m)}} = \delta_{nm}$ and $\langle l|\hat{B}_a(t)|l\rangle = 0$ have been used. We want to point out that the noise and the bath-correlation function are not independent, more precisely, the covariance function of the noise is given by the bath-correlation function. Collecting all the information, transforming back into the partial Schrödinger picture of the system and setting

$\tau = t - t'$, (A.13) can be written as

$$\begin{aligned} i\partial_t|\phi(t)\rangle &= \hat{H}_S|\phi(t)\rangle + \lambda\sum_a \gamma_a(t)\hat{S}_a|\phi(t)\rangle \\ &\quad -i\lambda^2\sum_{a,b}\hat{S}_a\int_0^t \mathrm{d}\tau e^{-i\hat{H}_S\tau}\hat{S}_b C_{ab}(\tau)|\phi(t-\tau)\rangle. \end{aligned} \tag{A.24}$$

Here, we have suppressed the index *l*, since we assume this wave function is a "typical representative" of the dynamics of the system. This again corresponds to the Gibbs ensemble theory: with probability close to 1, we are sure that picking at random one of the coefficient wave function, it will evolve according to (A.24).

Appendix B

Derivation of the Detailed-Balance Relation

As the SSE describes an ensemble of wave functions evolving under the influence of distinct stochastic processes, only on average one will be able to judge whether or not thermal equilibrium is reached and thus we will use the NMME for the discussion of thermal relaxation processes. As we are interested in the long-time dynamics it is sufficient to investigate thermal relaxation in the limit $t \to \infty$, where the condition

$$\lim_{t\to\infty} \frac{d\hat{\rho}_S^{\text{eq}}(t)}{dt} = 0 \tag{B.1}$$

indicates that the thermal equilibrium state, is a steady state of the dynamics. This requirement and the fact that the equilibrium density operator commutes with the system Hamiltonian leads for the NMME to

$$0 = \lim_{t\to\infty} \frac{d\hat{\rho}_S^{\text{eq}}}{dt} = \hat{K}\hat{\rho}_S^{\text{eq}}\hat{S} + \hat{S}\hat{\rho}_S^{\text{eq}}\hat{K}^\dagger - \hat{S}\hat{K}\hat{\rho}_S^{\text{eq}} - \hat{\rho}_S^{\text{eq}}\hat{K}^\dagger\hat{S} + \mathcal{O}(\lambda^4), \tag{B.2}$$

where

$$\hat{K} = \lambda^2 \int_0^\infty d\tau C(\tau) e^{-i\hat{H}_S\tau}\hat{S}e^{i\hat{H}_S\tau}. \tag{B.3}$$

From this one can obtain the conditions for relaxation processes in OQSs. Changing to the energy basis of the system,

$$\hat{H}_S|n\rangle = \epsilon_n|n\rangle, \qquad \hat{S} = \sum_{n,m} s_{nm}|n\rangle\langle m|, \tag{B.4}$$

Eq. (B.2) can be written as

$$\begin{aligned}\lim_{t\to\infty}\frac{d\hat{\rho}_S^{\mathrm{eq}}}{dt} = {} & \lambda^2 \textstyle\sum_{n,m,l} |n\rangle\langle l| s_{nm} s_{ml} \\ & \times \textstyle\int_0^\infty d\tau \Big\{ C(\tau) e^{-i(\epsilon_n-\epsilon_m)\tau} e^{-\beta\epsilon_m} + C^*(\tau) e^{-i(\epsilon_m-\epsilon_l)\tau} e^{-\beta\epsilon_m} \\ & - C(\tau) e^{-i(\epsilon_m-\epsilon_l)\tau} e^{-\beta\epsilon_l} - C^*(\tau) e^{-i(\epsilon_n-\epsilon_m)\tau} e^{-\beta\epsilon_n} \Big\} + \mathcal{O}(\lambda^4). \end{aligned} \tag{B.5}$$

As we are interested in system independent conditions for thermal relaxation, this has to be connected with the bath-correlation function

$$C(\tau) = \mathrm{Tr}_B\left[\hat{\rho}_B^{\mathrm{eq}} \hat{B}(\tau) \hat{B}(0)\right]. \tag{B.6}$$

By using the fact that $\hat{B}$ is a hermitian operator, one can conclude that

$$C^*(\tau) = C(-\tau). \tag{B.7}$$

As a result, the 'half Fourier transform' in Eq. (B.5) can be written as

$$\begin{aligned}\int_0^\infty d\tau C(\tau) e^{-i\omega\tau} &= \frac{1}{2}\int_{-\infty}^\infty d\tau C(\tau) e^{-i\omega\tau} + i\frac{1}{2i}\int_0^\infty d\tau \Big\{ C(\tau) e^{-i\omega\tau} - C^*(\tau) e^{i\omega\tau} \Big\} \\ &= \frac{1}{2}\widehat{C}(\omega) + iD(\omega), \end{aligned} \tag{B.8}$$

where $D(\omega)$ is the imaginary part of this half Fourier transform and as a consequence the Fourier transform of the bath correlation function, $\widehat{C}(\omega)$, is a real-valued function. Furthermore, if Eq. (B.8) is analytic in the upper complex half-plane of ω and vanishes faster than $|\omega|^{-1}$ as ω goes to infinity, one can apply the Kramers–Kronig relation,

$$D(\omega) = \frac{1}{2\pi} P \int_{-\infty}^{\infty} \mathrm{d}a\, \frac{\widehat{C}(a)}{\omega - a}. \tag{B.9}$$

Here, $P\int$ denotes the Cauchy principal-value integral.

In the same spirit we can simplify

$$\begin{aligned}\int_0^\infty d\tau C^*(\tau) e^{-i\omega\tau} &= \widehat{C}(-\omega) + i\frac{1}{2\pi} P \int_{-\infty}^{\infty} da \frac{\widehat{C}(-a)}{w - a} \\ &= \frac{1}{2}\widehat{C}(-\omega) + iF(\omega). \end{aligned} \tag{B.10}$$

Inserting Eqs. (B.10) and (B.8) into Eq. (B.5) we obtain

$$\begin{aligned}\lim_{t\to\infty}\frac{d\hat{\rho}_S^{\text{eq}}}{dt} &= \lambda^2\sum_{n,m,l}|n\rangle\langle l|v_{nm}v_{ml}\Big\{\Big(\frac{1}{2}\widehat{C}(\omega_{nm})+iD(\omega_{nm})\Big)e^{-\beta\epsilon_m}\\ &+\Big(\frac{1}{2}\widehat{C}(-\omega_{ml})+iF(\omega_{ml})\Big)e^{-\beta\epsilon_m}-\Big(\frac{1}{2}\widehat{C}(\omega_{ml})+iD(\omega_{ml})\Big)e^{-\beta\epsilon_l}\\ &-\Big(\frac{1}{2}\widehat{C}(-\omega_{nm})+iF(\omega_{nm})\Big)e^{-\beta\epsilon_n}\Big\}+\mathcal{O}(\lambda^4),\end{aligned} \tag{B.11}$$

where $\omega_{ij}=\epsilon_i-\epsilon_j$. We want to point out that in order to satisfy the requirement of thermal relaxation, the right-hand side of this equation has to vanish. In addition, the Fourier transform of the bath-correlation function can be interpreted as the power spectrum of the noise and hence describes the probabilities for energy transitions in the system. By assuming that this power spectrum satisfies a so-called detailed-balance relation,

$$\widehat{C}(-\omega)=e^{\beta\omega}\widehat{C}(\omega), \tag{B.12}$$

(B.11) simplifies to

$$\begin{aligned}\lim_{t\to\infty}\frac{d\hat{\rho}_S^{\text{eq}}}{dt} &= i\lambda^2\sum_{n,m,l}|n\rangle\langle l|s_{nm}s_{ml}\Big\{D(\omega_{nm})e^{-\beta\epsilon_m}+F(\omega_{ml})e^{-\beta\epsilon_m}\\ &-D(\omega_{ml})e^{-\beta\epsilon_l}-F(\omega_{nm})e^{-\beta\epsilon_n}\Big\}+\mathcal{O}(\lambda^4).\end{aligned} \tag{B.13}$$

The detailed-balance relation (B.12) ensures that the energy transitions in the system are balanced according sto Boltzmann factors. Furthermore, we want to point out that Eq. (B.13) has only imaginary components and by inserting the explicit integrals into it we arrive at

$$\begin{aligned}\lim_{t\to\infty}\frac{d\hat{\rho}_S^{\text{eq}}}{dt} &= \frac{i\lambda^2}{2\pi}\sum_{n,m,l}|n\rangle\langle l|s_{nm}s_{ml}\int_{-\infty}^{\infty}da\Big\{\frac{\widehat{C}(a)\big(1-e^{-\beta(\epsilon_n-\epsilon_m-a)}\big)e^{-\beta\epsilon_m}}{\omega_{mn}-a}\\ &-\frac{\widehat{C}(a)\big(1-e^{-\beta(\epsilon_m-\epsilon_l-a)}\big)e^{-\beta\epsilon_l}}{\omega_{ml}-a}\Big\}+\mathcal{O}(\lambda^4).\end{aligned} \tag{B.14}$$

In this expression there is no need to write the principal value anymore as the integral is no longer singular. It can be shown that the diagonal components of the former equation cancel each other, i.e.,

$$\langle l|\frac{d\hat{\rho}_S^{\text{eq}}}{dt}|l\rangle=0. \tag{B.15}$$

This can be done by changing ω_{mn} to $-\omega_{mn}$, changing the integration variable in the second integral of (B.14) from a to $-a$, and applying the detailed-balance relation another time.

As a result, one can conclude that the NMSSE (2.6) has a stationary solution which coincides with the thermal-equilibrium state up to first order in λ. Furthermore, if the detailed-balance relation is satisfied, the corresponding master equation or SSE drives the system towards a stationary state that coincides in the diagonal elements in the energy basis with the thermal-equilibrium state up to fourth order. Additionally, when neglecting either the off-diagonal components of the density matrix in the long-time behaviour or the imaginary contribution of the half Fourier transform,

$$\mathrm{Im}\left[\int_0^\infty d\tau C(\tau)e^{-i\omega\tau}\right] = D(\omega) \approx 0, \tag{B.16}$$

the thermal equilibrium states is a stationary solution of the equation of motion up to fourth order. It can be argued that this imaginary part can be included in the system Hamiltonian [31], the so-called Lamb shift. One the one hand, the equilibrium density operator will not commute with this effective Hamiltonian, nevertheless, this energy shift will not introduce dissipative dynamics in the system [32].

Appendix C

Angular Dependent Transmittance of TiS_3

Figure C.1 shows that the polar dependence of the transmittance (nanoribbons) follows subsequent rotations of the sample. The minimum of the transmittance is found to correspond with the *b*-axis. As the sample is rotated, the corresponding polar dependences rotates as well.

Figure C.2 (a–d) shows the angular dependence of the transmittance for decreasing thicknesses of nanosheet samples. The linear dichroism becomes weaker for thinner samples. This can be directly appreciated in Fig. C.2 (e) where we plot the ratio of the maximum and minimum transmittance as a function of the minimum transmittance (thickness). The ratio decreases for thinner samples.

Figure C.3 shows polar plots of the transmittance as a function of excitation angle for samples of TiS_3, BP, and MoS_2 having comparable overall transmittance. It can be seen that the TiS_3 sample has the strongest modulation of the transmittance with a *b*-axis to *a*-axis ratio of 30 compared with a ratio of 1.4 for BP. MoS_2 shows little modulation as expected.

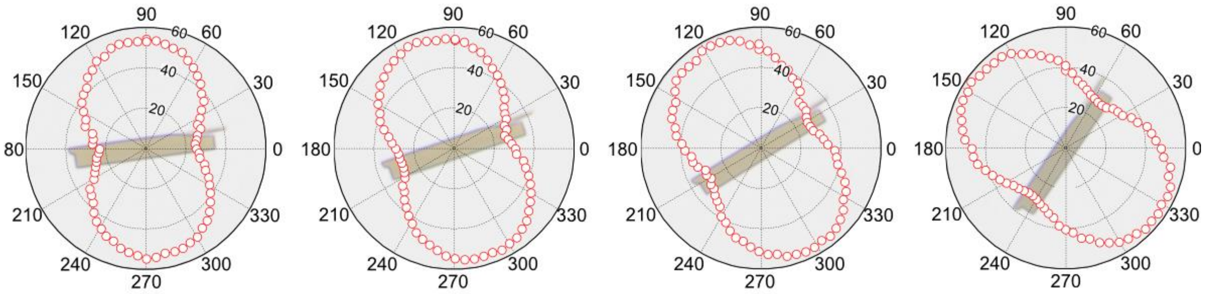

FIGURE C.1: Transmittance as a function of the excitation polarization angle for a TiS_3 wide ribbon, rotated at different angles. The angular dependence of the transmittance follows the rotation of the flake.

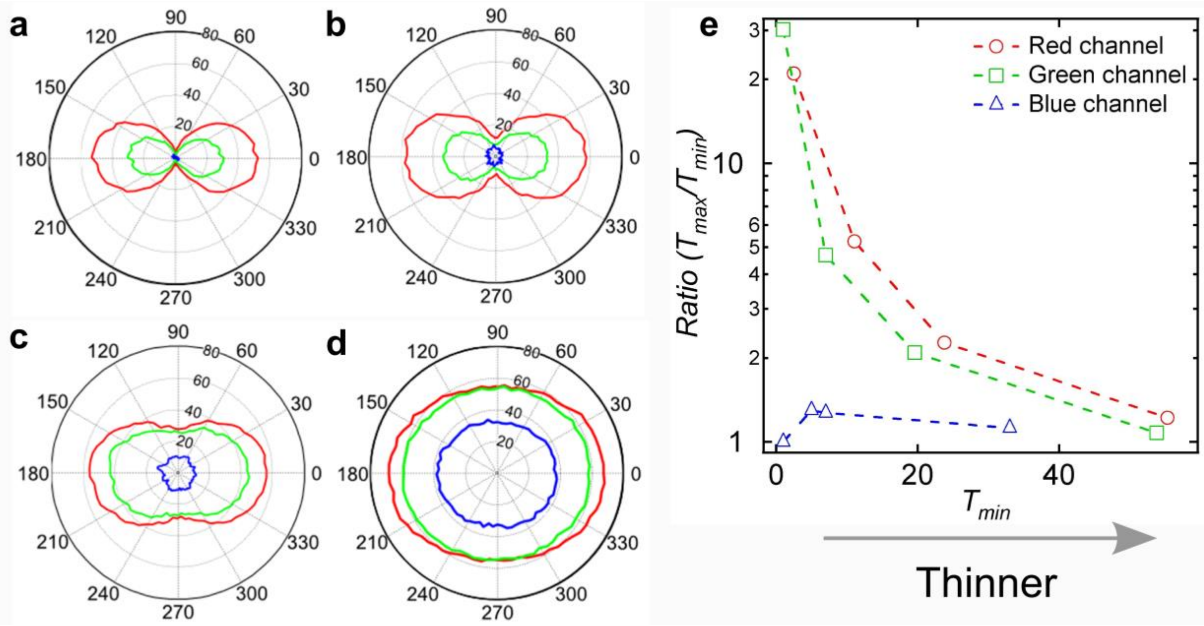

FIGURE C.2: Transmittance measured from the red, green and blue channel of the camera, measured for TiS_3 samples with different thicknesses (from thicker to thinner).

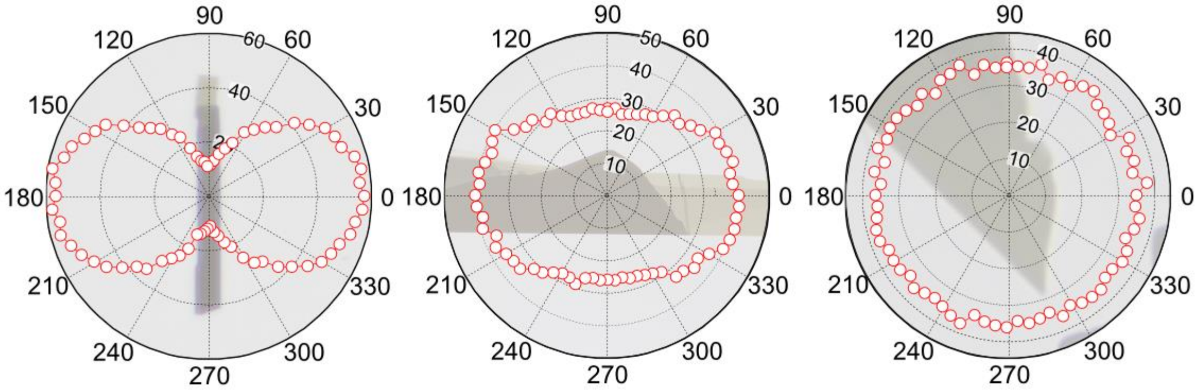

FIGURE C.3: Comparison between the angular dependent transmittance of TiS_3 (left), BP (middle) and MoS_2 (right).

Bibliography

[1] H. Vazquez, R. Skouta, S. Schneebeli, M. Kamenetska, R. Breslow, and L. Venkataraman, “Probing the conductance superposition law in single-molecule circuits with parallel paths,” Nat. Nanotechnol. **7**, 663–667 (2012).

[2] A. W. Chin, S. F. Huelga, and M. Plenio, “Coherence and decoherence in biological systems: principles of noise-assisted transport and the origin of long-lived coherences,” Phil. Trans. R. Soc. A **370**, 3638–3657 (2012).

[3] Y. Dubi, “Interplay between Dephasing and Geometry and Directed Heat Flow in Exciton Transfer Complexes,” J. Phys. Chem. C **119**, 25252–25259 (2015).

[4] J. K. Pachos, *Introduction to Topological Quantum Computation* (Cambridge University Press, 2012).

[5] S. Bravyi and J. Haah, “Quantum self-correction in the 3D cubic code model,” Phys. Rev. Lett. **111**, 200501 (2013).

[6] C. J. Muller, J. M. van Ruitenbeek, and L. J. de Jongh, “Experimental observation of the transition from weak link to tunnel junction,” Phys. C **191**, 485 (1992).

[7] M. Di Ventra, S. Evoy, and J. R. J. Helfin, eds., *Introduction to Nanoscale Science and Technology* (Kluwer Academic Publisher, 2004).

[8] A. Majumdar, “Thermoelectricity in Semiconductor Nanostructures,” Science **303**, 777 (2004).

[9] L. E. Bell, “Cooling, heating, generating power, and recovering waste heat with thermoelectric systems,” Science **321**, 1457 (2008).

[10] F. Giazotto, T. T. Heikkilä, A. Luukanen, A. M. Savin, and J. P. Pekola, “Opportunities for mesoscopics in thermometry and refrigeration : Physics and applications,” Rev. Mod. Phys. **78**, 217–274 (2006).

[11] B. Li, L. Wang, and G. Casati, “Negative differential thermal resistance and thermal transistor,” Appl. Phys. Lett. **88**, 143501 (2006).

[12] D. Segal and A. Nitzan, “Spin-Boson Thermal Rectifier,” Phys. Rev. Lett. **94**, 034301 (2005).

[13] M. Terraneo, M. Peyrard, and G. Casati, “Controlling the Energy Flow in Nonlinear Lattices : A Model for a Thermal Rectifier,” Phys. Rev. Lett. **88**, 094302 (2002).

[14] J.-S. Wang, J. Wang, and J. T. Lü, “Quantum thermal transport in nanostructures,” Eur. Phys. J. B **62**, 381–404 (2008).

[15] L. Wang and B. Li, “Thermal Logic Gates: Computation with Phonons,” Phys. Rev. Lett. **99**, 177208 (2007).

[16] E. T. Whittaker, *A history of the theories of aether and electricity from the age of Descartes to the close of the nineteenth century*, 2nd ed. (Thomas Nelson and Sons Ltd., 1951).

[17] P. L. Knight and L. Allen, *Concepts of Quantum Optics* (Pergamon Press Ltd., 1983) p. 226.

[18] J. C. Maxwell, “A Dynamical Theory of the Electromagnetic Field,” Philos. Trans. R. Soc. London **155**, 459–512 (1865).

[19] H. Hertz, “Ueber einen Einfluss des ultravioletten Lichtes auf die electrische Entladung,” Ann. der Phys. und Chemie **267**, 983–1000 (1887).

[20] A. Einstein, “Über einen die Erzeugung und Verwandlung des Lichtes betreffenden heuristischen Gesichtspunkt,” Ann. Phys. **322**, 132–148 (1905).

[21] A. P. French, *Einstein: A Centenary Volume* (Harvard University Press, 1979) p. 352.

[22] W. H. Zurek, “Decoherence and the transition from quantum to classical – REVISITED,” (2003), arXiv:0306072 [quant-ph] .

[23] P. Rebentrost, M. Mohseni, I. Kassal, S. Lloyd, and A. Aspuru-Guzik, “Environment-assisted quantum transport,” New J. Phys. **11**, 033003 (2009).

[24] W. Kohn, “Nobel Lecture : Electronic structure of matter wave functions and density functionals,” Rev. Mod. Phys. **71**, 1253–1266 (1999).

[25] L. Britnell, R. M. Ribeiro, A. Eckmann, R. Jalil, B. D. Belle, A. Mishchenko, Y. Kim, R. V. Gorbachev, T. Georgiou, S. V. Morozov, A. N. Grigorenko, A. K. Geim, C. Casiraghi, A. H. C. Neto, and K. S. Novoselov, “Strong Light-Matter Interactions Thin Films,” Sciene **340**, 1311–1314 (2013).

[26] K. F. Mak, C. Lee, J. Hone, J. Shan, and T. F. Heinz, “Atomically Thin MoS_2: A New Direct-Gap Semiconductor,” Phys. Rev. Lett. **105**, 136805 (2010).

[27] J. Pu, Y. Yomogida, K.-k. Liu, L.-J. Li, Y. Iwasa, and T. Takenobu, “Highly Flexible MoS_2 Thin-Film Transistors with Ion Gel Dielectrics,” Nano Lett. **12**, 4013–4017 (2012).

[28] G.-H. Lee, Y.-J. Yu, X. Cui, N. Petrone, C.-H. Lee, S. Choi, D.-Y. Lee, C. Lee, W. J. Yoo, K. Watanabe, T. Taniguchi, C. Nuckolls, P. Kim, and J. Hone, “Flexible and Transparent MoS_2 Field-Effect Transistors on Hexagonal Boron Nitride-Graphene Heterostructures,” ACS Nano **7**, 7931–7936 (2013).

[29] H.-P. Breuer and F. Petruccione, *Lect. Notes Phys.*, Vol. 622 (Springer, 2003).

[30] C. W. Gardiner and P. Zoller, *Quantum Noise*, 2nd ed. (Springer, Berlin, 2000).

[31] U. Weiss, *Quantum Dissipative Systems*, 3rd ed. (World Scientific, Singapore, 2007).

[32] H.-P. Breuer and F. Petruccione, *The Theory of Open Quantum Systems* (Oxford University Press, 2002).

[33] P. Gaspard and M. Nagaoka, “Non-Markovian stochastic Schrödinger equation,” J. Chem. Phys. **111**, 5676–5690 (1999).

[34] P. Gaspard and M. Nagaoka, “Slippage of initial conditions for the Redfield master equation,” J. Chem. Phys. **111**, 5668 (1999).

[35] P. E. Kloeden and E. Platen, *Numerical Solution of Stochastic Differential Equations* (Springer, 1999).

[36] H.-P. Breuer, U. Dorner, and F. Petruccione, “Numerical integration methods for stochastic wave function equations,” Comput. Phys. Commun. **132**, 30–43 (2000).

[37] P. E. Protter, *Stochastic Integration and Differential equations*, 2nd ed. (Springer, 2004) p. 415.

[38] R. F. Fox, “Stochastic calculus in physics,” J. Stat. Phys. **46**, 1145–1157 (1987).

[39] C. W. Gardiner, *Am. Nat.*, 3rd ed. (Springer, Berlin, 2004).

[40] N. van Kampen, *Stochastic Processes in Physics and Chemistry* (Elsevier, 2007).

[41] G. Lindblad, “On the Generators of Quantum Dynamical Semigroups,” Comm. Math. Phys. **48**, 119–130 (1976).

[42] R. Feynman, *Statistical Mechanics: A Set of Lectures*, 2nd ed. (Westview Press, 1998).

[43] K. Huang, *Introduction to Statistical Physics*, 2nd ed. (Taylor and Francis, London, 2001).

[44] R. Biele, *Stochastic Approaches to Thermal Relaxation of Open Quantum Systems* (2012).

[45] W. Schleich, *Quantum Optics in Phase Space* (Wiley, 2001).

[46] W. T. Strunz and T. Yu, “Convolutionless Non-Markovian master equations and quantum trajectories: Brownian motion,” Phys. Rev. A **69**, 52115 (2004).

[47] I. de Vega, D. Alonso, and P. Gaspard, “Two-level system immersed in a photonic band-gap material: A non-Markovian stochastic Schrödinger-equation approach,” Phys. Rev. A **71**, 23812 (2005).

[48] I. de Vega, D. Alonso, P. Gaspard, and W. T. Strunz, “Non-Markovian stochastic Schrödinger equations in different temperature regimes: a study of the spin-boson model.” J. Chem. Phys. **122**, 124106 (2005).

[49] C. Timm, “Time-convolutionless master equation for quantum dots: Perturbative expansion to arbitrary order,” Phys. Rev. B **83**, 115416 (2011).

[50] R. Biele, C. Timm, and R. D’Agosta, “Application of a time-convolutionless stochastic Schrödinger equation to energy transport and thermal relaxation.” J. Phys. Condens. Matter **26**, 395303 (2014).

[51] W. H. Press, S. A. Teukolsky, W. T. Vetterling, and B. P. Flannery, *Numerical recipes in Fortran 77: the art of scientific computing* (Cambridge University Press, Cambridge, 2001).

[52] P. E. Kloeden, E. Platen, and H. Schurz, *Numerical Solution of SDE Through Computer Experiments*, 3rd ed. (Springer, Berlin, 1997).

[53] H. Wichterich, M. Henrich, H.-P. Breuer, J. Gemmer, and M. Michel, “Modeling heat transport through completely positive maps,” Phys. Rev. E **76**, 31115 (2007).

[54] C. Mejia-Monasterio and H. Wichterich, “Heat transport in quantum spin chains,” Eur. Phys. J. Spec. Top. **151**, 113–125 (2007).

[55] Y. Dubi and M. Di Ventra, “Thermoelectric effects in nanoscale junctions.” Nano Lett. **9**, 97–101 (2009).

[56] C. W. Chang, D. Okawa, H. Garcia, A. Majumdar, and A. Zettl, “Breakdown of Fourier’s law in nanotube thermal conductors,” Phys. Rev. Lett. **101**, 075903 (2008).

[57] Y. Dubi and M. Di Ventra, “Reconstructing Fourier’s law from disorder in quantum wires,” Phys. Rev. B - Condens. Matter Mater. Phys. **79**, 115415 (2009).

[58] Y. Dubi and M. Di Ventra, “Fourier’s law: Insight from a simple derivation,” Phys. Rev. E **79** (2009), 10.1103/PhysRevE.79.042101.

[59] J. M. Luttinger, “Theory of Thermal Transport Coefficients,” Phys. Rev. **135**, A1505 (1964).

[60] F. G. Eich, M. Di Ventra, and G. Vignale, “Density-functional theory of thermoelectric phenomena,” Phys. Rev. Lett. **112**, 196401 (2014).

[61] F. G. Eich, A. Principi, M. Di Ventra, and G. Vignale, “Luttinger-field approach to thermoelectric transport in nanoscale conductors,” Phys. Rev. B **90**, 115116 (2014).

[62] M. A. L. Marques, C. A. Ullrich, A. Rubio, F. Nogueira, K. Burke, and E. K. U. Gross, eds., *Time-Dependent Density Functional Theory*, Lecture notes in Physics, Vol. 706 (Springer, Berlin, 2006).

[63] C. Ullrich, *Time Dependent Density Functional Theory: Concepts and Applications* (Oxford University Press, Oxford, 2012).

[64] G. Giuliani and G. Vignale, *Quantum theory electron Liq.* (Cambridge University Press, 2005).

[65] P. Hänggi and M. Borkovec, “Reaction-rate theory: fifty years after Kramers,” Rev. Mod. Phys. **62**, 251–341 (1990).

[66] G. Kirchhoff, “On the relation between the radiating and absorbing powers of different bodies for light and heat,” Ann. Phys. **109**, 275 (1860).

[67] M. Planck, “Über das Gesetz der Energieverteilung im Normalspectrum,” Ann. Phys. **4**, 553–563 (1901).

[68] M. Planck, “Entropie und Temperatur strahlender Wärme,” Ann. Phys. **1**, 719–737 (1900).

[69] K. A. Velizhanin, H. Wang, and M. Thoss, “Heat transport through model molecular junctions: A multilayer multiconfiguration time-dependent Hartree approach,” Chem. Phys. Lett. **460**, 325–330 (2008).

[70] A. Donges, “The coherence length of black-body radiation,” Eur. J. Phys. **19**, 245–249 (1998).

[71] D. C. Bertilone, “On the cross-spectral tensors for black-body emission into space,” J. Mod. Opt. **43**, 207 (1996).

[72] R. Biele and R. D’Agosta, “A stochastic approach to open quantum systems.” J. Phys. Condens. Matter **24**, 273201 (2012).

[73] R. Biele, R. D’Agosta, and A. Rubio, “Time-Dependent Thermal Transport Theory,” Phys. Rev. Lett. **115**, 056801 (2015).

[74] C. A. Rodríguez-Rosario, T. Frauenheim, and A. Aspuru-Guzik, “Thermodynamics of quantum coherence,” (2013), arXiv:1308.1245 .

[75] L.-A. Wu and D. Segal, “Energy flux operator, current conservation and the formal Fourier’s law,” J. Phys. A Math. Theor. **42**, 025302 (2009).

[76] P. Reimann, M. Grifoni, and P. Hänggi, “Quantum Ratchets,” Phys. Rev. Lett. **79**, 10–13 (1997).

[77] F. Zhan, N. Li, S. Kohler, and P. Hänggi, “Molecular wires acting as quantum heat ratchets,” Phys. Rev. E **80**, 061115 (2009).

[78] J. Lehmann, S. Kohler, P. Hänggi, and A. Nitzan, “Molecular Wires Acting as Coherent Quantum Ratchets,” Phys. Rev. Lett. **88**, 228305 (2002).

[79] P. Hänggi and F. Marchesoni, “Artificial Brownian motors: Controlling transport on the nanoscale,” Rev. Mod. Phys. **81**, 387–442 (2009).

[80] C. Drexler, S. A. Tarasenko, P. Olbrich, J. Karch, M. Hirmer, F. Müller, M. Gmitra, J. Fabian, R. Yakimova, S. Lara-Avila, S. Kubatkin, M. Wang, R. Vajtai, P. M. Ajayan,

J. Kono, and S. D. Ganichev, “Magnetic quantum ratchet effect in graphene,” Nat. Nanotechnol. **8**, 104–107 (2013).

[81] T. Salger, S. Kling, T. Hecking, C. Geckeler, L. Morales-Molina, and M. Weitz, “Directed Transport of Atoms in a Hamiltonian Quantum Ratchet,” Science **326**, 1241–1243 (2009).

[82] A. Nitzan and M. A. Ratner, “Electron Transport in Molecular Wire Junctions,” Science **300**, 1384–1389 (2003).

[83] I. Prigogine, “Time, Structure, and Fluctuations,” Science **201**, 777–785 (1978).

[84] I. Prigogine, I. Stengers, and A. Toffler, *Order Out of Chaos: Man’s New Dialogue with Nature* (Bantam New Age Books, 1984).

[85] D. Rai, O. Hod, and A. Nitzan, “Circular Currents in Molecular Wires ,” J. Phys. Chem. C **114**, 20583–20594 (2010).

[86] A. K. Geim and I. V. Grigorieva, “Van der Waals heterostructures,” Nature **499**, 419–425 (2013).

[87] W. J. Yu, Z. Li, H. Zhou, C. Y., Y. Wang, Y. Huang, and X. Duan, “Vertically stacked multi-heterostructures of layered materials for logic transistors and complementary inverters,” Nat. Mater. **12**, 246–252 (2012).

[88] S. Lebègue, T. Björkman, M. Klintenberg, R. M. Nieminen, and O. Eriksson, “Two-Dimensional Materials from Data Filtering and Ab Initio Calculations,” Phys. Rev. X **3**, 031002 (2013).

[89] K. Endo, H. Ihara, K. Watanabe, and S.-I. Gonda, “XPS study on valence band structures of transition-metal trisulfides, TiS_3, NbS_3, and TaS_3,” J. Solid State Chem. **39**, 215–218 (1981).

[90] J. O. Island, M. Buscema, M. Barawi, J. M. Clamagirand, J. R. Ares, C. Sánchez, I. J. Ferrer, G. A. Steele, H. S. J. van der Zant, and A. Castellanos-Gomez, “Ultrahigh Photoresponse of Few-Layer TiS_3 Nanoribbon Transistors,” Adv. Opt. Mater. **2**, 641 (2014).

[91] J. O. Island, M. Barawi, R. Biele, A. Almazán, J. M. Clamagirand, J. R. Ares, C. Sánchez, H. S. J. van der Zant, J. V. Álvarez, R. D’Agosta, I. J. Ferrer, and A. Castellanos-Gomez, “TiS_3 Transistors with Tailored Morphology and Electrical Properties,” Adv. Mater. **27**, 2595 (2015).

[92] A. J. Molina-Mendoza, M. Barawi, R. Biele, E. Flores, J. R. Ares, C. Sánchez, G. Rubio-Bollinger, N. Agraït, R. D'Agosta, I. J. Ferrer, and A. Castellanos-Gomez, "Electronic Bandgap and Exciton Binding Energy of Layered Semiconductor TiS_3," Adv. Electron. Mater. **1**, 1500126 (2015).

[93] J. Wu, D. Wang, H. Liu, W.-M. Lau, and L.-M. Liu, "An ab initio study of TiS_3: a promising electrode material for rechargeable Li and Na ion batteries," RSC Adv. **5**, 21455–21463 (2015).

[94] M. Barawi, I. J. Ferrer, J. R. Ares, and C. Sánchez, "Hydrogen evolution using palladium sulfide (PdS) nanocorals as photoanodes in aqueous solution," ACS Appl. Mater. Interfaces **6**, 20544 (2014).

[95] Y. Jin, X. Li, and J. Yang, "Single layer of MX_3 (M = Ti, Zr; X = S, Se, Te): a new platform for nano-electronics and optics," Phys. Chem. Chem. Phys. **17**, 18665–18669 (2015).

[96] I. G. Gorlova, S. G. Zybtsev, V. Pokrovskii, N. B. Bolotina, I. A. Verin, and A. N. Titov, "Nonlinear conductivity of quasi-one-dimensional layered compound TiS_3," Phys. B Condens. Matter **407**, 1707–1710 (2012).

[97] J. Dai and X. C. Zeng, "Titanium Trisulfide Monolayer: Theoretical Prediction of a New Direct-Gap Semiconductor with High and Anisotropic Carrier Mobility," Angew. Chemie Int. Ed. **54**, 7572–7576 (2015).

[98] A. Marini, C. Hogan, M. Grüning, and D. Varsano, "yambo: An ab initio tool for excited state calculations," Comput. Phys. Commun. **180**, 1392 (2009).

[99] P. Giannozzi, S. Baroni, N. Bonini, M. Calandra, R. Car, C. Cavazzoni, D. Ceresoli, G. L. Chiarotti, M. Cococcioni, I. Dabo, A. Dal Corso, S. de Gironcoli, S. Fabris, G. Fratesi, R. Gebauer, U. Gerstmann, C. Gougoussis, A. Kokalj, M. Lazzeri, L. Martin-Samos, N. Marzari, F. Mauri, R. Mazzarello, S. Paolini, A. Pasquarello, L. Paulatto, C. Sbraccia, S. Scandolo, G. Sclauzero, A. P. Seitsonen, A. Smogunov, P. Umari, and R. M. Wentzcovitch, "QUANTUM ESPRESSO: a modular and open-source software project for quantum simulations of materials," J. Phys. Condens. Matter **21**, 395502 (2009).

[100] P. Hohenberg and W. Kohn, "Inhomogeneous Electron Gas," Phys. Rev. **136**, B864–B871 (1964).

[101] W. Kohn and L. J. Sham, "Self-Consistent Equations Including Exchange and Correlation Effects," Phys. Rev. **140**, A1133 (1965).

[102] M. Levy, J. P. Perdew, and V. Sahni, "Exact differential equation for the density and ionization energy of a many-particle system," Phys. Rev. A **30**, 2745–2748 (1984).

[103] C.-O. Almbladh and U. von Barth, "Exact results for the charge and spin densities, exchange-correlation potentials, and density-functional eigenvalues," Phys. Rev. B **31**, 3231–3244 (1985).

[104] L. Fetter and J. D. Walecka, *Quantum theory of many-body systems* (McGraw Hill, New York, 1981).

[105] E. K. U. Gross, E. Runge, and O. Heinonen, *Many-particle theory* (Adam-Hilger, Bristol, 1991).

[106] G. Mahan, *Many-Particle Physics* (Plenum, New York, 1981).

[107] G. Strinati, "Application of the Green's Functions Method to the Study of the Optical Properties of Semiconductors ." La Riv. del Nuovo Cim. **11** (1988).

[108] G. Onida, L. Reining, and A. Rubio, "Electronic excitations : density-functional versus many-body Green's-function approaches," Rev. Mod. Phys. **74**, 601 (2002).

[109] R. D. Mattuck, *A Guide to Feynman Diagrams in the Many Body Problem*, 2nd ed. (Dover Publications, New York, 1992).

[110] G. Stefanucci and R. van Leeuwen, *Non-equilibrium many-body theory of quantum systems* (Cambridge University Press, New York, 2013).

[111] L. Hedin, "New Method for Calculating the One-Particle Green's Function with Application to the Electron-Gas Problem," Phys. Rev. **139**, A796 (1965).

[112] F. Aryasetiawan and O. Gunnarsson, "The GW method," Rep. Prog. Phys. **61**, 237 (1998).

[113] F. Brosens, J. T. Devreese, and L. Lemmens, "Dielectric function of the electron gas with dynamical-exchange decoupling. II. Discussion and results," Phys. Rev. B **21**, 1363 (1980).

[114] W. G. Aulbur, M. Städele, and A. Görling, "Exact-exchange-based quasiparticle calculations," Phys. Rev. B **62**, 7121 (2000).

[115] D. Varsano, R. D. Felice, M. A. L. Marques, and A. Rubio, "A TDDFT Study of the Excited States of DNA Bases and Their Assemblies," J. Phys. Chem. B **110**, 7129–7138 (2006).

[116] M. S. Hybertsen and S. G. Louie, “Electron correlation in semiconductors and insulators: Band gaps and quasiparticle energies correlation,” Phys. Rev. B **34**, 5390 (1986).

[117] R. W. Godby, M. Schlüter, and L. J. Sham, “Accurate Exchange-Correlation Potential for Silicon and Its Discontinuity on Addition of an Electron,” Phys. Rev. Lett. **56**, 2415 (1986).

[118] A. Rubio, J. L. Corkill, M. L. Cohen, E. L. Shirley, and S. G. Louie, “Quasiparticle band structure of AlN and GaN,” Phys. Rev. B **48**, 11810 (1993).

[119] E. E. Salpeter and H. A. Bethe, “A Relativistic Equation for Bound-State Problems,” Phys. Rev. **84**, 1232 (1951).

[120] G. Onida, L. Reining, and A. Rubio, “Electronic excitations: density-functional versus many-body Green’s-function approaches,” Rev. Mod. Phys. **74**, 601–654 (2002).

[121] J. L. Murray, “The S-Ti (Sulfur-Titanium) system,” Bull. Alloy Phase Diagrams **7**, 156–163 (1986).

[122] J. C. Mikkelsen, “P-T-X phase diagram for Ti-S from (60-75) atomic sulfur,” Nuovo Cim. B **38**, 378–386 (1977).

[123] K. K. Liu, W. Zhang, Y. H. Lee, Y. C. Lin, M. T. Chang, C. Y. Su, C. S. Chang, H. Li, Y. Shi, H. Zhang, C. S. Lai, and L. J. Li, “Growth of large-area and highly crystalline MoS_2 thin layers on insulating substrates,” Nano Lett. **12**, 1538–1544 (2012).

[124] C.-P. Lu, G. Li, J. Mao, L.-M. Wang, and E. Y. Andrei, “Bandgap, Mid-Gap States, and Gating Effects in MoS_2,” Nano Lett. **14**, 4628 (2014).

[125] B. H. Kim, M. Park, M. Lee, S. J. Baek, H. Y. Jeong, M. Choi, S. J. Chang, W. G. Hong, T. K. Kim, H. R. Moon, Y. W. Park, N. Park, and Y. Jun, “Effect of sulphur vacancy on geometric and electronic structure of MoS_2 induced by molecular hydrogen treatment at room temperature,” RSC Adv. **3**, 18424 (2013).

[126] W. Zhou, X. Zou, S. Najmaei, Z. Liu, Y. Shi, J. Kong, J. Lou, P. M. Ajayan, B. I. Yakobson, and J. C. Idrobo, “Intrinsic structural defects in monolayer molybdenum disulfide,” Nano Lett. **13**, 2615–2622 (2013).

[127] W. Setyawan and S. Curtarolo, “High-throughput electronic band structure calculations: Challenges and tools,” Comput. Mater. Sci. **49**, 299–312 (2010).

[128] F. Iyikanat, H. Sahin, R. T. Senger, and F. M. Peeters, “Vacancy Formation and Oxidation Characteristics of Single Layer TiS_3,” J. Phys. Chem. C **119**, 10709–10715 (2015).

[129] J. Kang, H. Sahin, H. D. Ozaydin, R. T. Senger, and F. M. Peeters, “TiS_3 nanoribbons: Width-independent band gap and strain-tunable electronic properties,” Phys. Rev. B **92**, 75413 (2015).

[130] A. Castellanos-Gomez, R. Roldán, E. Cappelluti, M. Buscema, F. Guinea, H. S. J. van der Zant, and G. A. Steele, “Local Strain Engineering in Atomically Thin MoS_2,” Nano Lett. **13**, 5361–5366 (2013).

[131] S. Yang, C. Wang, H. Sahin, H. Chen, Y. Li, S.-S. Li, A. Suslu, F. M. Peeters, Q. Liu, J. Li, and S. Tongay, “Tuning the Optical, Magnetic, and Electrical Properties of $ReSe_2$ by Nanoscale Strain Engineering,” Nano Lett. **15**, 1660–1666 (2015).

[132] H. Mei, C. M. Landis, and R. Huang, “Concomitant wrinkling and buckle-delamination of elastic thin films on compliant substrates,” Mech. Mater. **43**, 627–642 (2011).

[133] D. Vella, J. Bico, A. Boudaoud, B. Roman, and P. M. Reis, “The macroscopic delamination of thin films from elastic substrates.” Proc. Natl. Acad. Sci. **106**, 10901–10906 (2009).

[134] A. Castellanos-Gomez, J. Quereda, H. P. van der Meulen, N. Agraït, and G. Rubio-Bollinger, “Spatially resolved optical absorption spectroscopy of single-and few-layer MoS_2 by hyperspectral imaging,” Nanotechnology **27**, 115705 (2016).

[135] I. J. Ferrer, J. R. Ares, J. M. Clamagirand, M. Barawi, and C. Sánchez, “Optical properties of titanium trisulphide (TiS_3) thin films,” Thin Solid Films **535**, 398–401 (2013).

[136] C. Hartwigsen, S. Goedecker, and J. Hutter, “Relativistic separable dual-space Gaussian pseudopotentials from H to Rn,” Phys. Rev. B **58**, 3641–3662 (1998).

[137] S. Goedecker, M. Teter, and J. Hutter, “Separable dual-space Gaussian pseudopotentials,” Phys. Rev. B **54**, 1703–1710 (1996).

[138] S. Furuseth, L. Brattas, and A. Kjejshus, “On the crystal structures of TiS_3, ZrS_3, $ZrSe_3$, $ZrTe_3$, HfS_3, and $HfSe_3$,” Acta Chem. Scand. **29**, 623 (1975).

[139] M. Abdulsalam and D. P. Joubert, “Structural and electronic properties of MX_3 (M = Ti, Zr and Hf; X = S, Se, Te) from first principles calculations,” Eur. Phys. J. B **88**, 177 (2015).

[140] M. Li, J. Dai, and X. C. Zeng, “Tuning Electronic Properties of Transition-Metal Trichalcogenides via Tensile Strain,” Nanoscale , (accepted) (2015).

[141] K. S. Novoselov, D. Jiang, F. Schedin, T. J. Booth, V. V. Khotkevich, S. V. Morozov, and A. K. Geim, "Two-dimensional atomic crystals." Proc. Natl. Acad. Sci. U. S. A. **102**, 10451–10453 (2005).

[142] S. Z. Butler, S. M. Hollen, and L. Cao, "Opportunities in Two-Dimensional Materials Beyond Graphene," ACS Nano **7**, 2898–2926 (2013).

[143] F. Schwierz, "Graphene transistors," Nat. Nanotechnol. **5**, 487–96 (2010).

[144] B. Radisavljevic, A. Radenovic, J. Brivio, V. Giacometti, and A. Kis, "Single-layer MoS_2 transistors," Nat. Nanotechnol. **6**, 147–150 (2011).

[145] A. Meerschaut and J. Rouxel, "Pseudo-One-Dimensional MX_3 and MX_4 Transition Metal Chalcogenides," in *Phys. Chem. Mater. with Low-Dimensional Struct.* (Springer, 1986) pp. 205 –279.

[146] J. O. Island, R. Biele, M. Barawi, J. M. Clamagirand, J. R. Ares, C. Sánchez, H. S. J. van der Zant, I. J. Ferrer, R. D'Agosta, and A. Castellanos-Gomez, "Titanium trisulfide (TiS_3): a 2D semiconductor with quasi-1D optical and electronic properties," Sci. Rep. **6**, 22214 (2016).

[147] P. Nozières and D. Pines, "Electron interaction in solids. General formulation," Phys. Rev. **109**, 741–761 (1958).

[148] H. Ehrenreich and M. H. Cohen, "Self-consistent field approach to the many-electron problem," Phys. Rev. **115**, 786–790 (1959).

[149] W. von der Linden and P. Horsch, "Precise quasiparticle energies and Hartree-Fock bands of semiconductors and insulators," Phys. Rev. B **37**, 8351–8362 (1988).

[150] G. E. Engel and B. Farid, "Generalized plasmon-pole model and plasmon band structures of crystals," Phys. Rev. B **47**, 15931–15934 (1993).

[151] A. J. Molina-Mendoza, J. G. Rodrigo, J. Island, E. Burzuri, G. Rubio-Bollinger, H. S. J. van der Zant, and N. Agraït, "Note: Long-range scanning tunneling microscope for the study of nanostructures on insulating substrates," Rev. Sci. Instrum. **85**, 2014–2017 (2014).

[152] S. Crampin, H. Jensen, J. Kröger, L. Limot, and R. Berndt, "Resonator design for use in scanning tunneling spectroscopy studies of surface electron lifetimes," Phys. Rev. B **72**, 35443 (2005).

[153] J. Tauc, “Optical properties and electronic structure of amorphous Ge and Si,” Mater. Res. Bull **3**, 37 (1968).

[154] I. J. Ferrer, M. D. Maciá, V. Carcelén, J. R. Ares, and C. Sánchez, “On the Photoelectrochemical Properties of TiS_3 Films,” Energy Procedia **22**, 48–52 (2012).

[155] M. Rohlfing and S. Louie, “Electron-hole excitations and optical spectra from first principles,” Phys. Rev. B **62**, 4927–4944 (2000).

[156] G. Strinati, “Effects of dynamical screening on resonances at inner-shell thresholds in semiconductors,” Phys. Rev. B **29**, 5718–5726 (1984).

[157] R. Haydock, “The recursive solution of the Schrödinger equation,” Comput. Phys. Commun. **20**, 11–16 (1980).

[158] A. Marini and R. Del Sole, “Dynamical excitonic effects in metals and semiconductors.” Phys. Rev. Lett. **91**, 176402 (2003).

[159] A. Splendiani, L. Sun, Y. Zhang, T. Li, J. Kim, C.-Y. Chim, G. Galli, and F. Wang, “Emerging Photoluminescence in Monolayer,” Nano Lett. **10**, 1271–1275 (2010).

[160] K. Yang, A. Cantarero, A. Rubio, and R. D’Agosta, “Optimal thermoelectric figure of merit of Si/Ge core-shell nanowires,” Nano Res. **8**, 2611–2619 (2015).

[161] M. Buscema, G. A. Steele, H. S. J. van der Zant, and A. Castellanos-Gomez, “The effect of the substrate on the Raman and photoluminescence emission of single-layer MoS_2,” Nano Res. **7**, 561–571 (2014).

[162] J. Quereda, R. Biele, G. Rubio-Bollinger, N. Agraït, R. D’Agosta, and A. Castellanos-Gomez, “Strong quantum confinement effect in the optical properties of ultrathin α-In_2Se_3,” submitted (2016).

[163] J. Tauc, R. Grigorovici, and A. Vancu, “Optical Properties and Electronic Structure of Amorphous Germanium,” Phys. Status Solidi **15**, 627–637 (1966).

[164] G. W. Mudd, S. A. Svatek, T. Ren, A. Patanè, O. Makarovsky, L. Eaves, P. H. Beton, Z. D. Kovalyuk, G. V. Lashkarev, Z. R. Kudrynskyi, and A. I. Dmitriev, “Tuning the bandgap of exfoliated InSe nanosheets by quantum confinement,” Adv. Mater. **25**, 5714–5718 (2013).

[165] G. Bastard, E. E. Mendez, L. L. Chang, and L. Esaki, “Exciton binding energy in quantum wells,” Phys. Rev. B **26**, 1974–1979 (1982).

[166] C.-H. Ho and Y.-C. Chen, “Thickness-tunable band gap modulation in γ-In_2Se_3,” RSC Adv. **3**, 24896 (2013).

[167] W. S. Yun, S. W. Han, S. C. Hong, I. G. Kim, and J. D. Lee, “Thickness and strain effects on electronic structures of transition metal dichalcogenides : 2H-MX_2 semiconductors (M = Mo , W ; X = S , Se , Te),” Phys. Rev. B **85**, 1–5 (2012).

[168] A. Castellanos-Gomez, “Black Phosphorus: Narrow Gap, Wide Applications,” J. Phys. Chem. Lett. **6**, 4280–4291 (2015).

[169] R. Biele, C. Timm, and R. D’Agosta, “Application of a time-convolutionless stochastic Schrödinger equation to energy transport and thermal relaxation,” J. Phys. Condens. Matter **26**, 395303 (2014).

[170] R. D’Agosta, “Towards a dynamical approach to the calculation of the figure of merit of thermoelectric nanoscale devices.” Phys. Chem. Chem. Phys. **15**, 1758 (2013).

[171] G. Stefanucci, “Bound states in ab initio approaches to quantum transport: A time-dependent formulation,” Phys. Rev. B **75**, 195115 (2007).

[172] R. Biele, E. Flores, J. R. Ares, C. Sanchez, I. J. Ferrer, G. Rubio-Bollinger, A. Castellanos-Gomez, and R. D’Agosta, “Strain induced bang-gap engineering in layered TiS_3,” submitted (2016), arXiv:1509.00532 .

[173] J. O. Island, A. J. Molina-Mendoza, M. Barawi, R. Biele, J. M. Clamagirand, J. R. Ares, C. Sanchez, H. S. J. van der Zant, R. D’Agosta, I. J. Ferrer, and A. Castellanos-Gomez, “Layered TiS_3 for fast and broadband photodetectors,” (Springer, 2016) p. submitted chapter.

[174] K. Burke, R. Car, and R. Gebauer, “Density Functional Theory of the Electrical Conductivity of Molecular Devices,” Phys. Rev. Lett. **94**, 146803 (2005).

[175] M. Di Ventra and R. D’Agosta, “Stochastic Time-Dependent Current-Density-Functional Theory,” Phys. Rev. Lett. **98**, 226403 (2007).

[176] J. Yuen-Zhou, C. Rodríguez-Rosario, and A. Aspuru-Guzik, “Time-dependent current-density functional theory for generalized open quantum systems.” Phys. Chem. Chem. Phys. **11**, 4509–4522 (2009).

[177] R. D’Agosta and M. Di Ventra, “Stochastic time-dependent current-density-functional theory: A functional theory of open quantum systems,” Phys. Rev. B **78**, 165105 (2008).

[178] G. S. Engel, T. R. Calhoun, E. L. Read, T.-K. Ahn, T. Mancal, Y.-C. Cheng, R. E. Blankenship, and G. R. Fleming, “Evidence for wavelike energy transfer through quantum coherence in photosynthetic systems.” Nature **446**, 782–786 (2007).

[179] G. D. Scholes, “Quantum-coherent electronic energy transfer: Did nature think of it first?” J. Phys. Chem. Lett. **1**, 2–8 (2010).

[180] Y.-C. Cheng and G. R. Fleming, “Dynamics of light harvesting in photosynthesis,” Annu. Rev. Phys. Chem. **60**, 241–62 (2009).

[181] F. Fassioli, R. Dinshaw, P. C. Arpin, and G. D. Scholes, “Photosynthetic light harvesting: excitons and coherence,” J. R. Soc. Interface **11**, 20130901 (2014).

[182] R. Zwanzig, “Ensemble Method in the Theory of Irreversibility,” J. Chem. Phys. **33**, 1338 – 1342 (1960).

[183] S. Nakajima, “On Quantum Theory of Transport Phenomena,” Prog. Theor. Phys. **20**, 948 – 959 (1958).

[184] M. V. Berry, “Regular and irregular semiclassical wavefunctions,” J. Phys. A **10**, 2083 (1977).

[185] A. Voros, “Semi-classical approximations,” Annu. Inst. Henri Poincare **1**, 31–90 (1976).

[186] A. Voros, “Asymptotic $\hbar$-expansions of stationary quantum states,” Annu. Inst. Henri Poincare **4**, 343–403 (1977).

[187] S. Zelditch, “Uniform distribution of eigenfunctions on compact hyperbolic surfaces,” Duke Math. J. **55**, 919–941 (1987).

[188] S. Hortikar and M. Srednicki, “Correlations in Chaotic Eigenfunctions at Large Separation,” Phys. Rev. Lett. **80**, 1646–1649 (1998).